HYDROGEN STORAGE MATERIALS: A FIRST-PRINCIPLES STUDY

SÜLEYMAN ER

HYDROGEN STORAGE MATERIALS

A FIRST-PRINCIPLES STUDY

SÜLEYMAN ER

HYDROGEN STORAGE MATERIALS:
A FIRST-PRINCIPLES STUDY

Süleyman Er

Composition of the Graduation Committee

Prof. Dr. V. Subramaniam	University of Twente, Chairman
Prof. Dr. P. J. Kelly	University of Twente, Promoter
Dr. G. H. L. A. Brocks	University of Twente, Assistant Promoter
Prof. Dr. R. Griessen	VU Amsterdam
Prof. Dr. Ir. J. W. M. Hilgenkamp	University of Twente
Prof. Dr. H. Jónsson	University of Iceland
	Brown University
Prof. Dr. Ir. L. Lefferts	University of Twente
Dr. Ir. G. A. de Wijs	Radboud University Nijmegen

HYDROGEN STORAGE MATERIALS:
A FIRST-PRINCIPLES STUDY

DISSERTATION

to obtain
the degree of doctor at the University of Twente,
on the authority of the rector magnificus,
Prof. Dr. H. Brinksma,
on account of the decision of the graduation committee,
to be publicly defended
on Thursday 29$^{\text{th}}$ of October 2009 at 15:00

by

Süleyman Er

born on May 31$^{\text{st}}$, 1980
in Civril, Turkey

This doctoral dissertation is approved by:

Prof. Dr. P. J. Kelly   Promoter

Dr. G. H. L. A. Brocks   Assistant Promoter

VERITAS

Contents

Part − B   Molecular Hydrogen Storage   93

Chapter 1

Introduction

"I will get right to the point. Energy is the single most important problem facing humanity today. We must find an alternative to oil. We need to somehow provide clean, abundant, low-cost energy throughout the world to the 6 billion people that live on the planet today, and the 10+ billion that are expected by the middle of this century. The cheaper, cleaner, and more universally available this new energy technology is, the better we will be able to avoid human suffering, and the major upheavals of war and terrorism."

– Richard E. Smalley

As quoted above, the world needs a new source of energy that is cheap, clean and renewable. Hydrogen can be the next generation of fuels since it has a heating value (39.3 kWh/kg), which is already much higher than the most of the common fuels that are already in use today, such as gasoline (13.3 kWh/kg), propane (14.0 kWh/kg) or methane (15.3 kWh/kg). Hydrogen is abundant in the universe and on our mother earth, but, more importantly, it is regenerative and thus sustainable. If hydrogen is burned (with oxygen) to produce energy in a fuel cell or a combustion engine the only product is pure water vapor, $H_2O_{(gas)}$. A hydrogen cycle based on renewable sources is entirely pollution free, i.e., it has zero CO_2 emissions to the atmosphere. If produced from fossil fuels, on site CO_2 capture is also feasible. Combination of all these properties opens a way of supplying more energy to the whole world and reduce the impact on the environment.

Today, more than 85 % of the world energy demand is covered by fossil based fuels. These include coal, natural gas, and petroleum and its derivatives. Fig. 1.1 shows the decomposition of world energy consumption by fuel type. The world's energy demand is predicted to increase by 70 % from the year 2000 to 2030. Fossil based fuels are expected to supply a significant portion of the demand also in the coming years. However, the amount fossil fuels is limited, and cannot be the ultimate solution to the
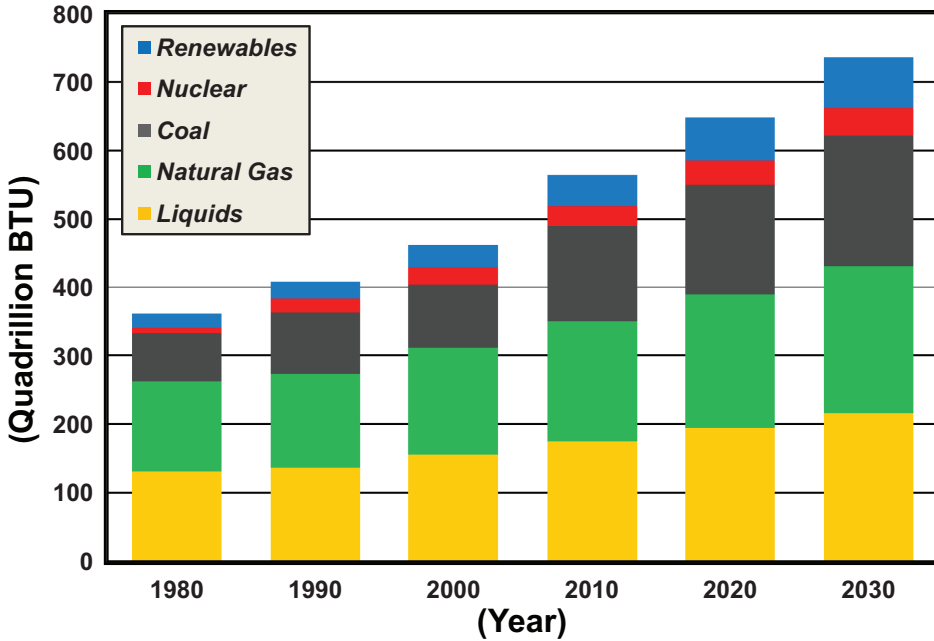
Figure 1.1: World energy consumption by fuel type. Renewables are the fastest growing source of world energy with a projected annual rate of 3.0 %, whereas the liquids are the worlds slowest growing source of energy with an annual rate of 0.9 %. [*Source: US Energy Information Administration, Report No.:DOE/EIA-0484 (May 27th, 2009)*]

energy problem in the long-term. Additionally, the liquid fuel market is vulnerable to fluctuations in prices and is therefore too risky to rely on. The environmental consequences of burning fossil fuels at a larger scale are also not hard to imagine. It is predicted that when all the fossil fuel reserves are consumed, the CO_2 released will raise the atmospheric temperature by 6° C [1]. Such a rise in temperature can harmfully affect the natural life on mother earth. According to Fig. 1.1 the fastest growing source of world energy are the renewables. It is expected to stay like this for the coming years as well. Unfortunately, the share of the renewable energy sources is still small, and definitely not enough to satisfy the world's energy demand entirely. The problems associated with renewable energy systems can be classified into three main categories: (*i*) the efficient conversion of energy into electricity, (*ii*) the storage of energy in the form of hydrogen, and (*iii*) the conversion of hydrogen into work.

In this study we focus on the storage aspects of hydrogen. Under normal conditions hydrogen is a nontoxic, low density gas and composed of diatomic molecules (H_2). The atomic form of hydrogen is very reactive and forms numerous compounds with many other elements, such as oxygen (water). Since a hydrogen atom consists of

a single proton and a single electron, hydrogen is the lightest of all the elements. It can diffuse easily in air or through other substances. Efficient hydrogen storage requires innovative methods, and the development of these methods requires research at a fundamental level. The following sections introduce the most common hydrogen storage materials that are at the focus of present scientific interests.

1.1 Pressurized gas

High pressure gas tanks are the most common storage systems used in today's world. The commercial tanks made from steel are operable up to 200 bars [2], whereas, composite cylinders developed so far can stand pressures up to 800 bars and contain 36 kg hydrogen per m^3 volume. The gravimetric hydrogen densities are, however, markedly reduced due to the necessity of using thick walled cylinders that can withstand such high pressures. Moreover, the energetic cost of pressurizing hydrogen is substantial. At room temperature it requires about 2.21 kWh/kg to reach 800 bars. Furthermore, the safety of high pressure gas tanks is an issue of concern especially if they are used on vehicles or at stations located nearby a densely populated area.

1.2 Cryogenic liquid

Space technology has made use of hydrogen as a fuel in liquid form for several years [3]. Similar to any other gas, storing hydrogen as liquid takes less space than storage as pressurized gas. The volumetric density of liquid hydrogen is 70 kg per m^3, which is almost twice of that of the pressurized gas at 800 bars. Once liquefied it can be maintained as a liquid in thermally insulated containers. However, liquid hydrogen has an extremely low boiling temperature of 20 K, which is actually the second lowest boiling temperature in nature after Helium [4]. Consequently, it requires very sophisticated insulation techniques to keep hydrogen in liquid form. Taking into account of the high energetic cost of hydrogen liquefaction, about 15.2 kWh/kg, together with the difficulties in maintenance, one can conclude that the liquid hydrogen option has no real practical use.

1.3 Metal hydrides

Most of the metals in the periodic table, their alloys or intermetallic compounds react with hydrogen to form metal hydrides. In this sense, the host metallic systems act like hydrogen sponges. The bonding between hydrogens and the metals can range from very covalent to very ionic as well as multi-centered bonds and metallic bonding. The classification of metal hydrides in terms of bonding, however, is not usually sharp, since in some cases several kinds of bonding can be observed in a single metal hydride system.

At certain temperature and pressure conditions large quantities of hydrogen can be absorbed by such metallic systems. When needed as fuel in a fuel cell or combustion engine to generate energy, hydrogen can be released from metal hydrides simply by increasing the temperature. Some metal hydrides can store hydrogen in a density higher than that of liquid hydrogen. The possibility of storing hydrogen in a more compact and safer way compared to pressurized gas and cryogenic liquid is exciting. The (de)hydrogenation reaction can be represented in a simple way:

$$M + \frac{y}{2}\mathrm{H}_2 \rightleftharpoons M\mathrm{H_y},\qquad(1.1)$$

where M is the host storage metal or metal mixture. Here, the thermodynamics play a crucial role in determining whether the material is suitable for storing hydrogen or not. At equilibrium, the change in Gibbs Free Energy ($\Delta G = \Delta H - T\Delta S$) between the metal hydride and the hydrogen gas is zero. The entropy of the metal hydride can be neglected compared to that of the hydrogen gas. The entropy of hydrogen gas at standard conditions (25°C and 1 bar pressure) is 130.7 J/mol·K [5]. For equilibrium under standard conditions, this leads to a formation enthalpy, ΔH, of the hydride of -39 kJ/mol (or -0.40 eV).

Besides suitable thermodynamic properties and volumetric densities, another important issue regarding metal systems is the total weight. In fact, only lightweight metals or their compounds are promising for onboard hydrogen storage. Using a a significant amount of heavy metal in intermetallic compounds has no use since it will result a reduction in hydrogen gravimetric density. The time to load the storage material with hydrogen at a fueling station and unload it onboard is also a concern. Since the formation of metal hydrides and their decomposition back into molecular hydrogen is a chemical process involving lots of bond breaking and formation, storage materials that can demonstrate fast hydrogen kinetics are needed. Recent research on metal hydrides focus on modifying the metal hydride compositions in such a way that the thermodynamics is favorable, hydrogen kinetics is fast, while a meaningful hydrogen gravimetric density is preserved.

1.4   Complex metal hydrides

Hydrides formed by a combination of metals or metalloids are called complex metal hydrides. In such materials hydrogen atoms are bonded covalently to a metal or metalloid atom to form an anion. This anion is then bonded ionically to a metal cation present, to form a complex metal hydride [6].

In general, complex metal hydrides have the formula $\mathrm{A_xM_yH_z}$, where "A" is an alkali metal or alkaline earth metal cation or cation complex, and "M" is a metal or metalloid. Well known examples feature anions of hydrogenated group 3 elements, in particular boron and aluminium. Compounds such as $\mathrm{LiBH_4}$ (lithium borohydride), and $\mathrm{NaAlH_4}$ (sodium alanate) are among the most widely studied. The variety in complex metal hydrides is very large. The possibility of forming complex metal hydrides using lightweight elements opens a promising route to achieve a very high

hydrogen content by weight, e.g., $LiBH_4$ contains 18 wt % hydrogen. Accordingly, there is an increasing interest to explore complex metal hydride systems and their subsequent optimization for practical use. Combining several complex hydrides into one storage system might improve the storage characteristics, but the complexity of reaction mechanisms requires further fundamental research on such materials.

1.5 Other hydrogen storage materials

There are several other materials that are potentially interesting for hydrogen storage. In this section a simple description is given of such materials.

1.5.1 Clathrates

A clathrate is a molecule that traps a second kind of molecule inside. In this case, hydrogen is the guest molecule stored inside clathrates. Large clathrate cages can accommodate multiple hydrogen molecules. Specific examples of the hydrogen storage clathrate family are the clathrate hydrates. They are formed by exerting huge pressures, approximately 2000 bars, to water. The water molecules then form a crystal with cages that can be filled with hydrogen molecules. The desorption mechanism of hydrogen from clathrates involves a structural break down of the clathrate crystal. Recent research focuses on clathrates that can be operated at lower pressures.

1.5.2 Zeolites

Zeolites are microporous inorganic compounds. Some zeolites occur naturally, but most of them are synthesized on an industrial scale. The application areas of zeolites are very diverge, including medical, agricultural, nuclear and petrochemical industries. The beauty of zeolites comes from their ability to selectively sort molecules based primarily on a size exclusion process. The pore structure of zeolites is regular with effective pore sizes between 3 and 10 Å [7]. Hydrogen storage inside zeolite pores faces technical difficulties arising from thermodynamics and kinetics. Moreover, zeolites are usually formed with heavy elements, and therefore hydrogen gravimetric densities are limited.

1.5.3 Nanoporous materials

Recent advances in nanotechnology inspire researchers in developing new hydrogen storage systems. Reasonably inexpensive nano-materials with large internal surfaces can be built from lightweight elements, such as boron, carbon and nitrogen. The storage takes place as hydrogen molecules are adsorbed on the surface of the solids [8]. The possibility of storing hydrogen in molecular form is advantageous over chemical storage in atomic form, which requires dissociation of the hydrogen bond and the formation of a hydride. In this section a brief introduction is given on nanomaterials that are promising for molecular hydrogen storage.

1.5.3.a   Planar systems

Some materials have a layered structure, which is the main driving force for studies on single layers for hydrogen storage. As an example of a planar system one can consider a single sheet of graphite, namely graphene [9, 10]. Theoretical calculations show that graphene layers spaced between 6 and 7 Angstroms apart store hydrogen at room temperature and 100 bars [11]. However, this is only possible if the interplanar distances can be fixed at an appropriate value that maximizes the stored hydrogen content. Spacer molecules can be used for this purpose, although an ideal one has not been reported yet. In order for graphene to become a strong contender for practical hydrogen storage, thermodynamical issues need to be resolved as well. The interaction of hydrogen molecules with the layers needs to be increased in order to enable operating under moderate temperature and pressure conditions. In addition, extending the storage densities to well over a monolayer hydrogen coverage would be interesting. Recently, there are numerous studies in this field [12–18].

1.5.3.b   Curved systems

Carbon structures with curvature, such as single-walled carbon nanotubes (SWNT) [19–22] and buckyballs [23–26] are among the most widely investigated nano-materials for hydrogen storage. The presence of a high specific surface area is promising for physical and chemical optimization of such materials. Carbon-only structures, and their derivatives obtained through doping, are the main stream materials considered so far. Compared to the planar systems discussed in section 1.5.3.a, structures with curvatures faces the same challenges in the optimization process to store hydrogen. These can be categorized into two main categories. Firstly, the binding energies of hydrogen molecules to naked curved systems (carbon only, or doped systems with similar curvatures, such as boron or nitrogen doped SWNTs or buckballs) is in the physisorption range. Therefore these unpractically low binding energies have to be increased. Secondly, similar to the planar systems the hydrogen coverage densities need to be enhanced to well over monolayer values.

The usual approach to the above mentioned problems is doping nano-materials with metals. Considering the gravimetric hydrogen density issue, it is only the lightweight metals that are potentially interesting for doping. The challenge is to find metals that can bind to SWNTs or buckyballs strong enough so that they are immobilized on the surface, and resist to metal clustering. The density of the metals covering the surface is also important and needs to be adjusted to an optimum value. That is, it should be high enough to capture as much hydrogen as possible, but low enough to preserve the hydrogen gravimetric density by not influencing the total system weight to a great extend. The interaction between the hydrogen molecules and metal atoms deposited on a surface can be electrostatic, chemisorption or of Kubas type [27–30].

1.5.3.c   Metal-Organic Frameworks: MOFs

Metal-Organic Frameworks (MOFs) are crystalline compounds consisting of metal ions or metal oxide clusters, coordinated with rigid organic molecules, forming regular three dimensional (3-D) structures [31]. MOFs are stable and highly porous systems. Additionally, they are among the lowest density crystalline materials, thanks to the presence of pores inside the lattice and the usage of mainly lightweight elements as building blocks. All these properties together make MOFs ideal candidates to store gases, like as hydrogen, methane or carbon dioxide [32–45]. Although the properties of gas kinetics depends on the size of the pores, in general MOFs are considered as systems allowing fast diffusion. This is due to the fact that the pores in 3-D form a continuous network.

The interaction of hydrogen molecules with the material shows different properties depending on the metal and organic components used in the construction of network. MOFs without defects in their crystal structures can bind several hydrogen molecules, but the binding interactions are usually weak, similar to other physisorption nano-materials. Increasing the H_2 binding energies is a current focus of research on MOF systems. Some of these methods can briefly explained as follows:

- (*i*) It is believed that MOFs with very large pores are not practical for massive hydrogen store. The reasoning is that the H_2 molecules close to the center of the pores are weakly interacting with the framework, consequently the binding energies are very low. The reduction of the pore size can be accomplished by penetrating MOFs. It is, however, is not so clear yet whether an increase in hydrogen binding energies as a consequence of penetration will offset the loss of free volume and its effects on the total hydrogen uptake.

- (*ii*) The second method involves catalyst initiated dissociation of H_2 and subsequent migration of atomic hydrogen onto the material surface. This process is called hydrogen spillover. However, the process of spillover in MOFs is largely unknown, and remains to be explored at a fundamental level. The recyclability and kinetics remain the main concerns for hydrogen stored via spillover in MOFs.

- (*iii*) Exposing metal atoms is another approach to improve interactions between hydrogen molecules and the MOFs. This is accomplished either by creating vacancies within the framework itself, or pumping extra metal atoms into the MOF lattice. Accordingly, hydrogen molecules are expected to be captured via non-van der Waals binding, such as Kubas type or electrostatic interactions. In principle, the strength of interactions are expected to increase to a range between physisorption and chemisorption. Unfortunately, the number of hydrogen molecules that can bind to a defect site is limited, and the only way to increase hydrogen densities is to create as many defect sites as possible. Defects, however, may lead to deformations in the framework structure and can harmfully affect the gas diffusion. Recent theoretical studies claim that MOFs with penetrated lightweight metal ions, such as Li, show improved hydrogen binding energies [46, 47].

To sum up, the ability to modify the metallic and organic components of metal-organic frameworks in a way to optimize the hydrogen storage properties is promising. Lately, numerous experimental and theoretical studies focus on gas storage in MOFs.

Bibliography

[1] S. Arrhenius, Philos. Mag. **41**, 237 (1896).

[2] L. Schlapbach and A. Züttel, Nature **414**, 353 (2001).

[3] S. Sherif, N. Zeytinoglu, and T. Veziroglu, Int. J. Hydrogen Energy **22**, 683 (1997).

[4] A. M. James and M. P. Lord, *Macmillan's chemical and physical data* (London: Macmillan, 1992).

[5] M. W. Chase, J. Phys. Chem. Ref. Data **9**, 1.

[6] A. F. Holleman and E. Wiberg, *Holleman-Wiberg Inorganic Chemistry* (San Diego: Academic Press, 2001).

[7] C. R. A. Catlow, *Modelling of structure and reactivity in zeolites* (London: Academic Press, 1992).

[8] A. Züttel, Mater. Today **6**, 24 (2003).

[9] A. Geim and K. Novoselov, Nat. Mater. **6**, 183 (2007).

[10] A. Geim and A. MacDonald, Phys. Today **60**, 35 (2007).

[11] S. Patchkovskii *et al.*, Proc. Natl. Acad. Sci. U.S.A. **102**, 10439 (2005).

[12] J. S. Arellano, L. M. Molina, A. Rubio, and J. A. Alonso, J. Chem. Phys. **112**, 8114 (2000).

[13] T. Heine, L. Zhechkov, and G. Seifert, Phys. Chem. Chem. Phys. **6**, 980 (2004).

[14] W. Q. Deng, X. Xu, and W. A. Goddard, Phys. Rev. Lett. **92**, 166103 (2004).

[15] D. Henwood and J. D. Carey, Phys. Rev. B **75**, 245413 (2007).

[16] N. Park, S. Hong, G. Kim, and S. H. Jhi, J. Am. Chem. Soc. **129**, 8999 (2007).

[17] G. Kim, S. H. Jhi, and N. Park, Appl. Phys. Lett. **92**, 013106 (2008).

[18] C. Ataca, E. Aktürk, S. Ciraci, and H. Ustunel, Appl. Phys. Lett. **93**, 043123 (2008).

[19] P. Chen, X. Wu, J. Lin, and K. L. Tan, Science **285**, 91 (1999).

[20] C. Liu *et al.*, Science **286**, 1127 (1999).

[21] R. Yang, Carbon **38**, 623 (2000).

[22] E. Lee, Y. Kim, Y. Jin, and K. Chang, Phys. Rev. B **66**, 73415 (2002).

[23] Y. H. Kim, Y. Zhao, A. Williamson, M. J. Heben, and S. B. Zhang, Phys. Rev. Lett. **96**, 16102 (2006).

[24] Q. Sun, P. Jena, Q. Wang, and M. Marquez, J. Am. Chem. Soc. **128**, 9741 (2006).

[25] K. R. S. Chandrakumar and S. K. Ghosh, Nano Lett. **8**, 13 (2008).

[26] Q. Sun, Q. Wang, and P. Jena, Appl. Phys. Lett. **94**, 013111 (2009).

[27] J. Niu, B. K. Rao, and P. Jena, Phys. Rev. Lett. **68**, 2277 (1992).

[28] L. Gagliardi and P. Pyykkö, J. Am. Chem. Soc. **126**, 15014 (2004).

[29] E. Durgun, S. Ciraci, W. Zhou, and T. Yildirim, Phys. Rev. Lett. **97**, 226102 (2006).

[30] R. C. Lochan and M. Head-Gordon, Phys. Chem. Chem. Phys. **8**, 1357 (2006).

[31] O. Yaghi *et al.*, Nature **423**, 705 (2003).

[32] N. L. Rosi *et al.*, Science **300**, 1127 (2003).

[33] X. Zhao *et al.*, Science **306**, 1012 (2004).

[34] J. Rowsell, J. Eckert, and O. Yaghi, J. Am. Chem. Soc. **127**, 14904 (2005).

[35] J. Rowsell, A. Millward, K. Park, and O. Yaghi, J. Am. Chem. Soc. **126**, 5666 (2004).

[36] J. Rowsell, E. Spencer, J. Eckert, J. Howard, and O. Yaghi, Science **309**, 1350 (2005).

[37] J. Rowsell and O. Yaghi, J. Am. Chem. Soc. **128**, 1304 (2006).

[38] J. Rowsell and O. Yaghi, Angew. Chem., Int. Ed. **44**, 4670 (2005).

[39] A. Wong-Foy, A. Matzger, and O. Yaghi, J. Am. Chem. Soc **128**, 3494 (2006).

[40] S. S. Kaye, A. Dailly, O. M. Yaghi, and J. R. Long, J. Am. Chem. Soc **129**, 14176 (2007).

[41] J. G. Vitillo *et al.*, J. Am. Chem. Soc. **130**, 8386 (2008).

[42] W. Zhou, H. Wu, and T. Yildirim, J. Am. Chem. Soc. **130**, 15268 (2008).

[43] M. Dinca and J. R. Long, Angew. Chem., Int. Ed. **47**, 6766 (2008).

[44] A. Dailly, J. Vajo, and C. Ahn, J. Phys. Chem. B **110**, 1099 (2006).

[45] J. Liu *et al.*, J. Phys. Chem. C **100**, 2911 (2008).

[46] S. Han and W. Goddard III, J. Am. Chem. Soc. **129**, 8422 (2007).

[47] A. Blomqvist, C. M. Araujo, P. Srepusharawoot, and R. Ahuja, Proc. Natl. Acad. Sci. U.S.A. **104**, 20173 (2007).

Chapter 2

Methodology

An appropriate description of the physical and chemical properties of matter is a complicated task. The problem involves interacting nuclei and electrons, and in some cases an external field. Quantum mechanics is a set of principles that predicts how the particles behave, given the elementary properties such as the rest masses and charges. It is the most successful and powerful theory ever created. In the heart of this monumental scientific achievement lies the Schrödinger Equation. In principle, by solving the Schrödinger equation one can access all the properties of a material of any size. However, the problem becomes practically unsolvable as the number of interacting particles increases, which is the case for most real-life situations.

The methodology chapter starts with a short introduction of the Schrödinger Equation, which is followed by the Born-Oppenheimer Approximation. Density Functional Theory, which is one of the leading electronic structure methods developed so far to investigate many-body systems (i.e., atoms, molecules, clusters or condensed phases), is discussed next. Exchange and correlation functionals are discussed in Section 2.4. Section 2.5 summarizes the usefulness of pseudopotential approach. Technical details on modeling infinite periodic systems, as well as the basis set used in the present calculations, are mentioned in Section 2.6. The last section of the chapter (Section 2.7) includes the details of calculations of some physical properties.

2.1   The Schrödinger Equation

At the beginning of the twentieth century, wave-like behavior of atomic particles observed in experiments inspired theoreticians in using wave equations to describe the behavior of physical systems. In the year 1926 Erwin Schrödinger formulated a fundamental equation to describe the quantum aspects of matter. The many body form of the time independent Schrödinger equation consisting of M nuclei and N electrons is written as:

$$\hat{H}\psi_i(\mathbf{r}_1, \mathbf{r}_2, ..., \mathbf{r}_N, \mathbf{R}_1, \mathbf{R}_2, ..., \mathbf{R}_M) = E_i\psi_i(\mathbf{r}_1, \mathbf{r}_2, ..., \mathbf{r}_N, \mathbf{R}_1, \mathbf{R}_2, ..., \mathbf{R}_M), \quad (2.1)$$

where, $\hat{H}$ denotes the Hamiltonian, and ψ_i the wave function in terms of all the electronic ($\mathbf{r}$) and nuclear coordinates ($\mathbf{R}$).

In principle, the above equation is applicable to any physical system regardless of size (i.e., from atoms to a whole crystal). In practice, however, a complete analytical solution is almost impossible for most real life systems, since the number of variables to deal with is determined by the $3(M + N)$ degrees of freedom. If we consider the methane molecule (chemical formula: CH_4), then there are in total 5 atomic nuclei and 10 electrons. The time independent Schrödinger Equation for a single methane molecule consequently becomes a partial differential eigenvalue problem in 45 variables. Although the exact solution of the Schrödinger Equation is unaffordable for almost every real system, sensible approximations are used to make the most use of it.

2.2 Born-Oppenheimer Approximation

The Born-Oppenheimer Approximation [1] lightens the calculation of the energy and the wave function of moderate size physical systems by making use of the significant mass differences between the nuclei and the electrons. Considering the same methane molecule example mentioned in the previous section (Section 2.1), we see that mass of the nucleus is 2800 times that of all the electrons surrounding it. It is therefore possible to decouple the motion of relatively slow moving nuclei and that of the fast moving electrons. In other words, the wave function of the system can be divided into electronic and nuclear components:

$$\psi(\mathbf{r}, \mathbf{R}) = \psi_{electronic}(\mathbf{r}, \mathbf{R}) \times \psi_{nuclear}(\mathbf{R}). \quad (2.2)$$

In the first step of the Born-Oppenheimer Approximation the nuclei are assumed to have fixed positions, and the electronic Schrödinger Equation, which depends only on the electronic coordinates, is solved. For instance, the electronic wave function of the methane molecule depends on 30 electronic coordinates. It is assumed that for fixed nuclear positions the electrons are in their ground state. Consequently, the calculated electronic energies are functions of nuclear positions. In the second step of the Born-Oppenheimer Approximation, these electronic functions serve to calculate a potential for the nuclear component of the Schrödinger Equation. In the case of the methane example it needs to deal with only 15 variables. To sum up, the nuclei move on the potential energy surface of the electronic ground state, and the electrons follow the nuclear motion adiabatically.

2.3   Density Functional Theory: DFT

Decoupling the Schrödinger Equation into electronic and nuclear components by the Born-Oppenheimer Approximation simplifies the problem. However, the electronic problem is still too complicated to be solved exactly due to the interactions between the electrons. Instead of using the 3N-dimensional Schrödinger Equation for the many electron wave function,$\psi_i(\mathbf{r}_1, \mathbf{r}_2, ..., \mathbf{r}_N)$, Density Functional Theory (DFT) reduces the problem into a series of coupled one-body problems. This is accomplished by using the electronic density distribution, $n(r)$, and a universal functional of the density $E_{\mathrm{xc}}[n(r)]$.

2.3.1   Hohenberg-Kohn Theorem

In the year 1964, P. Hohenberg and W. Kohn [2] proved that the construction of the total energy of a physical system can be expressed in terms of the electronic density. The ideas are related to earlier propositions of Thomas and Fermi in 1927, where atoms were modeled as systems with a positive potential (the nucleus) located in a uniform electron gas [3, 4]. The Hohenberg-Kohn theorem consist of two main parts:

- **Theorem I**: In a system of N interacting particles under the influence of an external potential $V_{ext}(r)$, the ground state electron density, $n(r)$, uniquely determines the potential, $V_{ext}(r)$.

Since $n(r)$ determines $V_{ext}(r)$, then the full ground state Hamiltonian is known. Consequently, $n(r)$ completely determines all the properties of a physical system, such as the eigenfunctions, $\psi_i(\mathbf{r}_1, \mathbf{r}_2, ..., \mathbf{r}_N)$ and the eigenvalues, E_i. In other words, the first theorem states that the energy is a unique functional of the electron density:

$$E[n(\mathbf{r})] = F[n(\mathbf{r})] + \int V_{\mathrm{ext}}(\mathbf{r})n(\mathbf{r})d^3\mathbf{r}. \qquad (2.3)$$

- **Theorem II**: There exists a functional $F[n(r)]$ for the ground state energy, for any given $V_{ext}(r)$. The global minimum of this functional defines the exact ground state energy of the physical system, and the density that minimizes the total energy is the exact ground state density, $n_0(r)$.

The second theorem states that the ground state electron density, $n_0(r)$, minimizes the universal functional, F, such that the electronic energy reaches its minimum value of $E[n_0(\mathbf{r})]$:

$$E[n_0(\mathbf{r})] = F[n_0(\mathbf{r})] + \int V_{\mathrm{ext}}(\mathbf{r})n_0(\mathbf{r})d^3\mathbf{r}. \qquad (2.4)$$

It should be noted that $F[n(\mathbf{r})]$ depends purely on the electron density. It does not depend on the external potential, $V_{ext}(r)$. The above two theorems together form the basis of DFT.

2.3.2 Kohn-Sham Equations

In order to find the ground state density, $n_0(\mathbf{r})$ W. Kohn and L. Sham [5] developed a set of differential equations in 1965. They start with the decomposition of the density functional given in (Eq. 2.3) into three parts:

$$E[n(\mathbf{r})] = T_0[n(\mathbf{r})] + E_H[n(\mathbf{r})] + E_{xc}[n(\mathbf{r})] + \int V_{\text{ext}}(\mathbf{r})n(\mathbf{r})d^3\mathbf{r}, \qquad (2.5)$$

where $T_0[n(\mathbf{r})]$, $E_H[n(\mathbf{r})]$ and $E_{xc}[n(\mathbf{r})]$ define the kinetic energy, Hartree energy as a consequence of electron-electron repulsions, and exchange and correlation energies, respectively. The main idea behind the Kohn and Sham equations is to replace the kinetic energy of interacting electrons with that of an equivalent non-interacting system, and define E_{xc} such, that the non-interacting system has the same ground state density as the interacting system. Within this assumption the electron density is given by the single particle wave functions, $\psi_{i,s}$ where s labels the spin state,

$$n(\mathbf{r}) = \sum_{s=1}^{2} \sum_{i=1}^{N} |\psi_{i,s}(\mathbf{r})|^2, \qquad (2.6)$$

and accordingly the kinetic energy is described as,

$$T_0[n(\mathbf{r})] = \sum_{s=1}^{2} \sum_{i=1}^{N} \langle \psi_{i,s}(\mathbf{r})| - \frac{\nabla^2}{2} |\psi_{i,s}(\mathbf{r})\rangle. \qquad (2.7)$$

Minimizing the total energy with respect to the single particle wave functions, under the constraint that these form an orthonormal set, leads to the Kohn-Sham equations:

$$\left[-\frac{\hbar^2}{2m}\nabla^2 + V_{\text{eff}}(\mathbf{r}) \right] \psi_{i,s}(\mathbf{r}) = \epsilon_{i,s}\psi_{i,s}(\mathbf{r}). \qquad (2.8)$$

In this way, the problem of interacting particles is reduced to an equivalent problem of non-interacting particles. The effective potential used in above Eq. (2.8) has the form:

$$V_{\text{eff}}(\mathbf{r}) = e^2 \int \frac{n(\mathbf{r})}{|\mathbf{r} - \mathbf{r'}|}d^3\mathbf{r} + \frac{\delta E_{\text{xc}}[n]}{\delta n(\mathbf{r})} + V_{\text{ext}}(\mathbf{r}). \qquad (2.9)$$

In principle, the above Kohn-Sham equations are just mathematical representations used to reduce the complexity of the problem. They need to be solved using a self consistent procedure. Although the exact E_{xc} functional is not known, approximate functionals have been constructed that are universal in the sense that they do not depend on the materials investigated. Without the use of special basis sets and algorithms, the computational costs of solving the Kohn-Sham equations scale as N^3, where N represents the total number of Kohn-Sham orbitals.

2.4 Exchange and Correlation Functionals

The Kohn-Sham approach allows the calculation of the kinetic energy term in Eq. 2.5. The only undetermined component of the equation is the exchange-correlation energy functional, $E_{xc} = E_x + E_c$. However, the exact form this functional is not known and an approximate description is used instead. Researchers still focus on generating new exchange-correlation functionals to improve the accuracy of DFT. Computational results obtained with different functionals are directly compared to experiments to decide which functionals to be used in a particular study. The details of the functionals used in this study are given below:

2.4.1 Local Density Approximation: LDA

In the local density approximation (LDA) general inhomogeneous electronic system is considered as locally homogeneous. For a spin-unpolarized system, local density approximation for the exchange-correlation energy is written as

$$E_{\text{xc}}^{\text{LDA}} = \int n(\mathbf{r})\varepsilon_{\text{xc}}[n(\mathbf{r})]d^3\mathbf{r}, \qquad (2.10)$$

where n, and $\varepsilon_{\text{xc}}[(n(\mathbf{r})]$ define the electron density and exchange-correlation energy per electron, respectively. Similarly, the exchange-correlation potential is written as

$$V_{\text{xc}}(\mathbf{r}) = \frac{\delta E_{\text{xc}}[n(\mathbf{r})]}{\delta n(\mathbf{r})} = \varepsilon_{\text{xc}}[n(\mathbf{r})] + n(\mathbf{r})\frac{d\varepsilon_{\text{xc}}[n(\mathbf{r})]}{dn(\mathbf{r})}. \qquad (2.11)$$

The most common form of LDA is based on numerical Monte Carlo calculations of the energy of homogeneous electron gases of varying densities, $\varepsilon_{\text{xc}}[(n(\mathbf{r})] = \varepsilon_{\text{xc}}^{hom}[(n(\mathbf{r})]$ by Ceperley and Alder [6]. In this study, we make use of the Perdew and Zunger [7] parameterized form of the Ceperley and Alder exchange-correlation.

LDA calculations usually describe the chemical trends correctly. The geometrical properties such as the cell parameters, bond lengths, and bond angles are also within a few percent for systems involving covalent, ionic or metallic bonds. On the other hand, the binding energies are mostly overestimated. In LDA, the exchange-correlation energy due to inhomogeneities in the electron density is ignored. Consequently, LDA has limitations for very inhomogeneous systems, finite systems being the most obvious ones.

2.4.2 Generalized Gradient Approximation: GGA

The failure of LDA in situations where the charge density undergoes rapid changes has motivated scientists to develop more advanced approximations. Deviations from the non-uniform charge density can be expressed in terms of gradients and higher spatial derivatives of the total charge density. Generalized Gradient Approximation (GGA) uses the gradient of the charge density as a correction for such deviations. The functional can be defined as a generalized form of Eq. (2.10) such that,

$$E_{\mathrm{xc}}^{\mathrm{GGA}} = \int n(\mathbf{r})\varepsilon_{\mathrm{xc}}[n(\mathbf{r})]F_{\mathrm{xc}}[n(\mathbf{r}), \nabla n(\mathbf{r})]d^3\mathbf{r}. \tag{2.12}$$

F_{xc} is dimensionless and numerous forms of it exist in literature. The most widely used forms in solid state physics are proposed by Perdew and Wang(PW91) [8] and Perdew, Burke, and Ernzerhof (PBE) [9, 10]. Unless otherwise stated, GGA calculations in this study make use of the PW91 functional. Some of the calculations are repeated with the PBE functional for comparison.

Compared to LDA, GGA improves the binding energies, especially when there is chemical bonding between the atoms. The description of the geometries, however, is not universally better. Similar to LDA, screening of exchange hole is not fully taken into account in GGA. Consequently, GGA cannot account for noticeable improvements to the band gap problem or to the calculation of the dielectric constants.

2.5 Pseudopotential Approach

The majority of the properties of a physical system are determined by its valence electrons rather than its core electrons. Therefore, in an effort to simplify the computational cost of calculations the ionic cores can be treated as frozen in their atomic configurations. In other words, the core electrons are pre-calculated in an atomic environment and kept frozen in the course of the remaining calculations. The pseudopotential (also called effective potential) approach utilizes this idea by replacing the core electrons and the strong ionic potential with a weaker pseudopotential that acts on a set of pseudo wave functions. Although the general ideas behind the pseudopotential approach are similar, there are several procedures to construct pseudopotentials, such as norm-conserving [11–13] and ultrasoft [14, 15]. In this study we make use of the pseudopotentials constructed using the Projector Augmented Wave (PAW) method [16, 17] as will be discussed in the next section.

2.5.1 Projector Augmented Waves: PAW

In 1994, Peter Blöchl developed the so called Projector Augmented Wave (PAW) method which combines the traditions of augmented wave methods and ultra-soft pseudopotentials into a unified description [16]. The most striking property of the PAW method is that the full all-electron wave function is kept and therefore the wave functions within the core regions are recovered. Additionally, advanced algorithms are used for a more efficient solution of the generalized eigenvalue problem.

In an effort to overcome the computational costs resulting from all-electron calculations, Blöchl pointed out that the true wave function, Ψ, and the pseudo wave function, $\tilde{\Psi}$, can be linked by a linear transformation

$$\Psi = T\tilde{\Psi}, \tag{2.13}$$

$$T = 1 + \sum_j (|\phi_j\rangle - |\tilde{\phi}_j\rangle)\langle\tilde{p}_j|. \tag{2.14}$$

The proposed transformation operator is shown above (Eq. 2.14), where ϕ_j, $\tilde{\phi}_j$, and $\tilde{p}_j$ are the all-electron partial waves, pseudo partial waves and PAW projector functions, respectively. Projector functions probe the character of the wave function, such as s, p and d-type. Applying this into the all-electron wave function equation one obtains the following expression:

$$|\Psi_n\rangle = |\tilde{\Psi}_n\rangle + \sum_j (|\phi_j\rangle - |\tilde{\phi}_j\rangle)\langle\tilde{p}_j|\tilde{\Psi}_n\rangle. \tag{2.15}$$

As the projector functions are effectively operative only in the core regions, the all-electron wave functions are obtained from the pseudo wave functions by projecting out the core regions and replacing the pseudo partial waves by the all electron partial waves. In principle, the functions ϕ_j, $\tilde{\phi}_j$, and $\tilde{p}_j$ can be optimized self-consistently for each system. In practice, these functions are obtained from an atomic calculation and then frozen, such that their effect can be incorporated as a fixed pseudopotential. Consequently, the computational effort is now reduced to a great extend. The PAW technique is surprisingly accurate, i.e., almost comparable to the full all-electron methods.

2.6 Periodicity vs. non-Periodicity

If a system obeys a set of periodic boundary conditions, this enables to model a large system using only a small part of it that is far from its edge. Crystalline bulk materials with no surfaces present are perfect examples of systems with periodicity. Such systems can be studied using unit cells to reduce the computational effort. In mathematical terms, for the potential of a periodic system operating on an electron we have:

$$V(\mathbf{r}+\mathbf{R}) = V(\mathbf{r}), \tag{2.16}$$

for all Bravais lattice vectors $\mathbf{R}$. Since the scale of periodicity of V is $\sim 10^{-9}$ meters, quantum mechanics is an essential tool to study the effect of periodicity on electronic motion.

2.6.1 Bloch's Theorem

In a condensed system the number of electrons can be assumed as infinite, which makes the solution of the Schrödinger equation very complicated. Felix Bloch, in year 1928, developed a theorem that enables the consideration of only the electrons within the unit cell to solve the Schrödinger equation [18, 19]. The theorem states that the wave function of an electron within a perfectly periodic potential can be written as

$$\psi_{n\mathbf{k}}(\mathbf{r}) = u_{n\mathbf{k}}(\mathbf{r})e^{i\mathbf{k}\cdot\mathbf{r}}, \tag{2.17}$$

where $\mathbf{k}$ is the wave vector analogous to that of the wave vector in the theory of free electrons, $\mathbf{r}$ is a position vector, and $u_{n\mathbf{k}}(\mathbf{r})$ is a periodic function that satisfies the boundary condition, $u_{n\mathbf{k}}(\mathbf{r}) = u_{n\mathbf{k}}(\mathbf{r}+\mathbf{R})$. The corresponding energy eigenvalue is

$$\epsilon_n(\mathbf{k}) = \epsilon_n(\mathbf{k}+\mathbf{K}), \tag{2.18}$$

where $\mathbf{K}$ is a reciprocal lattice vector. $\epsilon_n(\mathbf{k})$ is a continuous function, and since the energies associated with the index, n, vary with wave vector, $\mathbf{k}$, we speak of an energy band. All distinct values of $\epsilon_n(\mathbf{k})$ are represented by $\mathbf{k}$ values within the first Brillouin zone of the reciprocal lattice.

2.6.2 Sampling of Brillouin Zone

In principle, an infinite number of $\mathbf{k}$-points are necessary to account for infinite number of electrons in a periodic system. Bloch's theorem (Section 2.6.1) reduces the problem of calculating an infinite number of electronic wave functions to a finite number of wave functions for an infinite number of $\mathbf{k}$-points. In practice, one does not need an infinite number of $\mathbf{k}$-points since the electronic wave functions will be almost identical for $\mathbf{k}$-points that are very close to each other. Therefore, a single $\mathbf{k}$-point will be sufficient to represent the wave functions over a particular segment of $\mathbf{k}$-space. In general, structures with high symmetry can be sampled with a reduced $\mathbf{k}$-point set, since it is sufficient to consider the $\mathbf{k}$-points only within the irreducible part of the Brillouin zone. Metallic systems require dense set of $\mathbf{k}$-points for a more accurate determination of Fermi level. There exist several methods to generate suitable $\mathbf{k}$-point sets and corresponding weights [20]. Using these $\mathbf{k}$-point sets generated by such methods, an accurate approximation of the electronic potential and total energy can be possible at a reduced computational cost. The magnitude of the errors in the calculated results decreases by making use of denser $\mathbf{k}$-point sets.

2.6.3 Plane wave Basis

Using Bloch's theorem explained in Section 2.6.1, one electron wave functions at each $\mathbf{k}$-point can be expanded in terms of discrete plane-waves. In principle, an infinite number of plane-waves are required to perform such an expansion. However, a finite number of plane-waves are sufficient to span the lowest energy electronic states, in which all the electrons of the physical system can be accommodated. Therefore, in practice, the number of plane-waves used in a calculation is determined by $\sqrt{E_{\text{cutoff}}2m_e}/\hbar$, where E_{cutoff} is the kinetic cutoff energy. It is the only parameter that controls the accuracy of the plane wave basis set.

Plane wave basis sets are mathematically simple, cover all the space equally without being biased to any particular region, and span the Hilbert space completely. In this sense, they are superior to local basis sets, especially when the initial form of the
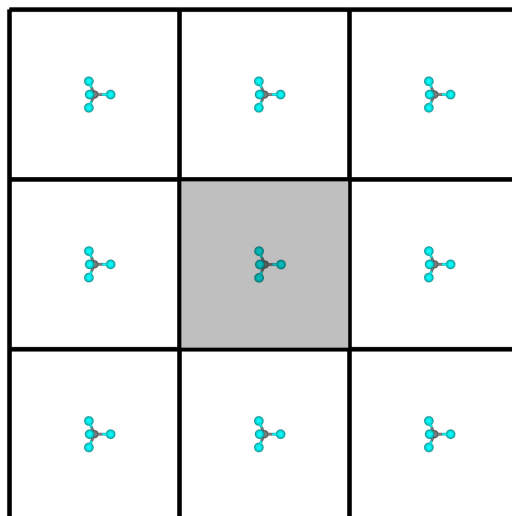
Figure 2.1: Schematic representation of a methane (CH_4) molecule placed in a cubic box of 20 Å that obeys periodic boundary conditions. Calculations are only performed using the shaded supercell, and the rest of the images are due to periodicity.

wave functions is unknown. The main disadvantage of a plane wave basis compared to local basis sets is the computational costs.

2.6.4 Non-periodic Systems

In real life, the periodicity of the systems can be hampered by defects in the crystal structure. Bloch's description of waves, however, is only applicable to periodic systems. In order to be able to write the eigenfunctions in form of Eq. 2.17 the periodicity of the system need to be recovered. A practical approach to the problem is to use supercells in stead of unit cells. The supercells need to be chosen in a way to recover the periodicity of the system so that the Bloch's theorem can be applied. In some cases, it may be necessary to use very large supercells to perform the simulations. In this manner, even molecules can be studied by constructing supercells large enough to prevent the interactions between the molecules in neighboring cells. In Fig. 2.1 a cubic supercell with an edge length of 20 Å is chosen to perform calculations on a single methane molecule (CH_4). Note that the image is repeated infinitely in three dimensions due to periodicity. However, the interaction of neighboring methane molecules is almost negligible at such distances. Naturally, large molecules require large supercells to maintain a sufficiently large separation between neighboring images.

2.7   Numerical Calculations

The results presented in this thesis are obtained via first-principles plane wave calculations within density functional theory (DFT) as implemented in the Vienna *ab initio* simulation package (VASP) [21, 22]. The kinetic cutoff energies for the plane-waves are chosen in a way as to assure a high convergence on the total energy, usually in the order of 10^{-3} eV/atom. The cutoff energies are determined through initial test calculations, and the numerical values range from 400 eV to 650 eV depending on the chemical elements present. The Brillouin zone (BZ) is integrated using regular **k**-point grids [20]. The Projector Augmented Wave (PAW) potentials are used to represent both the core and valence electrons [16, 17]. The reliability of these PAW potentials is checked by verifying well-known experimental results, such as lattice parameters and cohesive energies of simple bulk materials. Exchange-correlation potentials are approximated by the generalized gradient approximation (GGA) method using the Perdew Wang 91 (PW91) functional [8]. Some of the results are checked by using the Perdew Bucke Enzenhof (PBE) functional [9, 10]. Geometries are optimized with or without symmetry constraints, using the conjugate gradient (CG) algorithm. During the geometry relaxations the partial occupancies of the wave functions for metallic systems are represented by smearing methods, such as gaussian or Methfessel-Paxton [23]. The width of the smearing is carefully chosen to obtain a meaningful description of the energy. The numerical values for the smearing width are usually between 0.01 eV and 0.1 eV. During the relaxation processes special care is taken to achieve a high electronic convergence, in the order of 10^{-4} eV difference between two consecutive steps, in order to obtain accurate forces. A break condition of at most 0.02 eV/Å on total remaining force on each atom is set for the relaxation. The final total energies and charge densities of the optimized structures are obtained using the corrected linear tetrahedron method [24]. Further analysis of the densities of states, band structures and charge decompositions are performed on the fully optimized systems. A single H_2 molecule is treated within a cubic box with a cell parameter of 10 Å, using periodic boundary conditions and Γ-point sampling, whereas other molecules are studied in a larger cubic box with a cell parameter of 20 Å. For relaxations in slab calculations a spacing of approximately $\sim$20 Å between the slabs is conserved to prevent interactions of repeated periodic images.

2.7.1   Convergence Tests

The choice of pseudopotential, cutoff energy for the plane wave basis, and **k**-points to span the Brillouin zone (BZ), are the three most important factors that determine the quality of the numerical calculations. As mentioned in Section 2.5.1, the PAW potentials provide accuracy at a reasonable computational effort. However, there is no global value for the plane wave cutoff energy or a set of **k**-points that works fine for every individual system. Reliable results can only be obtained if accurate cutoffs (E_{cutoff}) and dense **k**-points are used. E_{cutoff} purely depends on the chemical
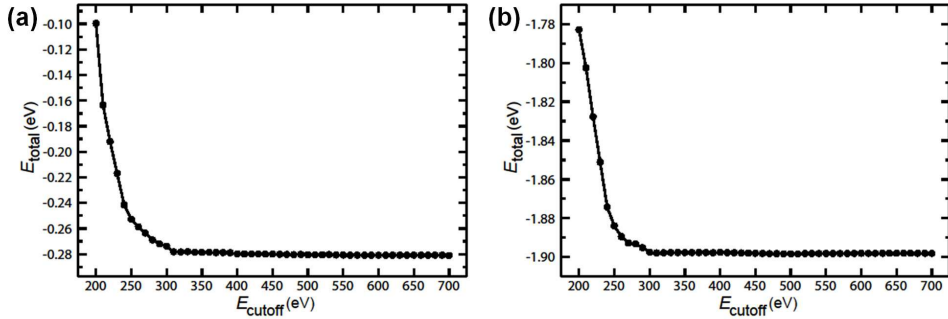
Figure 2.2: The variation of total energies w.r.t. E_{cutoff} used in calculation for Li in atomic form (a), and bulk form (b). The energies are given in units of electron volt and the calculated total energies are per Li.

elements used in the calculations.

If the material of interest is composed of several chemical elements, then it is appropriate to set E_{cutoff} to that of the value of the element with the highest cutoff. As an example, Fig. 2.2 shows the calculated total energy values for Li in atomic form (a), and bulk form (b), as a function of E_{cutoff}. Obviously, the E_{cutoff} need to be chosen from the region where the the variation in total energy is negligible while keeping in mind that higher cutoff values require more computational effort. For Li a value of E_{cutoff}=320 eV will be an adequate choice. A Similar analysis also needs to be performed for **k**-point sampling. A system specific **k**-point mesh should be dense enough the BZ to acquire the convergence in total energy as in the case of E_{cutoff}.

2.7.2 Thermodynamics

Thermodynamics is defined as the branch of science that deals with conversion of energy into work and heat and its relation to macroscopic variables such as temperature, volume and pressure. To address the thermodynamics of chemical processes, such as chemical reactions, one can make use of the mathematical methods of Josiah Willard Gibbs [25]. The Gibbs free energy of a system is defined as:

$$G = H - TS, \tag{2.19}$$

where H is the enthalpy, S is the entropy, and T is the temperature in units of kelvin. The change in the free energy of the system that occurs during a reaction measures the balance between the enthalpy and the entropy. Under constant temperature and pressure, if the change in the Gibbs energy from state A to state B is negative, then state B is said to be thermodynamically more stable than state A. At $T = 0$K, the change in Gibbs energy equals the change in enthalpy, $\Delta G = \Delta H$. The change in enthalpy is defined as the change in the internal energy of the system, ΔU, plus the work that the system has done on its surroundings, $P\Delta V$. Since moreover

the change in PV for reactions involving solids is negligible, mostly it is sufficient to focus upon the change in energy, ΔU, where U corresponds to the ground state energy of a system as calculated by DFT.

2.7.2.a   Zero-Point Energy Contribution: ZPE

The lowest possible energy that a quantum mechanical physical system may have is called the zero-point energy (ZPE) [26–28]. It arises as a result of nuclear motions. In molecular systems, both the vibrational and the rotational motions contribute to the ZPE. In solids, only the vibrational motions contribute. Within the harmonic oscillator approximation, the contribution of vibrational energies to the total energy term is calculated using the following equation:

$$E^{vib} = \int \left\{ \frac{\hbar\omega}{2} + \hbar\omega n(\omega) \right\} g(\omega)d\omega, \qquad (2.20)$$

where $g(\omega)$ is the phonon density of states, and $n(\omega) = [e^{\frac{\hbar\omega}{k_B T}} - 1]^{-1}$ is the Bose-Einstein occupation number. At zero Kelvin, the ZPE contribution to the total energy is given by the first term of Eq. 2.20 alone, whereas the second term represents the finite temperature contributions. Vibrational contributions to the entropy term can also be calculated when finite temperature results are demanded.

The numerical calculation of ZPE can be accomplished using a dynamical matrix which is constructed via small displacements of atoms from their equilibrium positions and finite differencing the accumulated forces. Each atom inside the cell is symmetrically displaced in its three degrees of freedom, by $dr = \pm 0.01 \mathring{A}$. To account for the spatial range of the dynamical matrix the calculations require large supercells. ZPE contributions to the calculated total energies are considerable for light elements such as hydrogen. For heavy elements the phonon frequencies are low and accordingly the ZPEs are negligible.

2.7.3   Kinetics

Thermodynamic calculations focus only on the initial and final states of a system and the path by which a change takes place is not taken into account. Intuitively, one might expect strongly exothermic reactions to occur spontaneously, but this is often not true, since many potentially favorable reactions are prohibited by substantial energy barriers. To have a better understanding of how chemical reactions take place, methods based on Transition State Theory (TST) [29] can be used. In principle, the transition rate between two stable equilibria is determined by the lowest energy barrier, also called the reaction barrier (RB). The nudged elastic band method (NEB), which is proposed by Jónsson and Henkelman [30–33], is one of the suitable ways to calculate the RBs. Once the transition states and the RBs are known, other important factors relevant to chemical kinetics, such as, diffusion rates k, and constants D, can be obtained from a vibrational analysis.

The set up of a NEB calculation starts with a discrete representation of a path from the initial reactant configuration to the final product configuration. The coordinates

of atoms for the initial and final configurations are kept fixed during the calculation. Based on these two stable structures, several intermediate configurations (the so called images) are generated using a straight line interpolation. An optimization algorithm is then applied to these images, so that they are relaxed down towards the minimum energy path (MEP). A refinement of MEP and accordingly a more accurate value for the RB is obtained by using denser set of images during calculations. The details on theoretical background of the NEB method as well as its comparison to other saddle point searching methods can be obtained in Refs. [30–34]

2.7.4   Density of States: DOS

The number of states at each energy level that are available to be occupied is called the density of states (DOS). A zero DOS for an energy level means that no states can be occupied. On contrary, a high DOS for an energy level represents that many states are available for occupation. DOS delivers invaluable information about the bonding within solids and in classification of materials as metallic, semiconductor or insulators. Metals or semi metals have non-localized electrons and no gap (separation between valence and conduction band). Materials with a large gap ($\geq 4\,\mathrm{eV}$) are called insulators, whereas systems with a smaller gap are categorized as semiconductors. In the representation of DOS the specific relation between ϵ and $\mathbf{k}$ must be known to convert between energy and wavevector [18, 19]. In the case of a parabolic relation, such as applies to free electrons, or to electrons in a solid with an isotropic parabolic band structure, the energy is related to the wavevector as: $\epsilon = \frac{\hbar^2}{2m} k^2$. Accordingly, the density of states in three dimensions is given by,

$$D(\epsilon) = \frac{1}{2\pi^2} \cdot \left(\frac{2m}{\hbar^2} \right)^{3/2} \cdot \epsilon^{1/2}. \tag{2.21}$$

Although DFT seems to systematically underestimate the band gap in insulators and semiconductors by about $30-40\%$, it is successful in reproducing the shape of the DOS.

2.7.5   Charge Analysis

In order to make a quantitative conclusion, the identification of the amount of electrons on a particular atom would be useful. However, there is no unique way to extract the number of electrons that are associated with a particular atom in a molecule, or in a solid. Many different schemes have been proposed, some are based on population analysis of wave functions (Mulliken population analysis [35], Coulson's charges [36]), and some others are based on partitioning of electron density distributions (Bader analysis[37], Hirshfeld analysis [38]). The charge density analysis of the materials discussed in this thesis are performed via the Bader analysis [39, 40]. In this approach, molecules or solids are partitioned into atomic volumes, such that the flux of the gradient of the electron density vanishes at every point on the surfaces. That is for every point $\mathbf{r}_s$ on the surface S($\mathbf{r}_s$),

$$\nabla n(\mathbf{r}_s) \cdot u(\mathbf{r}_s) = 0, \tag{2.22}$$

where $u(\mathbf{r}_s)$ is the unit vector normal to the surface at $\mathbf{r}_s$. The charge density reaches a minimum between atoms, which defines a natural location to separate the atoms from each other. The electron density used in a Bader analysis is obtained via self consistent static DFT calculations based on the equilibrium structure.

2.7.6 Electron Localization Function: ELF

Introduced by Becke and Edgecombe [41] and later adapted to DFT by Savin [42, 43], the electron localization function (ELF) provides a topological description of chemical bonding. ELF is a measure of the likelihood of finding an electron in the neighborhood space of a reference electron with the same spin, located at a given point. It is applicable to a variety of systems including molecules and solids. In principle, an approximate extraction of the ELF is possible from the experimental electron density that is measured in accurate X-ray diffraction experiments [44, 45]. However, it is more directly obtained from quantum mechanical calculations. Keeping in mind that the electron density is given by the single particle wave functions as shown in Eq. 2.6, Savin's interpretation the ELF is defined as:

$$\text{ELF} = \left\{ \left[\frac{T(\mathbf{r})}{T_h(\mathbf{r})} \right]^2 + 1 \right\}^{-1}, \tag{2.23}$$

where, $T(\mathbf{r})$ is the excess local kinetic energy due to Pauli exclusion principle,

$$T(\mathbf{r}) = \frac{1}{2} \sum_i |\nabla \Psi_i(\mathbf{r})|^2 - \frac{|\nabla n(\mathbf{r})|^2}{8n(\mathbf{r})}, \tag{2.24}$$

and $T_h(\mathbf{r})$ is the Thomas-Fermi kinetic energy density, such that

$$T_h(\mathbf{r}) = \frac{3}{10}(3\pi^2)^{2/3} n(\mathbf{r})^{5/3}. \tag{2.25}$$

The numerical values of ELF vary between 0 and 1, where the value 1 means perfect localization of electrons. A value of 0.5 corresponds to the electron gas. The most elegant way to analyze ELF is via a graphical representation in form of iso-surfaces and cut planes. Although the correlation between ELF and chemical bonding is sort of topological, ELF is found to be useful in distinguishing between ionic and covalent type of interactions in materials.

Bibliography

[1] M. L. Born and R. Oppenheimer, Ann. Phys. **84**, 457 (1927).

[2] P. Hohenberg and W. Kohn, Phys. Rev. **136**, B864 (1964).

[3] L. H. Thomas, Proc. Cambridge Philos. Soc. **23**, 542 (1927).

[4] E. Fermi, Z. Phys. **48**, 37 (1928).

[5] W. Kohn and L. J. Sham, Phys. Rev. **140**, A1133 (1965).

[6] D. M. Ceperley and B. J. Alder, Phys. Rev. Lett. **45**, 566 (1980).

[7] J. P. Perdew and A. Zunger, Phys. Rev. B **23**, 5048 (1981).

[8] J. P. Perdew *et al.*, Phys. Rev. B **46**, 6671 (1992).

[9] J. P. Perdew, K. Burke, and M. Ernzerhof, Phys. Rev. Lett. **77**, 3865 (1996).

[10] J. P. Perdew, K. Burke, and M. Ernzerhof, Phys. Rev. Lett. **78**, 1396 (1997).

[11] D. R. Hamann, M. Schlüter, and C. Chiang, Phys. Rev. Lett. **43**, 1494 (1979).

[12] G. B. Bachelet, D. R. Hamann, and M. Schlüter, Phys. Rev. B **26**, 4199 (1982).

[13] N. Troullier and J. L. Martins, Phys. Rev. B **43**, 1993 (1991).

[14] D. Vanderbilt, Phys. Rev. B **41**, 7892 (1990).

[15] K. Laasonen, A. Pasquarello, R. Car, C. Lee, and D. Vanderbilt, Phys. Rev. B **47**, 10142 (1993).

[16] P. E. Blöchl, Phys. Rev. B **50**, 17953 (1994).

[17] G. Kresse and D. Joubert, Phys. Rev. B **59**, 1758 (1999).

[18] N. W. Ashcroft and N. D. Mermin, *Solid State Physics* (Thomson Learning, Inc., 1976).

[19] C. Kittel, *Introduction to Solid State Physics* (New York: John Wiley & Sons, Inc., 1996).

[20] H. J. Monkhorst and J. D. Pack, Phys. Rev. B **13**, 5188 (1976).

[21] G. Kresse and J. Hafner, Phys. Rev. B **47**, 558 (1993).

[22] G. Kresse and J. Furthmüller, Phys. Rev. B **54**, 11169 (1996).

[23] M. Methfessel and A. T. Paxton, Phys. Rev. B **40**, 3616 (1989).

[24] P. E. Blöchl, O. Jepsen, and O. K. Andersen, Phys. Rev. B **49**, 16223 (1994).

[25] J. W. Gibbs, *Elementary Principles in Statistical Mechanics* (C. Scribner's sons, 1902).

[26] A. Einstein and L. Hopf, Ann. Phys. **33**, 1096 (1910).

[27] A. Einstein and L. Hopf, Ann. Phys. **33**, 1005 (1910).

[28] A. Einstein and O. Stern, Ann. Phys. **40**, 551 (1913).

[29] P. Atkins and J. de Paula, *Atkins' Physical Chemistry* (New York: Oxford University Press Inc., 2002).

[30] H. Jónsson, G. Mills, and K. W. Jacobsen, *Nudged Elastic Band Method for Finding Minimum Energy Paths of Transitions, in Classical and Quantum Dynamics in Condensed Phase Simulations* (Singapore: World Scientific, 1998).

[31] G. Henkelman and H. Jónsson, J. Chem. Phys. **113**, 9978 (2000).

[32] G. Henkelman, B. P. Uberuaga, and H. Jónsson, J. Chem. Phys. **113**, 9901 (2000).

[33] D. Sheppard, R. Terrell, and G. Henkelman, J. Chem. Phys. **128**, 134106 (2008).

[34] R. A. Olsen, G. J. Kroes, G. Henkelman, A. Arnaldsson, and H. Jónsson, J. Chem. Phys. **121**, 9776 (2004).

[35] R. S. Mulliken, J. Chem. Phys. **23**, 1833 (1955).

[36] J. Meister and W. H. E. Schwarz, J. Phys. Chem. **98**, 8245 (1994).

[37] R. Bader, *Atoms in Molecules: A Quantum Theory.* (USA: Oxford University Press, 1994).

[38] F. L. Hirshfeld, Theor. Chim. Acta **44**, 129 (1977).

[39] G. Henkelman, A. Arnaldsson, and H. Jónsson, Comput. Mater. Sci. **36**, 354 (2006).

[40] E. Sanville, S. D. Kenny, R. Smith, and G. Henkelman, J. Comput. Chem. **28**, 899 (2007).

[41] A. D. Becke and K. E. Edgecombe, J. Chem. Phys. **92**, 5397 (1990).

[42] M. Kohout and A. Savin, J. Comput. Chem. **18**, 1431 (1997).

[43] A. Savin, THEOCHEM **727**, 127 (2005).

[44] W. H. E. Schwarz and B. Müller, Chem. Phys. Lett. **166**, 621 (1990).

[45] V. Tsirelsos and A. Stash, Chem. Phys. Lett. **351**, 142 (2002).

Part − A
Atomic Hydrogen Storage

Chapter 3

Hydrogen storage in magnesium-transition metal compounds

3.1 Abstract

Magnesium-dihydride (MgH_2) stores 7.7 weight % hydrogen, but it suffers from a high thermodynamic stability and slow (de)hydrogenation kinetics. Alloying Mg with lightweight transition metals (TM = Sc, Ti, V, Cr) aims at improving the thermodynamic and kinetic properties. We study the structure and stability of $Mg_xTM_{1-x}H_2$ compounds, $x = $ [0-1], by first-principles calculations at the level of density functional theory. We find that the experimentally observed sharp decrease in hydrogenation rates for $x \gtrsim 0.8$ correlates with a phase transition of $Mg_xTM_{1-x}H_2$ from a fluorite to a rutile phase. The stability of these compounds decreases along the series Sc, Ti, V, Cr. Varying the transition metal (TM) and the composition x, the formation enthalpy of $Mg_xTM_{1-x}H_2$ can be tuned over the substantial range $0 - 2$ eV/f.u. Assuming however that the alloy Mg_xTM_{1-x} does not decompose upon dehydrogenation, the enthalpy associated with reversible hydrogenation of compounds with a high magnesium content ($x = 0.75$) is close to that of pure Mg.

3.2 Introduction

Hydrogen is a clean energy carrier and an alternative to carbon based fuels in the long run. [1] Mobile applications require a compact, dense and safe storage

of hydrogen with a high-rate loading and unloading capability. [2, 3] Lightweight metal hydrides could satisfy these requirements. [4, 5] Metal hydrides are formed by binding hydrogen atoms in the crystal lattice, resulting in very high volumetric densities. Reasonable hydrogen gravimetric densities in metal hydrides can be achieved if lightweight metals are used.

MgH_2 has been studied intensively since it has a relatively high hydrogen gravimetric density of 7.7 wt. %. Bottlenecks in the application of MgH_2 are its thermodynamic stability and slow (de)hydrogenation kinetics. These lead to excessively high operating temperatures ($573 - 673$ K) for hydrogen release. [6–8] The hydrogen (de)sorption rates can be improved by decreasing the particle size down to nanoscales. [9–11] It is predicted that particles smaller than 1 nm have a markedly decreased hydrogen desorption enthalpy, which would lower the operating temperature.[12] The production of such small particles is nontrivial, however, and the hydrogen (de)sorption rates of larger nanoparticles are still too low.

An additional way of improving the (de)hydrogenation kinetics of MgH_2 is to add transition metals (TMs).[9, 13–15] Usually only a few wt. % is added, since TMs are thought to act as catalysts for the dissociation of hydrogen molecules. Recently however, Notten and co-workers have shown that the (de)hydrogenation kinetics is markedly improved by adding more TM and making alloys $Mg_x TM_{(1-x)}$, TM=Sc, Ti, $x \lesssim 0.8$. [16–26] The basic ansatz is that the rutile crystal structure of MgH_2 enforces an unfavorably slow diffusion of hydrogen atoms. [27] ScH_2 and TiH_2 have a fluorite structure, which would be more favorable for fast hydrogen kinetics. By adding a sufficiently large fraction of these TMs one could force the $Mg_x TM_{(1-x)}$ compound to adopt the fluorite structure.

In this paper we examine the structure and stability of $Mg_x TM_{(1-x)} H_2$, TM = Sc, Ti, V, Cr, compounds by first-principles calculations. In particular, we study the relative stability of the rutile versus the fluorite structures. This paper is organized as follows. In Sec. 3.3 we discuss the computational details. The calculations are benchmarked on the TMH_2 simple hydrides. The structure and formation enthalpies of the compounds $Mg_x TM_{(1-x)} H_2$ are studied in Sec. 3.4 and an analysis of the electronic structure is given. We discuss the hydrogenation enthalpy of the compounds in Sec. 3.5 and summarize our main results in Sec. 3.6.

3.3   Computational Methods and Test Calculations

We perform first-principles calculations at the level of density functional theory (DFT) with the PW91 functional as the generalized gradient approximation (GGA) to exchange and correlation. [28] As transition metals have partially filled $3d$ shells we include spin polarization and study ferromagnetic and simple antiferromagnetic orderings where appropriate. A plane wave basis set and the projector augmented wave (PAW) formalism are used, [29, 30] as implemented in the VASP code. [31, 32] The cutoff kinetic energy for the plane waves is set at 650 eV. The total energies

of MgH$_2$, TMH$_2$ and the hydrogen molecule are then converged to within 1 meV. Standard frozen core potentials are applied for all the elements, except for Sc, where we include $3s$ and $3p$ as valence shells, in addition to the usual $4s$ and $3d$ shells. The Brillouin zone (BZ) is integrated using a regular **k**-point mesh with a spacing ~ 0.02 Å^{-1} and the Methfessel-Paxton scheme with a smearing parameter of 0.1 eV. [33] The self-consistency convergence criterion for the energy difference between two consecutive electronic steps is set to 10^{-5} eV. Structural optimization is assumed to be complete when the total force acting on each atom is smaller than 0.01 eV/Å. The volumes of the unit cells are relaxed, and, where appropriate, also their shapes. Finally, we calculate accurate total energies for the optimized geometries using the linear tetrahedron method. [34]

To calculate the formation enthalpies of the metal hydrides we consider the following reaction.

$$x\mathrm{Mg} + (1-x)\mathrm{TM} + \mathrm{H}_2(g) \longrightarrow \mathrm{Mg}_x\mathrm{TM}_{(1-x)}\mathrm{H}_2. \tag{3.1}$$

The formation enthalpies (at $T = 0$) are then obtained by subtracting the total energies of the reactants from that of the product. A cubic box of size 10 Å is applied for the H$_2$ molecule. The calculated H$-$H bond length, binding energy, and vibrational frequency are 0.748 Å, -4.56 eV and 4351 cm^{-1}, respectively, in good agreement with the experimental values of 0.741 Å, -4.48 eV and 4401 cm^{-1}. [35, 36]

Since hydrogen is a light element, the zero point energy (ZPE) due to its quantum motion, is not negligible. We find that the correction to the reaction enthalpies of Eq. (3.1) resulting from the ZPEs, is 0.15$\pm$0.05 eV/H$_2$, as function of the composition x and the transition metal TM. Since we are mainly interested in relative formation enthalpies, we omit the ZPE energy correction in the following.

Before discussing the Mg$_x$TM$_{(1-x)}$H$_2$ compounds we benchmark our calculations on the simple compounds MgH$_2$ and TMH$_2$. Under standard conditions magnesium-dihydride has the rutile structure, α-MgH$_2$, see Fig. 4.1, with space group P4$_2$/mnm (136) and Mg and H atoms in the $2a$ and $4f$ ($x = 0.304$) Wyckoff positions, respectively. Each Mg atom is coordinated octahedrally by H atoms, with two Mg-H distances of 1.94 Å and four distances of 1.95 Å. First row early transition metal hydrides crystallize in the fluorite structure, α-TMH$_2$, see Fig. 4.1, with space group Fm$\overline{3}$m (225) and TM atoms in $4a$ and H atoms in $8c$ Wyckoff positions. Each TM has a cubic surrounding of H atoms with calculated TM-H bond lengths of 2.07, 1.92, 1.82 and 1.79 Å for Sc, Ti, V, and Cr, respectively. By breaking the cubic symmetry by hand and reoptimizing the geometry we have confirmed that the fluorite structure indeed represents a stable minimum.
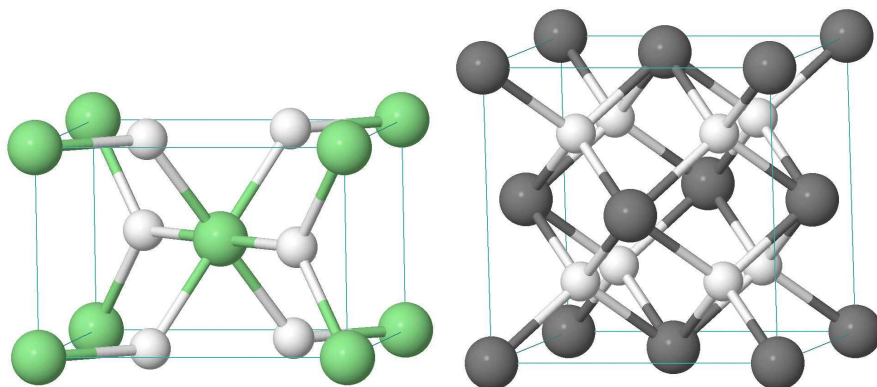
Figure 3.1: (Left) rutile crystal structure of α-MgH$_2$, and (right) fluorite crystal structure of α-TMH$_2$. The white spheres represent the hydrogen atoms.

The optimized cell parameters and the calculated formation enthalpies of the simple hydrides are given in Table 3.1. The structural parameters are in good agreement both with available experimental data and with previous DFT calculations.[37–39] The formation enthalpies of MgH$_2$ and VH$_2$ are somewhat underestimated by the calculations, whereas those of ScH$_2$ and TiH$_2$ are in excellent agreement with experiment. CrH$_2$ is predicted to be unstable with respect to decomposition.

3.4 Results Mg$_x$TM$_{(1-x)}$H$_2$

3.4.1 Structures and formation enthalpies

Mg$_x$TM$_{(1-x)}$H$_2$ has the fluorite structure for $x = 0$, and the rutile structure for $x = 1$. We want to establish which of the two structures is most stable at intermediate compositions x. First we summarize the current status of the experimental work on Mg$_x$TM$_{(1-x)}$ alloys.

Experimentally it has been demonstrated that Mg$_x$Sc$_{(1-x)}$ alloys can be reversibly hydrogenated, both in thin films, as well as in bulk form. [16, 17, 19, 20, 44, 45] Mg and Ti do not form a stable bulk alloy, but thin films of Mg$_x$Ti$_{(1-x)}$ have been made, which are readily and reversibly hydrogenated. [21–26, 46] Thin films of Mg$_x$V$_{(1-x)}$ and Mg$_x$Cr$_{(1-x)}$ can also be easily hydrogenated. [17] Attempts to produce non-equilibrium bulk Mg$_x$Ti$_{(1-x)}$ alloys by ball milling of Mg and Ti or their hydrides have had a limited success so far. [47–50] However, Mg$_7$TiH$_y$ crystals have been made using a high pressure anvil technique. [51] The same technique has been applied to

Table 3.1: Optimized cell parameters a (c), and calculated formation enthalpies E_f, of elemental dihydrides in their most stable (α) forms. All TMH$_2$ have a fluorite structure, space group Fm$\overline{3}$m (225), whereas MgH$_2$ has a rutile structure, space group P4$_2$/mnm (136).

| | a (c) | | E_f | |
| | (Å) | | (eV/f.u.) | |
Compound	Calc	Exp	Calc	Exp
MgH$_2$	4.494 (3.005)	4.501 (3.010)[a]	-0.66	-0.76
ScH$_2$	4.775	4.78[b]	-2.09	-2.08
TiH$_2$	4.424	4.454[c]	-1.47	-1.45
VH$_2$	4.210	4.27[d]	-0.65	-0.79
CrH$_2$	4.140	3.861[d]	$+0.13$[e]	-

[a]Reference [40]
[b]Reference [41]
[c]Reference [42]
[d]Reference [43]
[e]Antiferromagneticly ordered.

produce the hydrides Mg$_6$VH$_y$ and Mg$_3$CrH$_y$. [52–54]

The crystal structure of Mg$_x$Sc$_{(1-x)}$H$_y$ and Mg$_x$Ti$_{(1-x)}$H$_y$ in thin films, $x \lesssim 0.8$, $y \approx$ 1-2, is cubic, with the Mg and TM atoms at fcc positions. No detectable regular ordering of Mg and TM atoms at these positions has been found. [23, 44, 45] In contrast, the Mg and TM atoms form simple ordered structures in the high pressure phases. [51–55] The hydrogen atoms in Mg$_{0.65}$Sc$_{0.35}$H$_y$, $y \approx$ 1-2, assume tetrahedral interstitial positions, as is expected for the fluorite structure. [44, 45] In the Mg$_7$TiH$_{16}$ high pressure phase the metal atoms are in fcc positions and are ordered as in the Ca$_7$Ge structure. [51] The H atoms are in interstitial sites, but displaced from their ideal tetrahedral positions. [55]

The latter structure can be used as a starting point to construct simple, fluorite-type structures for Mg$_x$TM$_{(1-x)}$H$_2$, $0 < x < 1$. For $x = 0.125, 0.875$ we use the Ca$_7$Ge structure to order the metal atoms, for $x = 0.25, 0.75$ the Cu$_3$Au ($L1_2$) structure, and for $x = 0.5$ the CuAu ($L1_0$) structure. The H atoms are placed at or close to tetrahedral interstitial positions. As the atomic volumes of the various TM atoms differ, in each of the structures and compositions the cell parameters are optimized, as well as the positions of all atoms within the cell. Care is taken to allow for breaking the symmetry in the atomic positions. In particular the hydrogen atoms

are often displaced from their ideal tetrahedral positions. Although these structures are then no longer ideal fluorite structures anymore, we still use the term fluorite in the following. To model $Mg_x TM_{(1-x)} H_2$ in rutile-type structures we use the α-MgH_2 structure as a starting point. We replace a fraction x of the Mg atoms by TM atoms and use the smallest supercell of the rutile structure where this leads to an integer number of atoms. In case of multiple possible cells, the results given below refer to the cell that leads to the lowest energy. Again we allow for symmetry breaking and optimize the cell parameters and the atomic positions.

To asses the effect of disorder in the positions of the metal atoms we performed test calculations on special quasi-random structures of $Mg_x Ti_{(1-x)} H_2$, which enable to model random alloys in a finite supercell. For instance, we use a 32 atom supercell to model quasi-random structures of fcc $Mg_x Ti_{1-x}$ for $x = 0.25$, 0.5, and 0.75, and a 64 atom supercell for $x = 0.125$ and 0.875.[56] Inserting hydrogen atoms in tetrahedral interstitial positions then gives supercells with a total number of atoms of 96 and 192, respectively. The cell parameters are optimized, as well as the atomic positions.[57] The formation energies according to Eq. (3.1) of $Mg_x Ti_{(1-x)} H_2$ in these quasi-random structures, are within ~ 0.1 eV/f.u. lower than those of the simple ordered structures. In particular, the relative stability of the fluorite vs. the rutile structures is not sensitive to the relative ordering of the metal atoms. It is reasonable to expect that this also holds for the other $Mg_x TM_{(1-x)} H_2$ compounds.

The calculated volumes $V(Mg_x TM_{(1-x)} H_2)$ of the (simple) fluorite structures, normalized per formula unit (f.u.), are shown in Fig. 3.2. The volumes of the quasi-random structures of $Mg_x Ti_{(1-x)} H_2$ are within 1% of those of the simple structures. The volumes of a few bulk compounds and compositions can be extracted from experimental data, thus providing a check on the calculations. Interpolating the results in Ref. [44] gives $V(Mg_{0.65} Sc_{0.35} H_2) = 27.5$ Å^3, whereas the interpolated calculated value from Fig. 3.2 is 26.9 Å^3. Ref. [55] gives $V(Mg_{0.875} Ti_{0.125} H_2) = 27.3$ Å^3, compared to the calculated value 26.6 Å^3. These differences between experimental and calculated volumes are consistent with the differences between experimental and calculated lattice parameters of the simple hydrides, see Table 3.1. Experiments on thin films give $V(Mg_{0.7} Ti_{0.3} H_2) = 26.4$ Å^3, if one assumes cubic symmetry. [23] The interpolated computational value is 24.4 Å^3. The difference between these values is not excessively large, but considering the smaller difference found for the bulk composition $Mg_{0.875} Ti_{0.125} H_2$, it may suggest that the structure of thin films is slightly different from that of bulk.

The trends observed in Fig. 3.2 can be interpreted straightforwardly. The cell volumes of α-ScH_2 and the cubic β-MgH_2 structure [58] are within 1.4% of one

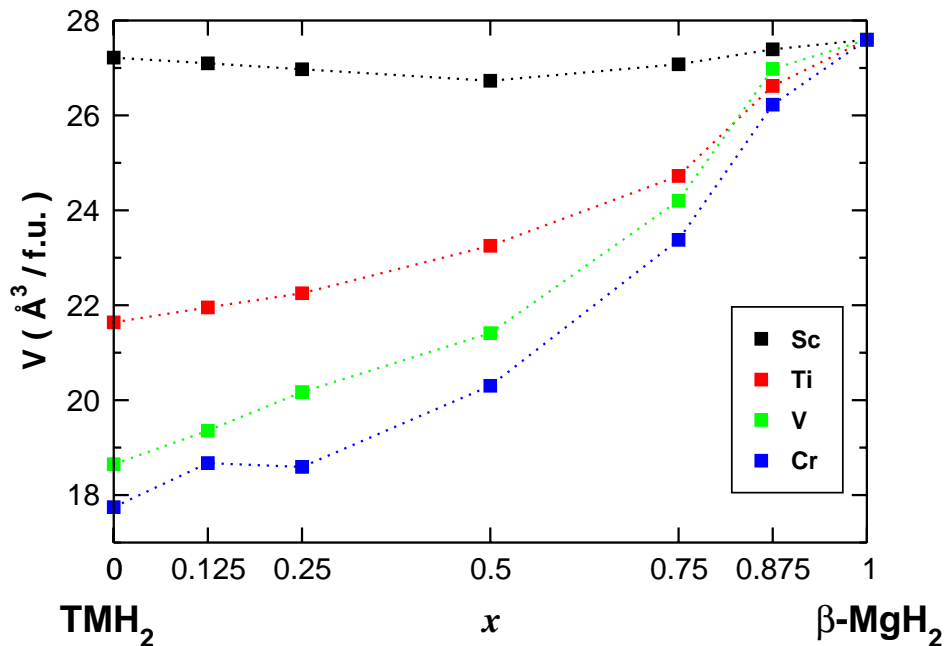**Figure 3.2:** The volumes per formula unit in Å^3 of $Mg_x TM_{(1-x)} H_2$ in the fluorite structure, as a function of the composition x for TM = Sc, Ti, V, Cr (from top to bottom).

another, which explains why the volumes calculated for $Mg_x Sc_{(1-x)} H_2$ only weakly depend on the composition x. The cell volumes of the other TMH_2 are smaller, hence one expects the volumes $V(Mg_x TM_{(1-x)} H_2)$ to increase with x. At fixed composition x, the volumes $V(Mg_x TM_{(1-x)} H_2)$ decrease along the series Sc, Ti, V, Cr, as the atomic volumes of the TMs decrease correspondingly. According to Zen's law of additive volumes one would expect [59]

$$V(Mg_x TM_{(1-x)} H_2) = x V(\beta\text{-}MgH_2) + (1-x) V(TMH_2). \tag{3.2}$$

The curves shown in Fig. 3.2 deviate slightly, but distinctly, from straight lines, with a maximum deviation of ~ 5 %. This deviation is consistent with the experimental observations on $Mg_x Ti_{(1-x)} H_2$. [21, 23] It is also observed in simple metal alloys. [59]

The calculated formation enthalpies of $Mg_x TM_{(1-x)} H_2$ are shown in Fig. 4.6.

Clearly for all TMs the fluorite structure is more stable than the rutile structure for all x smaller than a critical value, x_c. The critical composition x_c at which the rutile structure becomes more stable, as obtained by interpolation in Fig. 4.6, is in the range $x_c \approx 0.8$-0.85 for all TMs. The exact position of the critical composition x_c depends somewhat on the details of the structure. For quasi-random structures of $Mg_x Ti_{(1-x)} H_2$ the critical composition is at $x_c = 0.875$.[57] The fact that the critical composition is fairly high might be guessed from the energies of the fluorite and rutile structures of the simple hydrides. As a first estimate of the critical composition x_c below which the fluorite structure is stable one may try a linear interpolation between the pure TMH_2 compounds, $x = 0$, and MgH_2, $x = 1$. The rutile structure of TMH_2 is more unstable than the fluorite structure by $\Delta(TMH_2) = 0.75, 0.65, 0.68, 0.36$ eV/f.u. for TM = Sc, Ti, V, Cr, respectively. The difference in formation enthalpy between the α (rutile) and β (cubic) phases of MgH_2 is $\Delta(MgH_2) = 0.10$ eV/f.u. Linear interpolation then gives $x_c = \Delta(TMH_2)/(\Delta(TMH_2) + \Delta(MgH_2))$, which results in $x_c \approx 0.9$ for Sc, Ti and V, and $x_c = 0.8$ for Cr. Whereas these values may seem a good first guess, they are somewhat too high as compared to the crossing points x_c observed in Fig. 4.6. Moreover, as this figure shows, in particular the curves for Ti and V are far from linear, so the results for the linear interpolation may be somewhat fortuitous.

Experimental results indicate that $Mg_{0.7} Ti_{0.3} H_2$ has the fluorite structure and $Mg_{0.9} Ti_{0.1} H_2$ has the rutile structure. [23] This agrees with the results shown in Fig. 4.1, where a fluorite to rutile phase transition takes place at the composition $x = x_c \approx 0.83$. It has been suggested that the fluorite structure allows for a much faster kinetics of hydrogen loading and unloading. Experimentally it has been observed that the dehydrogenation kinetics of $Mg_x Sc_{(1-x)}$ and $Mg_x Ti_{(1-x)}$ becomes markedly slower if $x \gtrsim x_0 = 0.8$. The results shown in Fig. 4.1 suggest that $x_0 = x_c$, i.e. the composition at which the phase transition between fluorite and rutile structures takes place.

The dehydrogenation kinetics of $Mg_x Ti_{(1-x)}$ also becomes gradually slower with decreasing x, for $x < x_c$, i.e. where the compound remains in the fluorite structure, although it is still faster than for $x > x_c$. [19, 21] Whereas kinetic studies are beyond the scope of the present paper, we speculate that a volume effect might play a role here. In the fluorite structure the hydrogen atoms occupy interstitial positions close to the tetrahedral sites. Diffusion of hydrogen atoms is likely to take place via other interstitial sites such as the octahedral sites. The smaller the volume, the shorter the distance between such sites and the occupied positions, or in other words, the shorter the distance between a diffusing hydrogen atom and other hydrogen atoms in
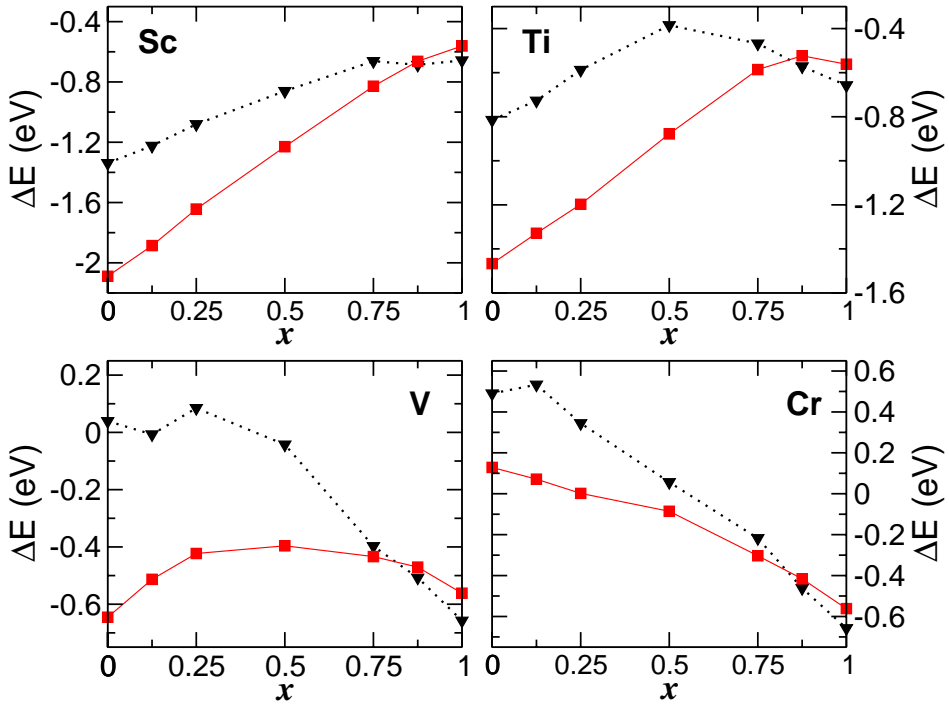
Figure 3.3: The formation enthalpy (per formula unit) of the $Mg_x TM_{(1-x)}H_2$ compounds as obtained from spin polarized calculations. The values for the fluorite and rutile structures are represented by squares (solid lines) and triangles (dashed lines), respectively.

the lattice. This may increase the barrier for diffusion. As the volume of $Mg_x V_{(1-x)}$ and $Mg_x Cr_{(1-x)}$ is smaller than that of $Mg_x Sc_{(1-x)}$ and $Mg_x Ti_{(1-x)}$ (at the same composition x), this might also explain why the dehydrogenation kinetics of the former compounds is much slower. [17] We note that the smaller volume of $Mg_x V_{(1-x)}$ and $Mg_x Cr_{(1-x)}$ is accompanied by a distortion of the structures consistent with the limited space available to accommodate the hydrogen atoms. For instance, in $Mg_{0.75}V_{0.25}H_2$ and $Mg_{0.75}Cr_{0.25}H_2$ the hydrogen atoms are displaced considerably from the tetrahedral positions, and the coordination number of V and Cr (by hydrogen) is 7, instead of 8 as in case of a perfect fluorite structure.

3.4.2   Electronic structure

To analyze the electronic structure of the compounds $Mg_xTM_{(1-x)}H_2$, we start with the density of states (DOS) of the pure hydrides α-MgH_2 and TMH_2 as shown in Fig. 3.4. The bonding in MgH_2 is dominantly ionic; occupied hydrogen orbitals give the main contribution to the valence states, whereas the conduction bands have a significant contribution from the Mg orbitals. [60] As usual, ionic bonding between main group elements results in an insulator with a large band gap. In contrast, the transition metal dihydrides are metallic, as demonstrated by Fig. 3.4. The peak in the DOS at low energy, i.e. between -9 and -2 eV in ScH_2 to between -12 and -4 eV in CrH_2, is dominated by hydrogen states. The broad peak around the Fermi level consists of transition metal d-states. It suggests that bonding in TMH_2 is at least partially ionic. The TM s-electrons are transferred to the H atoms, whereas the d-electrons largely remain on the TM atoms. The DOSs of TMH_2, TM=Sc, Ti, V, Cr, are very similar in shape. As the number of d-electrons increases from one in Sc to four in Cr, the Fermi level moves up the d-band in this series. As the DOS at the Fermi level increases, it enhances the probability of a magnetic instability. Indeed we find CrH_2 to be antiferromagnetic with a magnetic moment of $1.5\mu_B$ on the Cr atoms. The antiferromagnetic ordering is 51 meV/f.u. more stable than the ferromagnetic ordering, which is 7 meV/f.u. more stable than the non-polarized solution. In the other TMH_2 we do not find magnetic effects.

Additional information on the type of bonding can be obtained from a Bader charge analysis. [61] In α-MgH_2 the Bader charges are $Q_{Mg} = +1.59e$ (and $Q_H = -0.80e$, since the compound is neutral), which confirms that this compound is dominantly ionic. The results for TMH_2 are shown in Table 3.2. They indicate that the ionicity in ScH_2 is comparable to that in MgH_2. Furthermore, the ionicity decreases along the series Sc, Ti, V and CrH_2. Comparison to Table 3.1 shows that the decrease in ionicity correlates with a decrease in formation enthalpy.

These results on the simple hydrides help us to analyze the electronic structure and bonding in $Mg_xTM_{(1-x)}H_2$. We show results for the fluorite structure only, since that is the more stable structure over most of the composition range. As an example, Fig. 3.4 shows the calculated DOSs of $Mg_{0.75}TM_{0.25}H_2$. One can qualitatively interpret these DOSs as a superposition of the DOSs of MgH_2 and TMH_2. The bonding states at low energy, comprising the first broad peak in the DOS, consist mainly of filled hydrogen states. The peaks close to the Fermi level are dominated by TM d-states. The Fermi level moves up the d-band through the series Sc, Ti, V, Cr. At higher energy we find the (unoccupied) Mg s states. The basic structure of the DOSs remains the same for all compositions $Mg_xTM_{(1-x)}H_2$. As x increases, the TM d
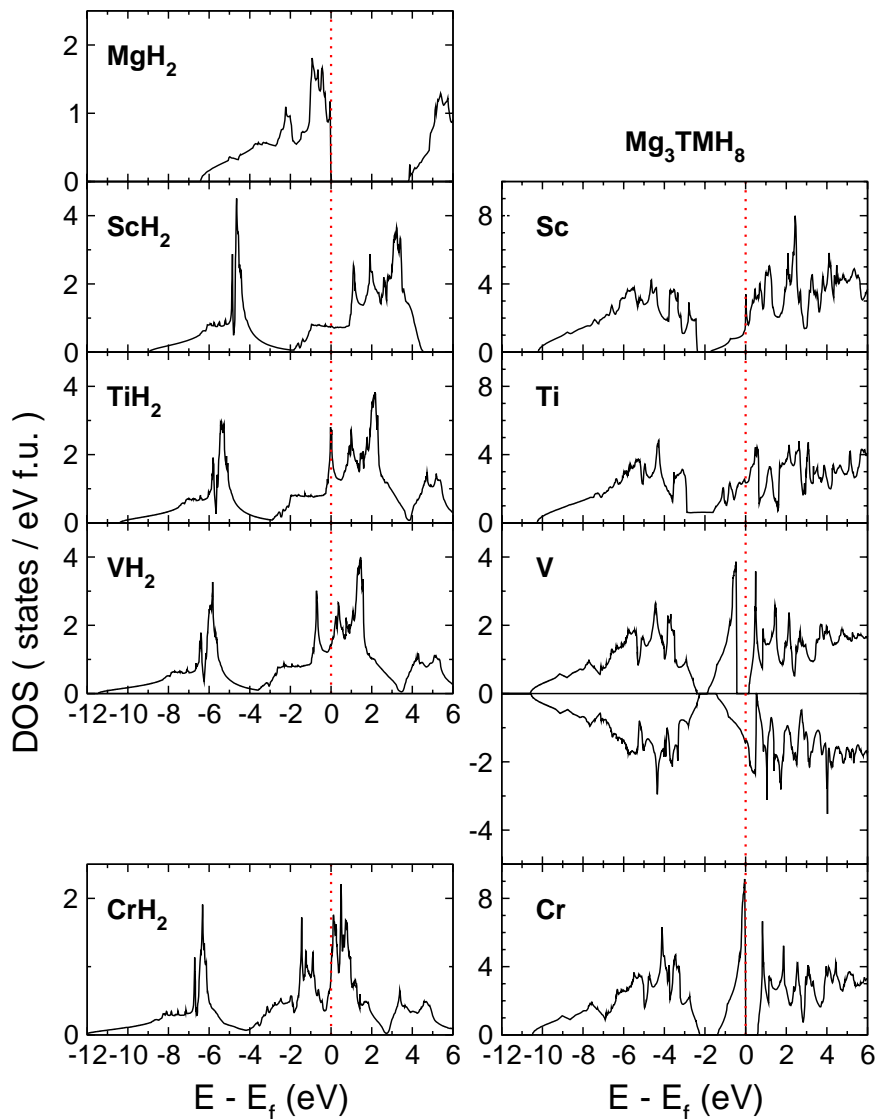
Figure 3.4: Densities of states of MgH_2 and TMH_2 (left column) and of $Mg_{0.75}TM_{0.25}H_2$ (right column) for TM = Sc, Ti , V, Cr. The shaded areas give the projected densities of states on the TM d orbitals. For CrH_2 the nonmagnetic DOS is given for simplicity reasons; CrH_2 is antiferromagnetic (see text).

contribution of course decreases. In addition, the TM d-peak becomes narrower with increasing x, as the distance between the TM atoms increases.

Narrowing of the d peak can give rise to magnetic instabilities. The tendency to such instabilities increases along the series Sc, Ti, V and Cr. The development of nonzero magnetic moments of course strongly depends upon the structure. Nevertheless, for $Mg_xSc_{(1-x)}H_2$ and $Mg_xTi_{(1-x)}H_2$ we see a tendency to form magnetic moments on the TMs only if $x \gtrsim 0.8$. For $Mg_xV_{(1-x)}H_2$ this occurs if $x \gtrsim 0.5$, and for $Mg_xCr_{(1-x)}H_2$ one can find magnetic instabilities over the whole composition range. Most of the structures have a finite DOS at the Fermi level, which, might indicate a metallic behavior. One cannot conclude this on the basis of a DOS alone, however, but should also critically evaluate possible localization and on-site correlation effects. There are a few exceptions. In particular cases low spin states can be more stable, such as for $Mg_{0.75}Cr_{0.25}H_2$ in the fluorite structure. Cubic crystal field splitting by the hydrogens surrounding the Cr atom results in a gap between e_g and t_{2g} states, the e_g states being lowest in energy. The latter are filled by the four d electrons of Cr, which makes this particular structure insulating, see Fig. 3.4. The DOS of $Mg_{0.75}V_{0.25}H_2$ in the fluorite structure is explained by the same mechanism. However, as V only has three d electrons, each V atom obtains a magnetic moment of $1 \mu_B$. The distance between the TM atoms is fairly large in most compositions that have nonzero magnetic moments, which suggests a small magnetic coupling between the TM atoms, a low Néel or Curie temperature, and paramagnetic behavior at room temperature. Exceptions are the Cr compounds with a substantial amount of Cr, as discussed above.

A Bader charge analysis of $Mg_xTM_{(1-x)}H_2$ can be made, similar to the simple hydrides. For all compositions $Q_{Mg} \approx +1.6e$, i.e. close to the value found in α-MgH_2. As an example the Bader charges on the TM and H atoms in $Mg_{0.75}TM_{0.25}H_2$ are given in Table 3.2. The charge on the TM atoms decreases along the series Sc, Ti, V, and Cr as in the simple hydrides, but compared to the latter, it is somewhat smaller on V and Cr. The charges on the H atoms in $Mg_{0.75}TM_{0.25}H_2$ are roughly the proportional average of the charges on the H atoms in MgH_2 and TMH_2. The charge analysis of the $Mg_xTM_{(1-x)}H_2$ compounds is consistent with the bonding picture extracted from the DOSs.

3.5   Discussion

We discuss to what extend the Mg-TM alloys are suitable as hydrogen storage materials. The formation enthalpies of $Mg_xTM_{(1-x)}H_2$ are shown in Fig. 4.6.

Table 3.2: Bader charge analysis of TMH_2 and $Mg_{0.75}TM_{0.25}H_2$. All charges Q are given in units of e.

| | TMH$_2$ | | Mg$_{0.75}$TM$_{0.25}$H$_2$ | |
| | Q_{TM} | Q_H | Q_{TM} | Q_H |
TM	(e)	(e)	(e)	(e)
Sc	+1.51	−0.75	+1.57	−0.80
Ti	+1.17	−0.59	+1.18	−0.76
V	+1.09	−0.55	+0.98	−0.73
Cr	+0.89	−0.45	+0.68	−0.69

Lightweight materials require a high content of magnesium, but to have a stable fluorite structure it should not exceed the critical composition x_c, as discussed in Sec. 3.4.1. We focus upon the composition $Mg_{0.75}TM_{0.25}H_2$ in the following discussion. The calculated formation enthalpies are $-0.83, -0.59, -0.43$ and -0.30 eV/f.u. for TM = Sc, Ti, V, and Cr, respectively. For applications the binding enthalpy of hydrogen in the lattice should be $\lesssim 0.4$ eV/H$_2$,[2–4] which indicates that the Sc and Ti compounds are too stable. The formation enthalpies of the V and Cr compounds could be in the right range. However, the parameter that is most relevant for hydrogen storage is the hydrogenation enthalpy. Assuming that the alloy does not dissociate upon dehydrogenation, the hydrogenation enthalpy corresponds the reaction

$$Mg_x TM_{(1-x)} + H_2(g) \longrightarrow Mg_x TM_{(1-x)} H_2. \tag{3.3}$$

To assess the hydrogenation enthalpy, one can break down the formation enthalpy associated with Eq. (3.1) into components, similar to the decomposition used in Ref. [37]. We write the formation enthalpy as a sum of three terms. (i) The enthalpy required to make the Mg-TM alloy in the fcc structure from the elements in their most stable form. (ii) The energy required to expand the fcc lattice in order to incorporate the hydrogen atoms. (iii) The energy associated with inserting the hydrogen atoms. The results of this decomposition for $Mg_{0.75}TM_{0.25}H_2$ are given in Fig. 3.5. To facilitate the discussion, a similar decomposition is shown for the simple hydrides, where (i) only consists of transforming the pure metal into the fcc structure. In contrast to Ref. [37], we use the spin-polarized fcc alloy for calculating the contributions (i) and (ii), as this will make the extraction of the hydrogenation enthalpy easier. In the cases where the magnetic moment is nonzero, we study both ferromagnetic and antiferromagnetic ordering. As for the simple hydrides, Cr compounds generally have an antiferromagnetic ordering.

The lattice expansion energy (ii) of the compounds $Mg_{0.75}TM_{0.25}H_2$ is ≤ 0.1 eV for all TMs, see Fig. 3.5(b). It is in fact comparable to that of pure Mg, see Fig. 3.5(a). At the composition $Mg_{0.75}TM_{0.25}H_2$, the effect on the energy of changing the unit cell volume is dominated by Mg. For these compounds the lattice expansion only plays a minor role in the formation energy, in contrast to the simple hydrides, where the lattice expansion gives a significant contribution. The hydrogen insertion energies (iii) are also remarkably similar for the Sc, Ti, and V compounds. Again this is in sharp contrast to the corresponding energies for the simple hydrides, which strongly depend on the TM. The hydrogen insertion energies for the compounds are in fact similar to that of pure Mg. At the composition $Mg_{0.75}TM_{0.25}H_2$ also this energy is then dominated by Mg. Only the compound $Mg_{0.75}Cr_{0.25}H_2$ has a somewhat smaller hydrogen insertion energy. The reason for this is that the energy gained by magnetic ordering of the alloy $Mg_{0.75}Cr_{0.25}$ is relatively high, as compared to the other compounds. This contribution stabilizes the alloy with respect to the hydride, which is nonmagnetic.

The formation enthalpy of the fcc alloys $Mg_{0.75}TM_{0.25}$ (i) shows the largest variation as a function of the TM, relative to the contributions (ii) and (iii). Whereas the alloy formation energy is negative for TM = Sc, indicating that this alloy is stable, it is positive for Ti, V, and Cr, meaning that these alloys are unstable. This result agrees with the experimental finding that of the Mg-TM alloys considered here, only a stable Mg-Sc alloy exists in bulk form. The substantial increase of the alloy formation enthalpy in the series Sc, Ti, V, is largely responsible for the variation of the formation energy of the corresponding hydrides $Mg_{0.75}TM_{0.25}H_2$. The alloy formation energy of $Mg_{0.75}Cr_{0.25}$ is similar to that of $Mg_{0.75}V_{0.25}$, due to a relatively high spin-polarization energy, as discussed in the previous paragraph.

The hydrogenation enthalpy according to Eq. (3.3) can be determined by summing the contributions (ii) and (iii) of Fig. 3.5. Since the most stable structure of the alloys is not always the fcc structure, one should however subtract the energy required to convert the alloys from their most stable structure to an fcc structure. We find, for instance, that for $Mg_{0.75}Ti_{0.25}$ the fcc structure is 0.04 eV/f.u. less stable than the hcp structure. Indeed thin film experiments on $Mg_xTi_{(1-x)}$ yield an hcp structure.[19, 23] For $Mg_{0.75}Sc_{0.25}$ the fcc structure is more stable than the hcp structure by 0.05 eV/f.u..

The calculated hydrogenation enthalpy of $Mg_{0.75}Sc_{0.25}$ is -0.79 eV/f.u., in good agreement with the experimental value of -0.81 eV/f.u..[19] The calculated hydrogenation enthalpy of $Mg_{0.75}Ti_{0.25}$ is -0.76 eV/f.u., which is in good agreement with the experimental value of -0.81 eV/f.u. of Ref. [26], obtained if the thin film cor-
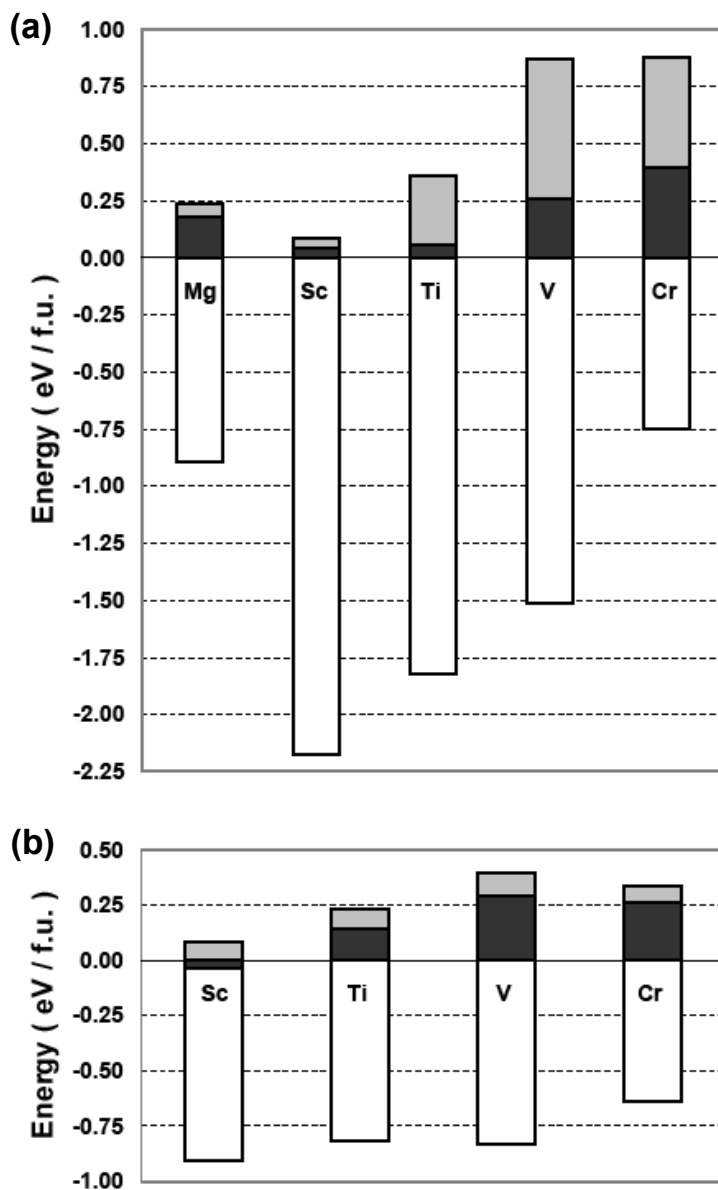
Figure 3.5: Decomposition of the formation energy into (i) the formation energy of the spin-polarized fcc metal $Mg_{0.75}TM_{0.25}$ (black), (ii) the lattice expansion energy (gray), and (iii) the hydrogen insertion energy (white); (a) the simple hydrides MgH_2, TMH_2; (b) $Mg_{0.75}TM_{0.25}H_2$.

rection suggested there is included. These hydrogenation enthalpies are remarkably similar to that of pure Mg, strongly suggesting that alloying Mg with these TMs does not improve this energy as compared to pure Mg. The most stable structures of $Mg_{0.75}TM_{0.25}$, TM = V, Cr, are not known, but judging from the Sc and Ti compounds the energy difference between the fcc and the most stable structures will be small. Neglecting this energy difference upper bounds for the hydrogenation enthalpies of $Mg_{0.75}V_{0.25}$ and $Mg_{0.75}Cr_{0.25}$ are -0.72 and -0.57 eV/f.u., respectively. Again this indicates that alloying Mg with these TMs does not improve the hydrogenation enthalpy substantially.

3.6   Summary

In summary, we have studied the structure and stability of $Mg_xTM_{(1-x)}H_2$, TM = Sc, Ti, V, Cr, compounds by first-principles calculations. We find that for $x < x_c \approx 0.8$ the fluorite structure is more stable than the rutile structure, whereas for $x > x_c$ the rutile structure is more stable. The density of states of these compounds is characterized by the valence bands being dominated by contributions from the hydrogen atoms, whereas the TMs have partially occupied d states around the Fermi level. As x increases and/or one moves down the TM series, the tendency to magnetic instabilities increases.

The formation enthalpy of $Mg_xTM_{1-x}H_2$ can be tuned over a substantial range, i.e. 0-2 eV/f.u., by varying TM and x. To a large part this reflects the variation of the formation enthalpy of the alloy $Mg_xTM_{(1-x)}$, however. Assuming that the alloys do not decompose upon dehydrogenation, the hydrogenation enthalpy then shows much less variation. For compounds with a high magnesium content ($x = 0.75$) it is close to that of pure Mg. Introducing a third metallic element may however be used to significantly improve the thermodynamics of (de)hydrogenation. The study of ternary alloys of Mg with transition metals and/or simple metals is actively pursued at present.[24, 62–64]

The phase transition from the rutile to the fluorite structure in $Mg_xTM_{(1-x)}H_2$, if x falls below the critical composition x_c, correlates with the experimentally observed speeding up of the (de)hydrogenation kinetics in these compounds. A discussion of the kinetics is beyond the scope of the present paper. However, our preliminary calculations indicate that even in MgH_2, hydrogen diffusion in the cubic (fluorite derived) β-MgH_2 phase is much faster than in the rutile α-MgH_2 phase, both through a smaller formation energy for a hydrogen vacancy, as well as through a lower barrier for vacancy diffusion.

Acknowledgments

Bibliography

[1] See the special issue *Toward a Hydrogen Economy*, by R. Coontz and B. Hanson, Science **305**, 957 (2004).

[2] A. Züttel, Materials Today **6**, 24 (2003).

[3] A. Züttel, Naturwissenschaften **91**, 157 (2004).

[4] L. Schlapbach and A. Züttel, Nature **414**, 353 (2001).

[5] B. Bogdanovic, M. Felderhoff, S. Kaskel, A. Pommerin, K. Schlichte, and F. Schuth, Adv. Mater. **15**, 1012 (2003).

[6] J. F. Stampfer, Jr., C. E. Holley, Jr., and J. F. Suttle, J. Am. Chem. Soc. **82**, 3504 (1960).

[7] J. Huot, G. Liang, and R. Schulz, Appl. Phys. A: Mater. Sci. Process. **72**, 187 (2001).

[8] W. Grochala and P. P. Edwards, Chem. Rev. **104**, 1283 (2004).

[9] A. Zaluska, L. Zaluski, and J. O. Ström-Olsen, Appl. Phys. A: Mater. Sci. Process. **72**, 157 (2001).

[10] M. Dornheim, N. Eigen, G. Barkhordarian, T. Klassen, and R. Bormann, Adv. Eng. Mater. **8** (2006).

[11] W. Li, C. Li, H. Ma, and J. Chen, J. Am. Chem. Soc. **129**, 6710 (2007).

[12] R. W. P. Wagemans, J. H. van Lenthe, P. E. de Jongh, A. J. van Dillen, and K. P. de Jong, J. Am. Chem. Soc. **127**, 16675 (2005).

[13] J. F. Pelletier, J. Huot, M. Sutton, R. Schulz, A. R. Sandy, L. B. Lurio, and S. G. J. Mochrie, Phys. Rev. B **63**, 52103 (2001).

[14] F. von Zeppelin, H. Reule, and M. Hirscher, J. Alloys Compd. **330**, 723 (2002).

[15] X. Yao, C. Wu, A. Du, G. Q. Lu, H. Cheng, S. C. Smith, J. Zou, and Y. He, J. Phys. Chem. B **110**, 11697 (2006).

[16] P. H. L. Notten, M. Ouwerkerk, H. van Hal, D. Beelen, W. Keur, J. Zhou, and H. Feil, J. Power Sources **129**, 45 (2004).

[17] R. A. H. Niessen and P. H. L. Notten, Electrochem. Solid-State Lett. **8**, A534 (2005).

[18] R. A. H. Niessen and P. H. L. Notten, J. Alloys Compd. **404**, 457 (2005).

[19] W. P. Kalisvaart, R. A. H. Niessen, and P. H. L. Notten, J. Alloys Compd. **417**, 280 (2006).

[20] R. A. H. Niessen, P. Vermeulen, and P. H. L. Notten, Electrochim. Acta **51**, 2427 (2006).

[21] P. Vermeulen, R. A. H. Niessen, and P. H. L. Notten, Electrochem. Commun. **8**, 27 (2006).

[22] D. M. Borsa, A. Baldi, M. Pasturel, H. Schreuders, B. Dam, R. Griessen, P. Vermeulen, and P. H. L. Notten, Appl. Phys. Lett. **88**, 241910 (2006).

[23] D. Borsa, R. Gremaud, A. Baldi, H. Schreuders, J. Rector, B. Kooi, P. Vermeulen, P. Notten, B. Dam, and R. Griessen, Phys. Rev. B **75**, 205408 (2007).

[24] P. Vermeulen, E. F. M. J. van Thiel, and P. H. L. Notten, Chem. Eur. J. **13**, 9892 (2007).

[25] W. P. Kalisvaart, H. J. Wondergem, F. Bakker, and P. H. L. Notten, J. Mater. Res **22**, 1640 (2007).

[26] R. Gremaud, C. P. Broedersz, D. M. Borsa, A. Borgschulte, P. Mauron, H. Schreuders, J. H. Rector, B. Dam, and R. Griessen, Adv. Mater. **19**, 2813 (2007).

[27] K. H. J. Buschow, P. C. P. Bouten, and A. R. Miedema, Reports on Progress in Physics **45**, 937 (1982).

[28] J. P. Perdew, K. Burke, and M. Ernzerhof, Phys. Rev. Lett. **77**, 3865 (1996).

[29] P. E. Blöchl, Phys. Rev. B **50**, 17953 (1994).

[30] G. Kresse and D. Joubert, Phys. Rev. B **59**, 1758 (1999).

[31] G. Kresse and J. Hafner, Phys. Rev. B **47**, 558 (1993).

[32] G. Kresse and J. Furthmüller, Phys. Rev. B **54**, 11169 (1996).

[33] M. Methfessel and A. T. Paxton, Phys. Rev. B **40**, 3616 (1989).

[34] P. E. Blöchl, O. Jepsen, and O. K. Andersen, Phys. Rev. B **49**, 16223 (1994).

[35] K. P. Huber and G. Herzberg, *Molecular Spectra and Molecular Structure. IV. Constants of Diatomic Molecules* (Van Nostrand Reinhold Co., 1979).

[36] J. D. Cox, D. D. Wagman, and V. A. Medvedev, *CODATA Key Values for Thermodynamics* (Hemisphere Publ., 1989).

[37] K. Miwa and A. Fukumoto, Phys. Rev. B **65**, 155114 (2002).

[38] C. Wolverton, V. Ozolins, and M. Asta, Phys. Rev. B **69**, 144109 (2004).

[39] L. Zhang, Y. Wang, T. Cui, Y. Li, Z. He, Y. Ma, and G. Zou, Phys. Rev. B **75**, 144109 (2008).

[40] M. Bortz, B. Bertheville, G. Bottger, and K. Yvon, J. Alloys Compd. **287**, L4 (1999).

[41] W. M. Mueller, J. P. Blackledge, and G. G. Libowitz, *Metal Hydrides* (Academic Press, New York, 1968).

[42] P. Villars, L. D. Calvert, and W. B. Pearson, *Pearson's Handbook of Crystallographic Data for Intermetallic Phases* (ASM International, Materials Park, OH, USA, 1991).

[43] C. A. Snavely and D. A. Vaughan, J. Am. Chem. Soc. **71**, 313 (1949).

[44] M. Latroche, W. P. Kalisvaart, and P. H. L. Notten, J. Solid State Chem. **179**, 3024 (2006).

[45] P. C. M. M. Magusin, W. P. Kalisvaart, P. H. L. Notten, and R. A. van Santen, Chem. Phys. Lett. **456**, 55 (2008).

[46] P. Vermeulen, R. A. H. Niessen, D. M. Borsa, B. Dam, R. Griessen, and P. H. L. Notten, Electrochem. Solid-State Lett. **9**, A520 (2006).

[47] G. Liang, J. Huot, S. Boily, A. V. Neste, and R. Schulz, J. Alloys Compd. **292**, 247 (1999).

[48] J. L. Bobet, C. Even, Y. Nakamura, E. Akiba, and B. Darriet, J. Alloys Compd. **298**, 279 (2000).

[49] G. Liang and R. Schulz, J. Mater. Sci. **38**, 1179 (2003).

[50] Y. J. Choi, J. Lu, H. Y. Sohn, and Z. Z. Fang, J. Power Sources **180**, 491 (2008).

[51] D. Kyoi, T. Sato, E. Rönnebro, N. Kitamura, A. Ueda, M. Ito, S. Katsuyama, S. Hara, D. Noréus, and T. Sakai, J. Alloys Compd. **372**, 213 (2004).

[52] D. Kyoi, E. Rönnebro, N. Kitamura, A. Ueda., M. Ito, S. Katsuyama, and T. Sakai, J. Alloys Compd. **361**, 252 (2003).

[53] D. Kyoi, T. Sato, E. Rönnebro, Y. Tsuji, N. Kitamura, A. Ueda, M. Ito, S. Katsuyama, S. Hara, D. Noréus, et al., J. Alloys Compd. **375**, 253 (2004).

[54] E. Rönnebro, D. Kyoi, H. Blomqvist, D. Noréus, and T. Sakai, J. Alloys Compd. **368**, 279 (2004).

[55] E. Rönnebro, D. Kyoi, A. Kitano, Y. Kitano, and T. Sakai, J. Alloys Compd. **404**, 68 (2005).

[56] A. V. Ruban, S. I. Simak, S. Shallcross, and H. L. .Skriver, Phys. Rev. B **67**, 214302 (2003).

[57] S. Er, M. van Setten, G. de Wijs, and G. Brocks, in preparation (2009).

[58] P. Vajeeston, P. Ravindran, A. Kjekshus, and H. Fjellvåg, Phys. Rev. Lett. **89**, 175506 (2002).

[59] J. Hafner, J. Phys. F: Met. Phys. **15**, L43 (1985).

[60] M. J. van Setten, V. A. Popa, G. A. de Wijs, and G. Brocks, Phys. Rev. B **75**, 35204 (2007).

[61] G. Henkelman, A. Arnaldsson, and H. Jónsson, Comput. Mater. Sci. **36**, 354 (2006).

[62] M. J. van Setten, G. A. de Wijs, V. A. Popa, and G. Brocks, Phys. Rev. B **72**, 073107 (2005).

[63] M. J. van Setten, G. A. de Wijs, and G. Brocks, Phys. Rev. B **76**, 075125 (2007).

[64] C. P. Broedersz, R. Gremaud, B. Dam, R. Griessen, and O. M. Lovvik, Phys. Rev. B **77**, 024204 (2008).

Chapter 4

First principles modelling of magnesium titanium hydrides

4.1 Abstract

Mixing Mg with Ti leads to a hydride $Mg_xTi_{(1-x)}H_2$ with markedly improved (de)hydrogenation properties for $x \lesssim 0.8$, as compared to MgH_2. Optically, thin films of $Mg_xTi_{(1-x)}H_2$ have a black appearance, which is remarkable for a hydride material. In this paper we study the structure and stability of $Mg_xTi_{(1-x)}H_2$, $x = 0\text{-}1$ by first-principles calculations at the level of density functional theory. We give evidence for a fluorite to rutile phase transition at a critical composition $x_c = 0.8\text{-}0.9$, which correlates with the experimentally observed sharp decrease in (de)hydrogenation rates at this composition. The densities of states of $Mg_xTi_{(1-x)}H_2$ have a peak at the Fermi level, composed of Ti d states. Disorder in the positions of the Ti atoms easily destroys the metallic plasma, however, which suppresses the optical reflection. Interband transitions result in a featureless optical absorption over a large energy range, causing the black appearance of $Mg_xTi_{(1-x)}H_2$.

4.2 Introduction

Hydrogen promises to be a good candidate to replace carbon based fuels in the future [1]. The current inability to store hydrogen in a safe and sufficiently dense form obstructs its use in vehicles or in portable applications. A practical means of

storage should yield a system that operates at moderate temperatures and releases hydrogen fast enough to feed a fuel cell [2]. Storage should be reversible and the dehydrogenated system should adsorb hydrogen sufficiently fast. Typical target numbers for gravimetric and volumetric hydrogen densities in storage systems are 6 weight % (wt%) and 0.045 kg/L.

The highest volumetric hydrogen densities among all possible storage forms are achieved in metal hydrides, where atomic hydrogen is bonded in the crystal lattice of bulk metals or alloys [3, 4]. Reasonable gravimetric hydrogen densities can be obtained if lightweight metals are used. For instance, the simple dihydride MgH_2 has a gravimetric hydrogen density of 7.7 wt%. However, MgH_2 is so stable that releasing hydrogen at a pressure of 1 bar requires a temperature of around 300ºC [5], which is impractically high for use in combination with PEM fuel cells. Moreover, the (de)hydrogenation kinetics of MgH_2 is poor. Surface processes can hamper the kinetics, as the dissociation rate of hydrogen molecules on a Mg surface is small [6], and surface oxidation leads to the formation of a hydrogen diffusion barrier [7]. The surface kinetics can be improved by annealing [8] and by adding a catalyst [9]. Experimental studies also claim that the (de)hydrogenation kinetics of bulk MgH_2 is very slow. It has been suggested that the kinetics is hampered by the rutile crystal structure of α-MgH_2 [10–12].

It is well known that 3d transition metals (TMs) act as catalysts to improve the surface kinetics of hydrogen adsorption in Mg [13]. To obtain this improvement usually only a few wt% of TM is added to Mg. Recently it has been shown that also the bulk (de)hydrogenation kinetics can be improved markedly by adding TMs. One has to add a substantially larger amount, however, and make alloys $Mg_xTM_{(1-x)}$ with TM = Sc, Ti and $x \lesssim 0.8$ [10–12]. The hydrides of these alloys have a cubic crystal structure quite unlike the α-MgH_2 rutile structure [14–17]. Obviously, to preserve a high gravimetric hydrogen density it is essential to use lightweight TMs. As Sc is too expensive to be used on a large scale, Ti is then the obvious choice. Thin $Mg_xTi_{(1-x)}$ films, prepared by various experimental techniques, can be reversibly hydrogenated and dehydrogenated [12, 18–20]. The (de)hydrogenation kinetics is fast and increases gradually for alloys with increasing Mg content x, until a maximum at $x \approx 0.8$. If the Mg content is larger than this value, the kinetics becomes much slower.

Recent experimental studies reveal that Mg-Ti-H thin films have interesting optical properties, which may lead to applications of these compounds other than hydrogen storage [19–21]. In the dehydrogenated state the films are highly reflective, whereas upon hydrogenation they become black, i.e. they have a low reflection and high absorption for light in the visible range. This would allow them to be used as switch-

able smart coatings for solar panels, or as hydrogen sensors to detect the presence of hydrogen gas, for instance.

Despite the experimental interest in Mg-Ti hydrides, obtaining structural data has proven to be difficult as so far the bulk compounds have resisted synthesis under normal conditions. The only bulk Mg-Ti-H compound synthesized so far is Mg_7TiH_{16}, obtained by letting the dihydrides MgH_2 and TiH_2 react under extreme conditions of high pressure (8 GPa) and temperature (873 K) [22, 23]. In contrast, thin films of $Mg_xTi_{(1-x)}H_2$ can be readily obtained for any composition x by various deposition techniques. The limited amount of data on the structure, the thermodynamic stability and the electronic properties of Mg-Ti-H compounds has motivated the present first-principles computational study on $Mg_xTi_{(1-x)}H_2$.

First we consider the simple dihydrides MgH_2 and TiH_2 and subsequently characterize the properties of $Mg_xTi_{(1-x)}H_2$, focusing on the relative stability of possible cubic and rutile crystal structures. Limited first-principles calculations on ordered structures have indicated that a cubic fluorite-like crystal structure of $Mg_xTM_{(1-x)}H_2$ is more stable than the rutile structure for a range of early TMs and $x \lesssim 0.8$ [24, 25]. Here we focus on TM = Ti and study such structures in more detail, including the effects of disorder in the positions of the metal atoms, which is relevant for the experimental thin film studies. Our results suggest that the observed change in kinetics as a function of Mg content, is associated with a change in crystal structure. Finally, we calculate the optical properties of $Mg_xTi_{(1-x)}H_2$ and analyze them in terms of the compounds' structure and electronic structure. We show that the optical black state, which makes these compounds unique among the reversible hydrides so far, is an intrinsic property [26], unlike similar optical states of other Mg-TM-H thin films, which are caused by multiphase inhomogeneities in thin films [27, 28].

4.3 Computational Details

Most of the present calculations are performed at the level of the generalized gradient approximation (GGA) to density functional theory, using the projector augmented wave (PAW) technique and a plane wave basis set [29, 30], as implemented in the Vienna *Ab initio* Simulation Package (VASP) [31–33]. Standard frozen core PAW potentials are used and the H 1s, Mg 2s, Ti 4s and 3d shells are treated as valence shells. As Ti has a partially filled 3d shell we have considered the possibility of spin polarization and ferromagnetic or antiferromagnetic orderings. Unless otherwise mentioned explicitly, most of the compounds studied turn out to be paramagnetic, however. The main results are obtained using the Perdew Wang 91 (PW91) func-

tional [34], but we have also performed some tests with the hybrid DFT/Hartree-Fock schemes B3LYP and HSE06 [35–39].

We require that the total energy of each compound is converged to within 1 meV/atom with respect to the plane wave kinetic energy cutoff, which is assured by using a cutoff of 650 eV. Convergence with respect to the k-point sampling for the Brillouin zone (BZ) integration is tested independently on simple compounds using regular meshes of increasing density. We aim at converging total energies on a scale of 1 meV/atom. This is obtained with the following k-point meshes for the simple unit cells: $12\times12\times8$ for hcp unit cells, $16\times16\times16$ for cubic, fcc or fluorite, unit cells and $12\times12\times16$ for bct or rutile unit cells. In studying alloys and their hydrides we construct supercells of these simple unit cells and keep the same k-point grid. Thus employing the equivalent k-points method one avoids relative k-point sampling errors and maintains the accuracy for all cell sizes [40].

The molar volume of Ti (10.64 cm^3) is much smaller than that of Mg (14.00 cm^3), which makes finding the optimal cell parameters for $Mg_x Ti_{(1-x)}H_2$ non-trivial. We start by keeping the atomic fractional coordinates and the c/a ratio fixed and first carry out volume scans for each composition x and crystal type individually. Values for the lattice parameters are then estimated from the total energy minima. These are then used as starting values for a full optimization of each composition and crystal type.

The cell parameters, including the cell volume, and the atomic positions within the cells are optimized by minimizing the forces and stresses with the conjugate gradient algorithm [41]. During optimization Methfessel-Paxton smearing is used with a smearing parameter of 0.1 eV [42]. The criteria for self-consistency are set to 10^{-5} eV and 10^{-4} eV for the total energy differences between two consecutive electronic and ionic steps, respectively. Structural relaxation is assumed to be complete if all the forces acting on atoms are smaller than 1 meV/Å in the simple cell studies, and 10 meV/Å in the supercell studies. After the structures are optimized, the total energies are recalculated self-consistently with the tetrahedron method [43]. The latter technique is also used to calculate the electronic density of states (DOS).

The properties of the H$_2$ molecule are calculated in a cubic cell with cell parameter 10 Å, using Γ-point sampling. The calculated H$-$H bond length, binding energy, and vibrational frequency are 0.748 Å, -4.56 eV and 4351 cm^{-1}, respectively, in good agreement with the experimental values of 0.741 Å, -4.48 eV and 4401 cm^{-1} [44].

To study the stability of $Mg_x Ti_{(1-x)}H_2$ we look at the reaction

$$x\mathrm{Mg} + (1-x)\mathrm{Ti} + \mathrm{H}_2(\mathrm{gas}) \rightarrow \mathrm{Mg}_x\mathrm{Ti}_{(1-x)}\mathrm{H}_2 \qquad (4.1)$$

In principle one should consider the change in Gibbs free energy $G(T, P) = U +$

$PV - TS$ of this reaction. As the thermodynamic properties of hydrogen gas are well documented [45], one can focus upon the solid phases involved in the reaction. In addition, the temperature dependence of G of such solids tends to be relatively small over the temperature range of interest [46, 47]. A calculation of the change in enthalpy $H = U + PV$ at $T = 0$K should therefore be adequate to assess the relative stability of metal hydrides. Since moreover the PV contribution of solids can be neglected, it suffices to focus upon the change in energy U.

U corresponds to the total energy of a system as obtained in a DFT calculation. The positions of the atomic nuclei are then fixed, which corresponds to $T = 0$ K for classical particles. However, hydrogen is such a light atom that quantum vibrational energies give contributions to the total energies that are not negligible, even at $T = 0$ K. These zero-point energies (ZPEs) associated with atomic vibrations are obtained by solving the eigenvalue problem of the dynamical matrix [48]. Slightly displacing an atom from its equilibrium position creates forces on the other atoms. The dynamical matrix can then be constructed by displacing each atom at a time and finite differencing the forces. We use symmetric displacements $dr = \pm 0.01$ Å for each atom and its three degrees of freedom. These calculations are carried out in supercells to properly account for the spatial range of the dynamical matrix.

The ZPE corrected reaction energies are then calculated as

$$\Delta U^{\text{ZPE}} = \sum_p (U_p + U_p^{\text{vib}}) - \sum_r (U_r + U_r^{\text{vib}}), \qquad (4.2)$$

where r, p indicate the reactants and products of the reaction, respectively, U is the total energy obtained from a DFT calculation and U^{vib} is the vibrational ZPE. As it turns out, the ZPE corrections result in a rather constant shift of the reaction energy for the range of compounds studied here. Therefore, we frequently give the reaction energy as ΔU, calculated without $U_{p,r}^{\text{vib}}$ contributions, and mention the ZPE corrections separately.

As we will discuss in Sec. 4.5.1, we employ two different strategies to model the structures. The first strategy consists of constructing a set of relatively simple ordered structures, inspired by the experimental structure of Mg_7TiH_{16} [22, 23]. The structure of $Mg_xTi_{(1-x)}H_y$ as deposited in thin films is cubic with Mg and Ti atoms at fcc positions, but without a regular ordering of Mg and Ti atoms at these positions [15, 17]. To model such disordered structures, our second strategy consists of employing special quasi-random structures (SQSs), which enable to model random alloys in a finite supercell [49]. At each composition $Mg_xTi_{(1-x)}$ of interest, the Mg and Ti atoms are distributed such, that their lower order correlation functions are equal to those of a perfect random alloy [50, 51]. Hydrogen atoms are then inserted

into similar positions as in the simple structures. We use a set of SQSs for each crystal structure (fluorite or rutile) and composition, with a total number of atoms ranging from 48 to 192. Again all cell parameters are optimized, as well as the positions of all atoms within the cell.

To model the optical response of $Mg_x Ti_{(1-x)} H_2$ we calculate the dielectric function, consisting of interband and intraband contributions

$$\varepsilon(\omega) = \varepsilon_{\text{inter}}(\omega) + \varepsilon_{\text{intra}}(\omega), \tag{4.3}$$

which are calculated separately. The interband contribution $\varepsilon_{\text{inter}}$ is calculated in the independent particle approximation, using DFT eigenvalues and wave functions, i.e. neglecting exciton and local field effects. $\text{Im}[\varepsilon_{\text{inter}}(\omega)]$ is calculated directly via the standard longitudinal expression, and $\text{Re}[\varepsilon_{\text{inter}}(\omega)]$ is obtained by a Kramers-Kronig transform [26, 52, 53]. As optical data on hydrides are usually obtained from micro- and nano-crystalline samples whose crystallites have a significant spread in orientation, we use the directionally averaged dielectric function.

Many metals and metal alloys undergo a metal-insulator transition upon full hydrogenation [27, 28, 53–58]. $Mg_x Ti_{(1-x)} H_2$ however retains a finite DOS at the Fermi level. Hence intraband transitions contribute to the dielectric function. We model $\varepsilon_{\text{intra}}(\omega)$ by a standard free electron plasma model, with the plasma frequency calculated from the **k**-derivatives of the DFT eigenvalues [26, 59]. Once the full dielectric function $\varepsilon(\omega)$ is calculated, optical functions such as the extinction coefficient $\kappa(\omega)$ or the refractive index $n(\omega)$ are obtained via the standard expression

$$\varepsilon(\omega) = [n(\omega) + i\kappa(\omega)]^2 \tag{4.4}$$

4.4   Simple Dihydrides

As discussed in the introduction, experimental information on the structure of $Mg_x Ti_{(1-x)} H_2$ is limited, in particular concerning the positions of the hydrogen atoms. A sensible way to approach the problem is to assume that the structure is similar either to MgH_2 or to TiH_2. In this section we consider these simple dihydrides in more detail.

At standard temperature and pressure MgH_2 has the rutile structure, space group $P4_2/mnm$ (136), see figure 4.1. In this so-called α-MgH_2 phase, six hydrogen atoms surround each Mg atom in a distorted octahedron. The distance between Mg and two out of the six surrounding H atoms is 1.938 Å, and between Mg and the other four H
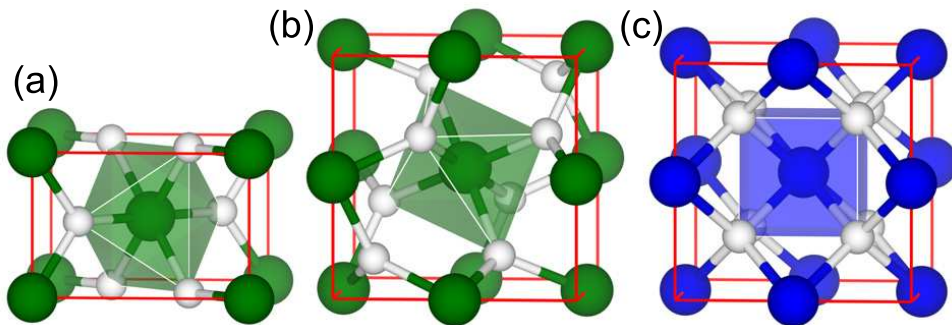
Figure 4.1: Crystal structures of α-MgH$_2$ (a), β-MgH$_2$ (b), and f-TiH$_2$ (c). Mg, Ti and H atoms are shown as green, blue and white coloured spheres, respectively; the polyhedra indicate the coordination of the metal atoms by hydrogens. The images are made using the VESTA software [60].

atoms it is 1.951 Å. Each H atom is in the centre of a triangle with Mg atoms at the vertices. Experimentally it has been shown that an increase in the temperature and pressure to 923 K and 4 GPa, converts α-MgH$_2$ to a cubic form, called β-MgH$_2$, with no further information about the positions of the H atoms [63]. DFT calculations have suggested a structure for β-MgH$_2$ [64]. Starting from a fluorite cubic structure with the hydrogen atoms on tetrahedral interstitial sites, space group Fm$\overline{3}$m (225), structural optimization gives a cubic structure with reduced symmetry, space group Pa$\overline{3}$ (205). This is accompanied by a decrease in the total energy of 0.24 eV/f.u. and a volume expansion of $\sim 4\%$. Each hydrogen atom is displaced from the centre of a tetrahedron to a base plane, where the coordination by Mg atoms is triangular with the three Mg atoms at a distance $d_1 = 1.911$ Å, similar to the α-phase. The fourth Mg atom of the original tetrahedron is at a distance $d_2 = 2.878$ Å. Each Mg atom is octahedrally coordinated by six H atoms at a distance d_1. An additional two H atoms are at d_2. At zero pressure the optimized β-MgH$_2$ structure is energetically unfavourable compared to the α-MgH$_2$ structure by 0.10 eV/f.u. and its volume is $\sim 9\%$ smaller. The optimized structural parameters obtained in our calculations are given in table 4.1. They are in good agreement with available experimental data.

The most stable phase of TiH$_2$ at standard temperature and pressure has the fluorite structure, space group Fm$\overline{3}$m (225), see figure 4.1, where the Ti atoms occupy the fcc lattice positions and hydrogen atoms reside at the tetrahedral interstitial positions. The calculated value of the Ti$-$H bond length is 1.916 Å. We call this the f-TiH$_2$ structure and to have a comparison between the two structural types of

Table 4.1: Calculated and experimental structural parameters of simple metals and hydrides.

Compound	Space group Unit cell (Å)			x	y	z
Mg	P6$_3$/mmc (194)	Mg	2c	1/3	2/3	1/4
	$a = 3.190$; $c = 5.180$					
exp.[61]	$a = 3.209$; $c = 5.210$	Mg	2c	1/3	2/3	1/4
Ti	P6$_3$/mmc (194)	Ti	2c	1/3	2/3	1/4
	$a = 2.916$; $c = 4.631$					
exp.[61]	$a = 2.951$; $c = 4.686$	Ti	2c	1/3	2/3	1/4
α-MgH$_2$	P4$_2$/mnm (136)	Mg	2a	0	0	0
	$a = 4.494$; $c = 3.005$	H	4f	0.3044	0.3044	0
exp.[62]	$a = 4.501$; $c = 3.010$	Mg	2a	0	0	0
		H	4f	0.3044	0.3044	0
β-MgH$_2$	Pa$\overline{3}$ (205)	Mg	4a	0	0	0
	$a = 4.796$	H	8c	0.3464	0.3464	0.3464
f-TiH$_2$	Fm$\overline{3}$m (225)	Ti	4a	0	0	0
	$a = 4.424$	H	8c	1/4	1/4	1/4
exp.[61]	$a = 4.454$	Ti	4a	0	0	0
		H	8c	1/4	1/4	1/4
r-TiH$_2$	P4$_2$/mnm (136)	Ti	2a	0	0	0
	$a = 3.991$; $c = 3.080$	H	4f	0.322	0.322	0

dihydrides we also construct a rutile form of TiH$_2$, and call it r-TiH$_2$ in table 4.1. This artificial rutile structure does not exist in nature to our knowledge. It has a 13% larger volume than f-TiH$_2$, and its total energy is 0.65 eV/f.u. higher.

The formation energies of the simple hydrides are defined as the reaction energies corresponding to (4.1) for $x = 0, 1$. The calculated values with and without vibrational ZPE corrections are given in table 4.2. ZPEs tend to destabilize the metal hydrides. By far the biggest contribution stems from the difference between the vibrational frequencies of the hydrogen atoms in the metal hydride and in the gas phase H$_2$ molecules. The ZPEs of the metals are small, i.e. 0.031 and 0.033 eV/atom for Mg and Ti, respectively (calculated with a 3×3×2 hcp supercell). In general, the more compact the metal hydride structure, the less space for the hydrogen atoms to vibrate, and the higher their vibrational frequencies and the ZPE are. The volumes per formula unit are 30.34 Å^3 for α-MgH$_2$ and 21.64 Å^3 for f-TiH$_2$. The calculated

Table 4.2: Calculated formation energies in eV without (ΔU) and with (ΔU^{ZPE}) vibrational zero point energy corrections, cf. (4.2), compared to experimental values (ΔU^{exp}). The latter are taken from [65] unless indicated otherwise.

Compound	ΔU	ΔU^{ZPE}	ΔU^{exp}		
α-MgH$_2$	-0.657	-0.558	-0.682	-0.694	-0.771
			-0.772 [66]	-0.779 [67]	
α-TiH$_2$	-1.467	-1.279	-1.297	-1.351	-1.378
			-1.450 [68]	-1.496	

Table 4.3: Calculated formation energies of α-MgH$_2$ in eV, obtained with different PAW pseudopotentials for Mg and different DFT functionals or hybrid DFT/Hartree-Fock schemes. The ZPE correction has been calculated at the PW91 level only.

Mg valence	functional	ΔU	ΔU^{ZPE}
3s	PW91	-0.657	-0.558
2p3s	PW91	-0.648	-0.549
3s	HSE06	-0.25	-0.15
3s	B3LYP	-0.95	-0.85

ZPEs are 0.406 eV/f.u. and 0.501 eV/f.u., respectively. These are calculated using a $2\times2\times3$ rutile supercell for MgH$_2$, containing 72 atoms, and a $2\times2\times2$ fluorite supercell for TiH$_2$, containing 96 atoms. The calculated ZPE of a H$_2$ molecule is 0.276 eV. Consequently, including ZPE corrections destabilizes α-MgH$_2$ by approximately 0.1 eV, whereas the more compact f-TiH$_2$ is destabilized by almost 0.2 eV, see table 4.2.

The experimental numbers obtained for the formation energy of TiH$_2$ range from -1.30 to -1.50 eV. The calculated numbers are in good agreement with these results. Experimental values of the formation energy of MgH$_2$ range from -0.68 to -0.78 eV. The calculated values overestimate these numbers somewhat, in particular if one includes ZPEs. Such differences between calculated and experimental formation energies are also found in other simple alkali and alkaline earth hydrides and seem to be typical for the use of GGA functionals such as PW91 or PBE. To see whether the calculated values can be improved, we test the use of a hard PAW pseudopotential for Mg, which includes the 2p shell as valence electrons, as well as the use of the hybrid DFT/Hartree-Fock schemes B3LYP and HSE06. The results, listed in table 4.3, show
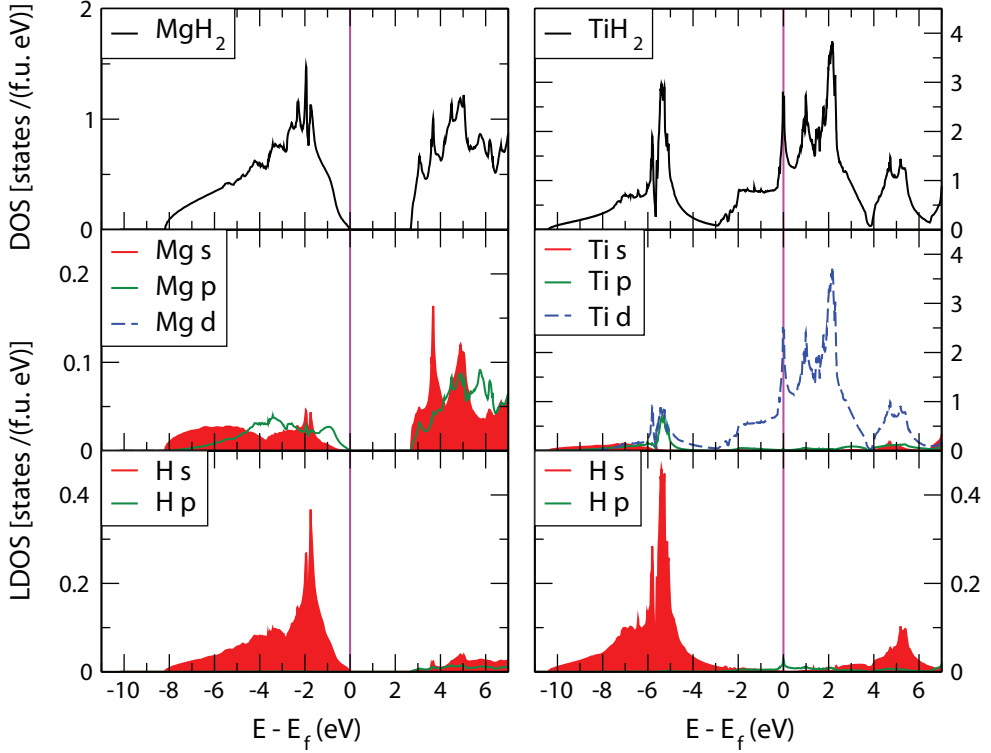
Figure 4.2: Electronic density of states (DOS) of β-MgH$_2$ and f-TiH$_2$. The origin of the energy scale is set at the top of the valence band. The top figure gives the total DOS, and the middle and bottom figures represent the local DOS, projected on the atoms; s, p and d contributions are shown in red, green and blue, respectively. The regions under the s curves are shaded and the d curves are dashed.

that the effect of using a hard PAW potential is minor. Hybrid DFT/Hartree-Fock schemes do not necessarily give an improvement over DFT/GGA functionals. The HSE06 and B3LYP schemes lead to formation energies of MgH$_2$ that are respectively much larger and somewhat smaller than the experimental one. Since in the following we are foremost interested in energy differences between crystal structures, we stick to using the PW91 GGA functional.

α-MgH$_2$ is an insulator with an experimental optical band gap of 5.6 eV [69]. As usual DFT calculations underestimate this gap [53]; the value obtained for α-MgH$_2$ is 3.8 eV, whereas the calculated gap for β-MgH$_2$ is 2.7 eV. The electronic (projected) densities of states ((P)DOS) of the cubic simple dihydrides β-MgH$_2$ and f-TiH$_2$ are

shown in figure 4.2. The fact that many fully hydrided simple metals and alloys are insulators can be understood from simple chemical arguments [53, 55–58]. The Mg atoms almost fully donate their valence (2s) electrons to the H atoms. Indeed the PDOS in figure 4.2 shows that the valence bands have a predominant H 1s character, whereas the Mg 2s states emerge in the conduction bands. In contrast, TiH_2 is metallic with a considerable DOS at the Fermi level. The PDOS shows that the states around the Fermi energy have a dominant Ti 3d character, whereas, as for MgH_2, the lower valence bands are dominantly H 1s. It suggests that in TiH_2 two electrons per metal atom are transferred to hydrogen and, as Ti atoms have four valence electrons ($s^2 d^2$), they remain in an open-shell configuration in the hydride. Figure 4.2 illustrates that the Ti d electrons participate significantly less than the s electrons to the bonding to H atoms.

4.5 $Mg_x Ti_{(1-x)} H_2$

4.5.1   Structures

The only detailed structure of $Mg_x Ti_{(1-x)} H_2$ available from experiment is for the composition $x = 0.875$. In the $Mg_7 TiH_{16}$ high pressure phase the metal atoms are in fcc positions and are ordered as in the $Ca_7 Ge$ structure [22, 23]. The H atoms are at interstitial sites, but displaced from their ideal tetrahedral positions. This structure has 96 atoms in the unit cell. We use it as a starting point to construct relatively simple, fluorite-type structures for other compositions x. For $x = 0.125, 0.875$ we use the $Ca_7 Ge$ structure to order the metal atoms, for $x = 0.25, 0.75$ the $Cu_3 Au$ ($L1_2$) structure, and for $x = 0.5$ the CuAu ($L1_0$) structure. The H atoms are placed at or close to tetrahedral interstitial positions. In each of the structures and compositions the cell parameters are optimized, as well as the positions of all atoms within the cell. Care is taken to allow for breaking the symmetry in the atomic positions, as the hydrogen atoms are often displaced from their ideal tetrahedral positions. Although strictly speaking such structures are then no longer ideal fluorite structures anymore, we still use the term fluorite in the following.

The optimized fluorite structures are given in table 4.4. Most of these structures are cubic, except $Mg_{0.5} Ti_{0.5} H_2$, which is tetragonally distorted. Comparing the calculated and the experimental structures of $Mg_{0.875} Ti_{0.125} H_2$ one observes that the calculated lattice parameter is 2% smaller than the experimental one. Although such a result is not uncommon for DFT calculations, note that the differences between calculated and experimental lattice parameters of MgH_2 and TiH_2 are much smaller,

Table 4.4: Optimized cell parameters and atomic positions of the fluorite-type simple $Mg_x Ti_{(1-x)} H_2$ structures.

Compound, Space group Unit cell (Å)			x	y	z
$Mg_{0.125}Ti_{0.875}H_2$	Mg	$4a$	0	0	0
$Fm\bar{3}m$ (225)	Ti1	$4b$	1/2	1/2	1/2
$a = 8.8896$	Ti2	$24d$	0	1/4	1/4
	H1	$32f$	0.1285	0.1285	0.1285
	H2	$32f$	0.3755	0.3755	0.3755
$Mg_{0.25}Ti_{0.75}H_2$	Ti	$3c$	0	1/2	1/2
$Pm\bar{3}m$ (221)	Mg	$1a$	0	0	0
$a = 4.4648$	H	$8g$	0.2566	0.2566	0.2566
$Mg_{0.5}Ti_{0.5}H_2$	Ti1	$1a$	0	0	0
$P4/mmm$ (123)	Ti2	$1c$	1/2	1/2	0
$a = 4.4720$	Mg	$2e$	0	1/2	1/2
$c = 4.6544$	H	$8r$	0.25	0.25	0.2352
$Mg_{0.75}Ti_{0.25}H_2$	Ti	$1a$	0	0	0
$Pm\bar{3}m$ (221)	Mg	$3c$	0	1/2	1/2
$a = 4.6208$	H	$8g$	0.2432	0.2432	0.2432
$Mg_{0.875}Ti_{0.125}H_2$	Ti	$4a$	0	0	0
$Fm\bar{3}m$ (225)	Mg1	$4b$	1/2	1/2	1/2
$a = 9.3565$	Mg2	$24d$	0	1/4	1/4
	H1	$32f$	0.1194	0.1194	0.1194
	H2	$32f$	0.3725	0.3725	0.3725
$Mg_{0.875}Ti_{0.125}H_2$ exp.[23]	H1	$32f$	0.094(2)	0.094(2)	0.094(2)
$a = 9.564(2)$	H2	$32f$	0.365(2)	0.365(2)	0.365(2)

see table 4.1. The Wyckoff positions and the hydrogen-metal coordinations of the calculated and experimental structures of $Mg_{0.875}Ti_{0.125}H_2$ agree, but the absolute difference between the calculated and experimental H positions is 0.1-0.4 Å. This is not a volume effect, since optimizing the structure using the experimental or the calculated lattice parameter gives the same H positions. We have also checked that breaking the symmetry by random displacement of the H atoms yields the same optimized $Fm\bar{3}m$ (225) structure. From our calculations the experimental structure is 0.766 eV/f.u. higher in energy.
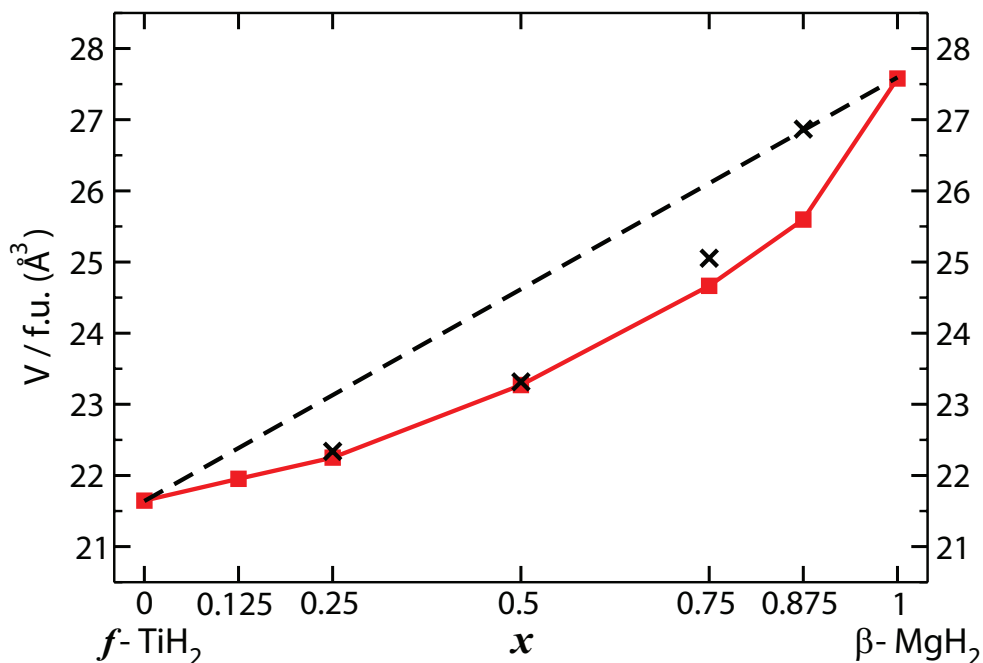
Figure 4.3: The volumes per formula unit (V/f.u) in $Å^3$ of $Mg_xTi_{(1-x)}H_2$ in the ordered fluorite structures, as a function of the composition x. The dashed line marks a linear interpolation between f-TiH_2 and β-MgH_2. The crosses mark the volumes of the special quasi-random structures.

The calculated tetrahedral environment of a H1 atom in $Mg_{0.875}Ti_{0.125}H_2$ consists of a Ti atom at a distance of 1.935 Å and three Mg2 atoms at 2.058 Å; the experimental distances are 1.557 Å and 2.293 Å, respectively. The calculated tetrahedral environment of a H2 atom consists of a Mg1 atom at 2.066 Å and three Mg2 atoms at 2.013 Å compared to experimental distances of 2.236 Å and 2.021 Å. The calculated H−Ti distance is close to the 1.916 Å found in TiH_2, see table 4.1, whereas the experimental distance is significantly smaller. In fact, for all compositions in table 4.4 we find H−Ti distances in the range 1.91-1.94 Å. From the calculated H−Mg distances one observes that the H atoms are closer to ideal tetrahedral positions than in the experimental structure. From the positions of the H2 atoms it is clear, however, that both the calculated and the experimental structure are closer to an ideal fluorite structure than to β-MgH_2.

One should note that the experimental structure of Mg_7TiH_{16} is based upon room temperature XRD data. As XRD measures the electronic charge distribution, mod-

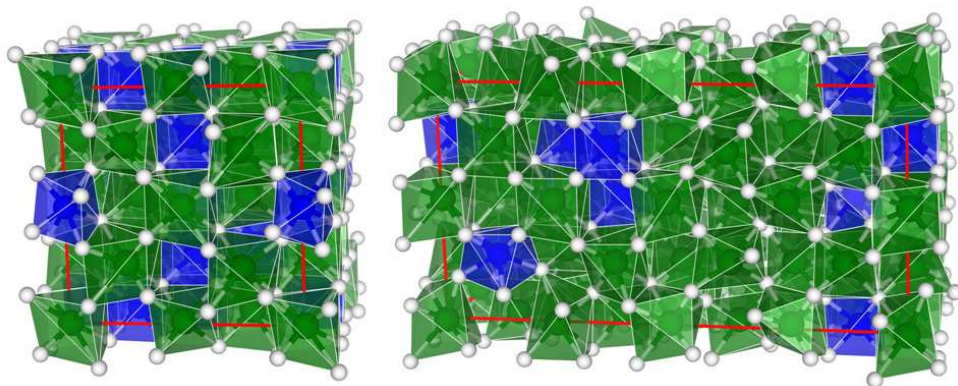**Figure 4.4:** Cells to model special quasi-random structures of $Mg_x Ti_{(1-x)} H_2$ for $x = 0.75$ (left image) and $x = 0.875$ (right image) compositions. Mg, Ti and H atoms are shown as green, blue and white coloured spheres, respectively; the polyhedra indicate the coordination of the metal atoms by hydrogens [60].

elling the data with atomic scattering functions introduces errors on the positions of light atoms such as hydrogen. In particular, the asymmetry in the hydrogen positions is sometimes exaggerated. In that case low temperature neutron diffraction can give a structure that is much closer to the calculated structure [46, 70].

The calculated volumes of the fluorite structures of $Mg_x Ti_{(1-x)} H_2$ as a function of the composition x, normalized per formula unit, are shown in figure 4.3. According to Zen's law of additive volumes one would expect a linear dependence [71]. The curves deviate slightly, but distinctly, from straight lines, with a maximum deviation of 5.4 % at $x = 0.5$. This deviation is consistent with the experimental observations on $Mg_x Ti_{(1-x)} H_2$ [12, 15]. It is also observed in simple metal alloys [71].

The binary phase diagram of Mg and Ti indicates that they do not form a stable bulk alloy. It is however claimed that synthesis by mechanical alloying may be possible [72]. In addition, thin films of $Mg_x Ti_{(1-x)}$ are readily made, which can be reversibly hydrogenated [10, 12, 15, 18–20]. The crystal structure of $Mg_x Ti_{(1-x)} H_y$ in thin films, $x \lesssim 0.8$, $y \approx$ 1-2, is cubic, with the Mg and Ti atoms at fcc positions, but no detectable regular ordering of Mg and Ti atoms at these positions [15, 17]. The positions of the H atoms have not been determined from experiment.

To model such disordered structures, we perform calculations on SQSs, which enable to model random alloys in a finite supercell. We use a 32 atom supercell to model SQSs of fcc $Mg_x Ti_{1-x}$ for $x = 0.25$, 0.5, and 0.75, and a 64 atom supercell for 0.875 [50]. Inserting hydrogen atoms in tetrahedral interstitial positions then gives
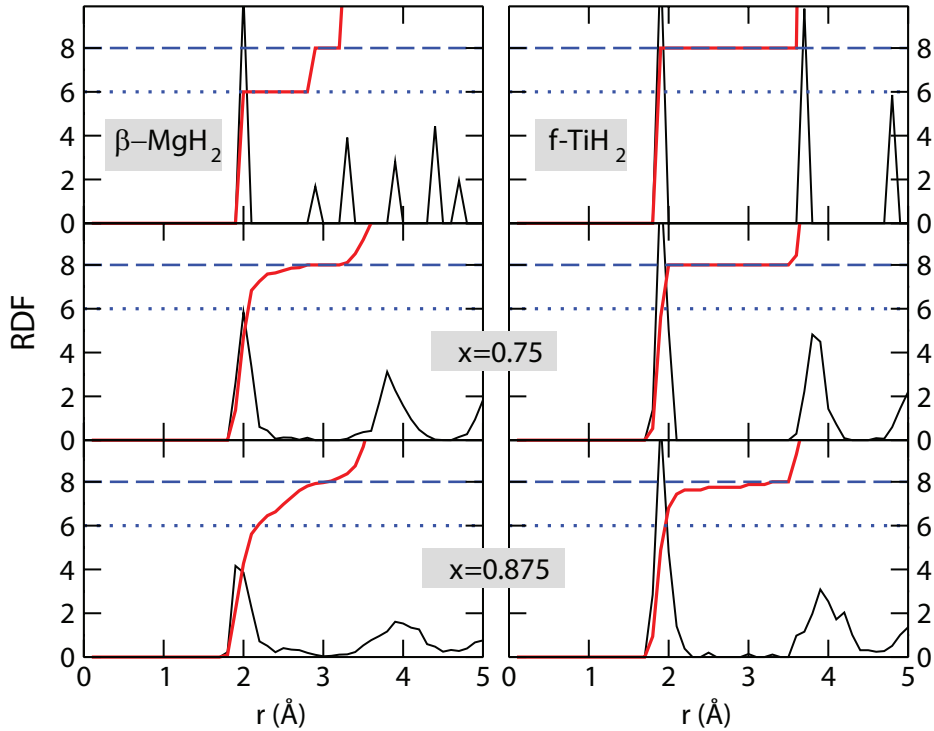
Figure 4.5: Radial distribution functions (RDFs) for Mg−H (left column) and Ti−H (right column) pairs in $Mg_x Ti_{(1-x)} H_2$, $x = 0.75$, 0.875 fluorite-type SQSs, compared to the RDFs of β-MgH_2 and f-TiH_2. The red lines indicate the integrated RDF. Horizontal dotted and dashed lines indicate the H coordination numbers of Mg and Ti in the simple dihydrides, respectively.

supercells with a total number of atoms of 96 and 192, respectively. Optimizing the structure leads to some displacements in the positions of the metal atoms, but they remain close to fcc. There is a larger spread in the positions of the H atoms, which increases with increasing x. Representative examples of SQSs are given in figure 4.4. Whereas in the ordered structures of table 4.4 the nearest neighbour Ti−Ti distance increases with increasing Mg content x, in the SQSs one can always find at least one Ti−Ti pair at a distance comparable to that in f-TiH_2, for the compositions studied.

The optimized volumes of the SQSs are shown in figure 4.3. For $x \leq 0.75$ these volumes are within 1.5% of those of the ordered structures. Remarkably, the SQS volume of $Mg_{0.875} Ti_{0.125} H_2$ is 4.9% larger than that of the ordered structure of table 4.4. This is indicative of a structural change at this composition, which can be

clarified by calculating the radial distribution functions (RDFs) of the SQSs. The RDFs of $Mg_xTi_{(1-x)}H_2$ for $x = 0.75, 0.875$ are plotted in figure 4.5. Shown are the RDFs of Ti−H and Mg−H distances and the corresponding RDFs in the cubic β-MgH_2 and f-TiH_2 compounds. Integrating the RDF gives the number of hydrogen atoms surrounding each metal atom. The number in the first shell then corresponds to the coordination number of the metal atom.

In f-TiH_2 each Ti atom is coordinated by eight H atoms at a distance of approximately 1.9 Å, whereas in the Mg atoms in β-MgH_2 are coordinated by six H atoms at 2.0 Å, and by an additional two H atoms at 2.9 Å. The RDFs of the SQSs show that in $Mg_xTi_{(1-x)}H_2$ each Ti is coordinated as in f-TiH_2, irrespective of the composition x. For $x = 0.75$ each Mg atom is also coordinated by eight atoms at a similar distance, as in a fluorite structure. However, for $x = 0.875$ the RDF for Mg−H starts to resembles that of β-MgH_2, i.e. a peak representing six H atoms at ~ 2.0 Å, and a shoulder representing two H atoms at ~ 2.9 Å. Apparently a large Mg content is required before such a structure can develop, which is accompanied by a volume expansion with respect to an ideal fluorite structure. In order not to complicate the terminology we call all such structures fluorite-type in the following.

Since we will compare the stability of these fluorite-type structures to rutile-type structures $Mg_xTi_{(1-x)}H_2$, we also make models of the latter using the α-MgH_2 structure as a starting point. To construct simple, ordered structures, we replace a fraction x of the Mg atoms by TM atoms and use the smallest supercell of the rutile structure where this leads to an integer number of atoms. In case of multiple possible cells, the results given below refer to the cell that leads to the lowest energy. Rutile SQSs of $Mg_xTi_{(1-x)}$ for $x = 0.25$-0.875 are constructed using standard algorithms [50]. As it turns out that rutile structures are relatively unstable over a large composition range, we refrain from giving their structural details here.

4.5.2   Stability

Experimentally it is concluded that Mg and Ti do not form a thermodynamically stable bulk alloy. Indeed we find that its costs energy to make alloys from the bulk metals Mg and Ti. For instance, the energy costs of making $Mg_xTi_{(1-x)}$ fcc SQSs from bulk hcp Mg and Ti are 0.16 and 0.11 eV/atom for $x = 0.5$ and 0.75, respectively, and for $Mg_xTi_{(1-x)}$ in the simple, ordered CuAu and Cu_3Au structures the energy costs are 0.22 and 0.15 eV/atom, respectively. Calculations on hcp $Mg_xTi_{(1-x)}$ decrease these numbers by ~ 0.04 eV, which implies that the hcp alloy is more stable than the fcc alloy, but it is still unstable. Moreover, simple estimates of the configurational entropy show that the alloys cannot be stabilized at a reasonable
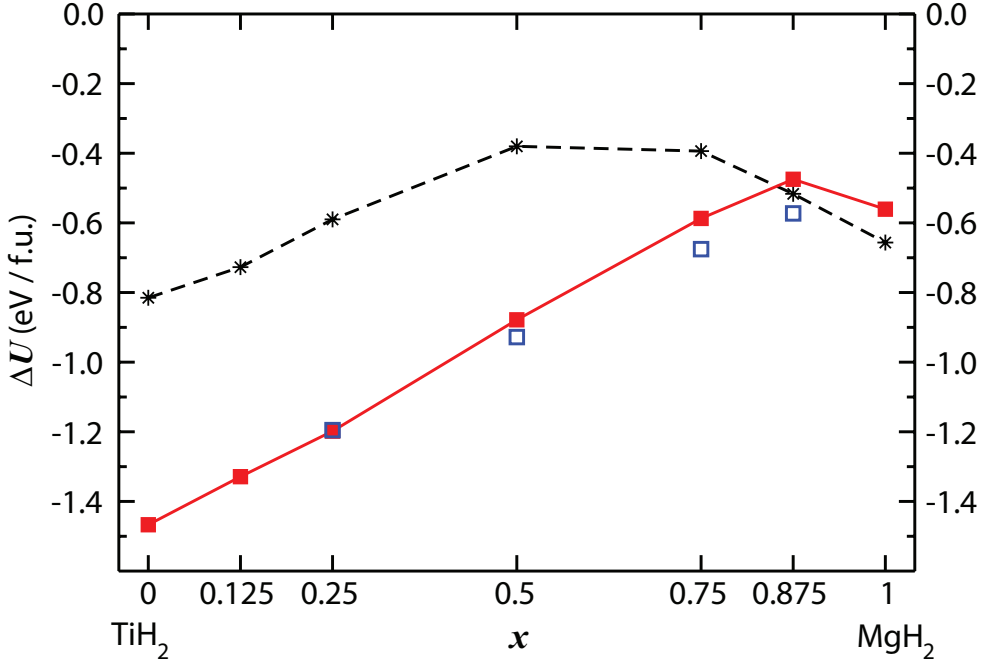
Figure 4.6: Formation energies of $\mathrm{Mg}_x\mathrm{Ti}_{(1-x)}\mathrm{H}_2$ as function of composition x for ordered fluorite-type (filled red squares) and rutile-type (black stars) structures. The lines are added to guide the eye. The open blue squares indicate the formation energies of fluorite-type SQSs.

temperature by entropy. Metastable structures can still be relevant, though, as thin film deposition of $\mathrm{Mg}_x\mathrm{Ti}_{(1-x)}$ yields a hcp structure that survives a large number of (de)hydrogenation cycles.

The formation energy of $\mathrm{Mg}_x\mathrm{Ti}_{(1-x)}\mathrm{H}_2$ according to (4.1) is given in figure 4.6 for the fluorite and rutile structures. The numbers are given without ZPE corrections, which we will discuss later. Clearly all numbers are negative, which implies that the compounds are stable with respect to decomposition into the elements. In addition, over most of the composition range the fluorite structure is more stable than the rutile structure. For x larger than a critical composition x_c the rutile structure becomes lower in energy. If we use the energies calculated for the simple ordered structures as a starting point and linearly interpolate between the compositions, we find $x_c \approx 0.83$. The fact that x_c has a high value makes sense, since the energy difference between the α-MgH_2 (rutile) and β-MgH_2 ("fluorite") phases is only 0.10 eV/f.u., whereas between f-TiH_2 (fluorite) and r-TiH_2 (rutile) it is 0.65 eV/f.u..

Therefore, it requires a high Mg content to force the structure into rutile. Indeed, experimental results suggest that the cross-over from fluorite to rutile structures in $Mg_xTi_{(1-x)}H_2$ occurs for x somewhere in the range 0.8-0.9 [15, 17].

Note that for all compositions the structures are metastable with respect to decomposition into TiH_2 and MgH_2, as is evident from figure 4.6. Evidently, the decomposition is kinetically hindered as it does not occur experimentally. Upon dehydrogenation the cubic $Mg_xTi_{(1-x)}H_2$ converts into hcp $Mg_xTi_{(1-x)}$. Although the latter is metastable with respect to Ti and Mg, its decomposition is also kinetically hindered, as thin films can be (de)hydrogenated reversibly. The apparent stability of these compounds is quite remarkable.

The formation energies of the fluorite SQSs are also given in figure 4.6. Within the constraints of the SQS approach, some variation in the relative ordering of Ti and Mg atoms is still possible at each composition x. We estimate that this variation gives a spread in the energies of ~ 0.1 eV/f.u.. From figure 4.6 one also observes that the most stable SQSs are slightly more stable than the ordered structures, by up to ~ 0.1 eV/f.u. for $x = 0.875$. We have also constructed rutile SQSs of $Mg_xTi_{(1-x)}$ for $x = 0.25$-0.875. However, upon optimization these structures turn out to be unstable and spontaneously convert into a fluorite-type structure (i.e. using the conjugate gradient algorithm). This would suggest that a fluorite-type structure is stable at least up to a composition $x = 0.875$. As the energies of the two types of structures are quite similar over a range of compositions close to the critical composition x_c, the exact value of x_c is difficult to determine. Note that here we only consider simple ordered and SQSs models of rutile and flourite-type lattices. Of course, it cannot be excluded that different structural models describe the true ground state. However, our structures are judicially chosen so that our studies are relevant to understand the experiments; indeed we obtain a good agreement with experimental studies.

The ZPE corrections destabilize the simple hydrides α-MgH_2 and α-TiH_2, see table 4.2, and one expects this also to be the case in $Mg_xTi_{(1-x)}H_2$. The size of the ZPE correction in the simple hydrides indicates that it decreases with increasing x from 0.19 eV/f.u. at $x = 0$ to 0.10 eV/f.u. at $x = 1$. We suggest that this decrease is approximately linear in x. An explicit calculation on the SQS of the $x = 0.75$ composition gives a ZPE correction of 0.12 eV/f.u., in agreement with this suggestion.

We now consider to what extend $Mg_xTi_{(1-x)}H_2$ is suitable as a hydrogen storage material. Experimentally it has been observed that the dehydrogenation kinetics becomes markedly slower if $x \gtrsim x_0 = 0.8$. The results of figure 4.6 strongly suggest that $x_0 = x_c$, i.e. the composition at which the phase transition between fluorite

and rutile structures takes place. Lightweight materials require a high content of magnesium, but to have a stable fluorite structure it should not exceed the critical composition x_c. We focus upon the composition $Mg_{0.75}Ti_{0.25}H_2$, which should have the fluorite structure. It has gravimetric and volumetric hydrogen densities of 6.2 wt% and 0.135 kg/L, respectively. Its calculated formation energy is -0.59 eV/f.u. (without ZPE), which means that this compound is slightly less stable than α-MgH_2 with respect to decomposition into the elements. A decreased stability of the hydride should ease the dehydrogenation reaction. However, in order that the process is reversible, it is not advantageous if the alloy $Mg_xTi_{(1-x)}$ dissociates upon dehydrogenation. If we calculate the hydrogenation energy according to the reaction

$$Mg_xTi_{(1-x)} + H_2(g) \rightarrow Mg_xTi_{(1-x)}H_2, \tag{4.5}$$
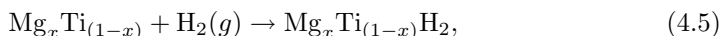
we find -0.76 eV/f.u. for $x = 0.75$. This number is in good agreement with the experimental value of -0.81 eV/f.u. of [73], obtained if the thin film correction suggested there is included. This hydrogenation enthalpy is somewhat lower than that of pure Mg, showing that alloying Mg with Ti does not improve the thermodynamics as compared to pure Mg. On the other hand, it is also not much worse, and the kinetics of (de)hydrogenation of $Mg_{0.75}Ti_{0.25}H_2$ is markedly better than that of pure Mg.

4.5.3 Electronic structure and optical properties

The calculated electronic density of states (DOS) of $Mg_xTi_{(1-x)}H_2$ in the simple ordered structures is shown in figure 4.7 for fluorite- and rutile-type structures. Qualitatively these DOSs can be interpreted as linear combinations of DOSs of the simple hydrides, see figure 4.2. In the DOSs of the rutile structure one can still distinguish the band gap that originates from MgH_2. The states just above the gap originate from Ti, as discussed in Sec. 4.4. In particular the DOS of rutile-$Mg_{0.875}Ti_{0.125}H_2$ can be interpreted as Ti-doped α-MgH_2. Enlarging the Ti content then increasingly fills the gap with Ti-derived states and for rutile-$Mg_{0.25}Ti_{0.75}H_2$, the DOS is dominated by a Ti-derived peak at the Fermi level.

A similar qualitative interpretation of the DOSs also holds for the $Mg_xTi_{(1-x)}H_2$ fluorite structures. It is somewhat less clear because the band gap in (fluorite-type) β-MgH_2 is smaller than that of (rutile) α-MgH_2. Still the DOS of $Mg_{0.875}Ti_{0.125}H_2$ can clearly be interpreted as Ti-doped β-MgH_2, where Ti-derived states appear in the gap. Upon increasing the Ti content, the DOS more and more resembles that of f-TiH_2 and the gap is completely filled. The latter has implications for the optical properties, as we will discuss below.
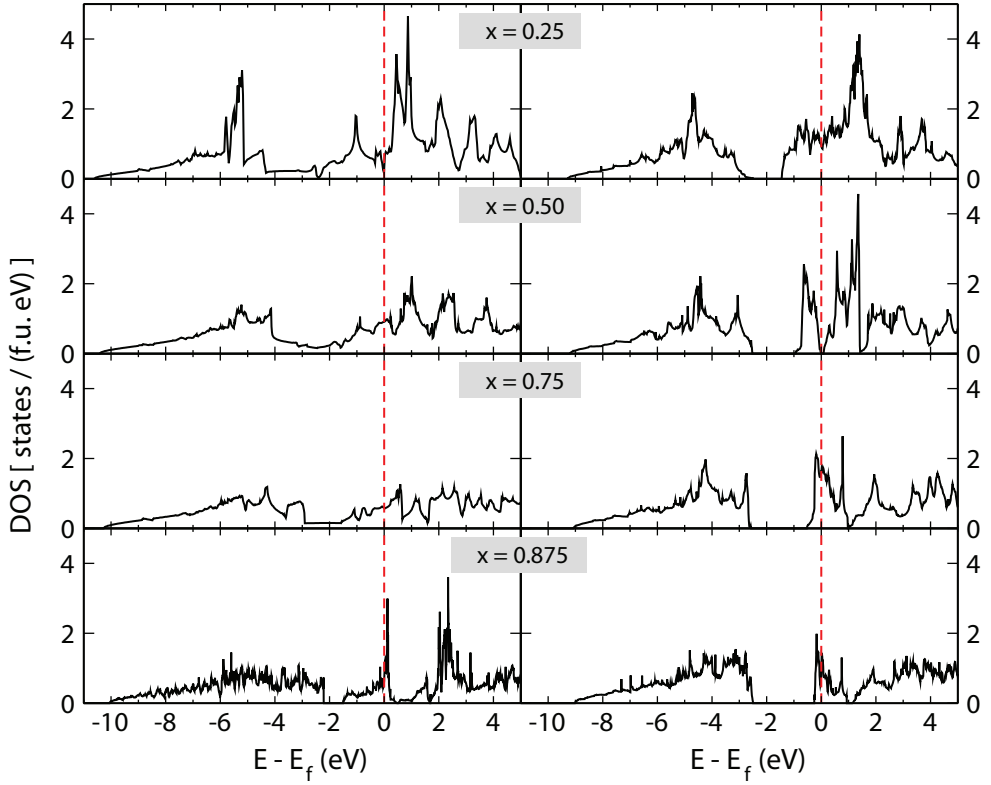
Figure 4.7: Electronic density of states (DOS) per formula unit for the fluorite (left column) and rutile (right column) $Mg_x Ti_{(1-x)} H_2$ structures.

In order to be able to identify the character of the electronic states, the atom projected DOS of the simple structures is shown in fig. 4.8 for fluorite-type $Mg_x Ti_{(1-x)} H_2$, $x = 0.75, 0.875$, which are the most relevant structures and compositions for studying the optical properties [15]. It is obvious that the peaks at the Fermi level are dominated by states of Ti 3d character, as in f-TiH_2, see figure 4.2. For $Mg_{0.875} Ti_{0.125} H_2$ these peaks are narrow, reflecting the large distance of 6.62 Å between neighbouring Ti atoms. One observes the e_g-t_{2g} splitting that is typical of d states in a cubic crystal field. In this case the latter originates from the cubic coordination of each Ti atom by H atoms. Local magnetic moments of 1.5 μ_B develop on the Ti atoms and we predict an anti-ferromagnetic ordering of these moments at low temperature. The estimated Néel temperature is only 40K, however, demonstrating that the moments are atomic like. If we increase the Ti content, the states on neighbouring Ti atoms interact more strongly. For $Mg_{0.75} Ti_{0.25} H_2$ the nearest neighbour distance between Ti atoms is 4.62 Å. The Ti d derived peaks are much wider, and the local magnetic

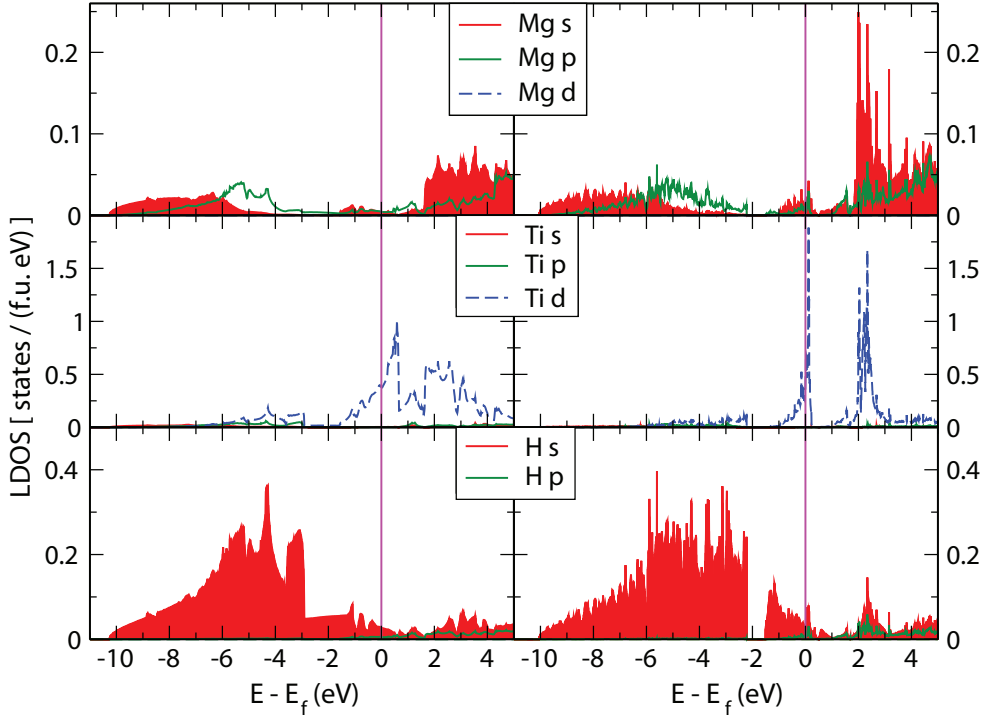**Figure 4.8:** Local density of states (LDOS) for fluorite-$Mg_xTi_{(1-x)}H_2$, $x = 0.75$ (left column) and $x = 0.875$ (right column). The origin of the energy scale is set at the Fermi level. Atomic s, p and d contributions are shown in red, green and blue, respectively. The regions under the s curves are shaded and the d curves are dashed.

moments disappear.

The states in the PDOS at low energy are dominantly H 1s derived states, as expected. Interestingly, the states around the Fermi level also have a H contribution. These contributions are spread out over an energy range that is much wider in $Mg_xTi_{(1-x)}H_2$ than in the simple hydrides MgH_2 and TiH_2, see figure 4.2. The spread occurs in H derived bands of s character, as well as in the those of p character. Since transitions between such H derived bands give a large contribution to the optical response of a hydride [53], one might expect the response to be spread over a large energy range.

We calculate the optical response functions of $Mg_xTi_{(1-x)}H_2$ as described in Sec. 4.3. The refractive index $n(\omega)$ and the extinction coefficient $\kappa(\omega)$ are shown in figure 4.9 for the compositions $x = 0.5$, 0.75, and 0.875. Most relevant for a com-
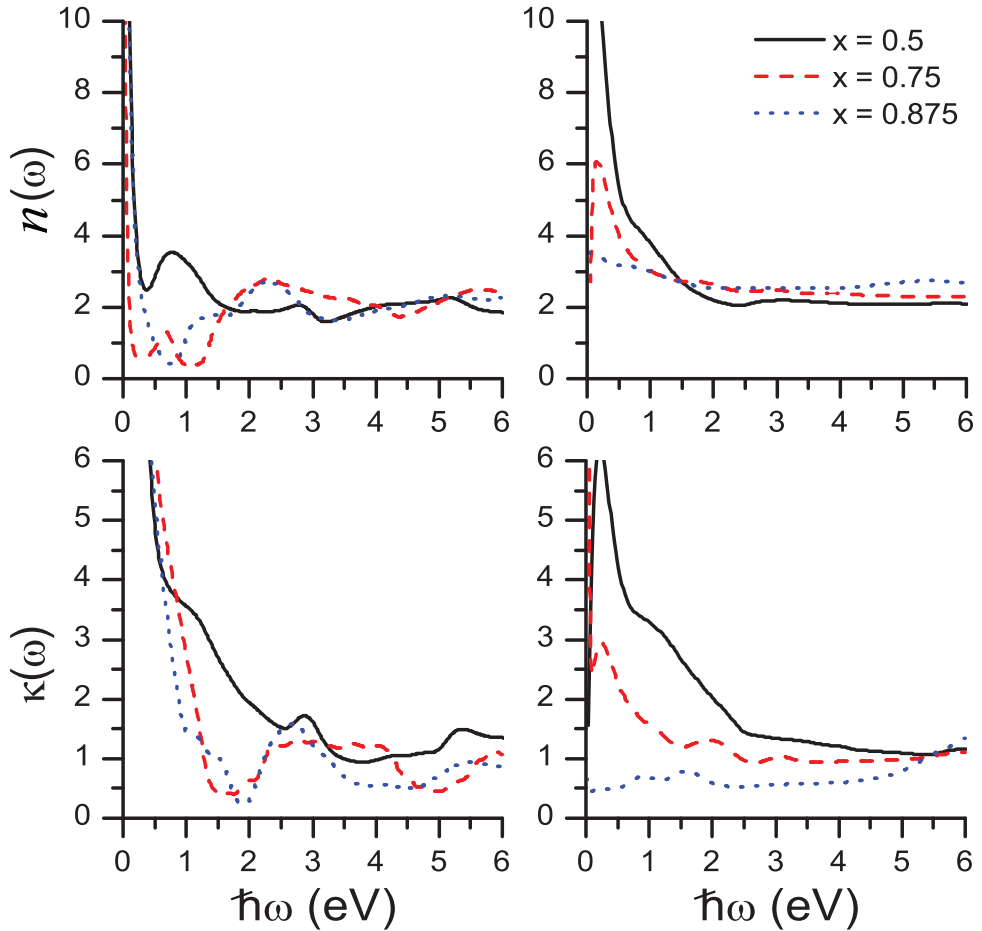
Figure 4.9: Index of refraction (top) $n(\omega)$ and extinction coefficient $\kappa(\omega)$ (bottom) of $Mg_xTi_{(1-x)}H_2$ as function of frequency ω. The black (solid), red (dashed), and blue (dotted) lines are for the compositions $x = 0.5, 0.75, 0.875$, respectively. The left and right columns are for the ordered structures and the SQSs, respectively.

parison to the optical experiments on thin films are the data for the SQSs. Comparing our data on the SQSs and the ordered structures, we observe that one main effect of disorder in the positions of the metal atoms, as modelled by a SQS, is smoothing the spectrum.

In addition, disorder strongly affects the lower end of the spectrum, i.e. $\omega = 0$-1.5 eV, in particular for the Mg-rich compositions $x = 0.75, 0.875$. The extinction coefficient $\kappa(\omega)$ of the SQSs in this frequency range is smaller than that of the ordered

structures and much closer to its value at high frequency. The large $\kappa(\omega < 1 \text{ eV})$ in the ordered structures is typical for the electron plasma response of metals, which matches the DOSs shown in figure 4.7. As the metallic properties of $Mg_xTi_{(1-x)}H_2$ originate from the Ti atoms only, introducing disorder in the Ti positions can destroy the electron plasma, suppressing the large $\kappa(\omega < 1 \text{ eV})$ [26]. As can be observed in figure 4.9, compositions with a low Ti content are particularly sensitive to disorder, as the coupling between Ti atoms is relatively small.

Also the structure in the refractive index of the ordered structures at low frequency is suppressed in the SQSs and the refractive index at $\omega > 1$ eV becomes close to constant. Assuming that one may use bulk optical functions to model the optical properties of $Mg_xTi_{(1-x)}H_2$, the reflectance (at normal incidence) of a surface is given by the usual Fresnel expression $R = ((n-1)^2 + \kappa^2)/((n+1)^2 + \kappa^2)$. For a metal usually $\kappa \gg n$, giving rise to a large reflectance. In this case both κ and n are rather moderate for frequencies in the visible region. Using the data shown in figure 4.9 one obtains an almost constant low reflectance $R \approx 0.2$ over the whole visible region. Since the extinction coefficient is also almost constant in the visible region and it has a quite considerable value, the material $Mg_xTi_{(1-x)}H_2$ has a dark, colourless, i.e. black appearance.

Using the extinction coefficient of the $Mg_xTi_{(1-x)}H_2$ SQSs shown in figure 4.9 to calculate the absorption $\alpha(\omega) = 2\kappa(\omega)\omega/c$, we obtain a good qualitative agreement with experimental data [15]. The quantitative difference between the calculated and experimental absorption is ~ 30 %, which reflects both the approximations made in the calculations, and in the extraction of the experimental values.

4.6   Summary and Conclusions

MgH_2 has a high hydrogen storage capacity, but it suffers from poor (de) hydrogenation kinetics and a high thermodynamic stability, which make it unsuitable as a hydrogen storage material. Adding Ti to Mg gives an alloy hydride $Mg_xTi_{(1-x)}H_2$ with much faster (de)hydrogenation kinetics for $x \lesssim 0.8$. In this paper we have studied the structure and stability of $Mg_xTi_{(1-x)}H_2$, $x = 0\text{-}1$, by first-principles calculations at the level of density functional theory.

As the most stable structures (at ambient conditions) of MgH_2 and TiH_2 are rutile and fluorite, respectively, we model such structures for the alloy hydride $Mg_xTi_{(1-x)}H_2$. A series of simple, ordered fluorite structures is constructed analogous to the high pressure Mg_7TiH_{16} phase, and rutile structures are modelled in MgH_2 supercells. All cell parameters and atomic positions are optimized and care is

taken to converge the total energies with respect to computational parameters such as the basis set size and the k-point sampling grid. Upon optimization, all structures stay quite close to either fluorite or rutile. To model disorder in the positions of the metal atoms, we construct a series of SQSs of $Mg_xTi_{(1-x)}H_2$ starting from fluorite and rutile structures. Upon optimization the fluorite structures are stable, but in compositions with a high Mg content, such as $Mg_{0.875}Ti_{0.125}H_2$, the structure around the Mg atoms starts to resemble that of the high pressure phase β-MgH$_2$. The SQS rutile structures of $Mg_xTi_{(1-x)}H_2$ are unstable for $x \leq 0.875$. From the formation energies of the ordered, as well as the disordered structures, we give evidence for a fluorite to rutile phase transition at a critical composition $x_c = 0.8$-0.9. This correlates with the experimentally observed sharp decrease in (de)hydrogenation rates around this composition.

Thin films of $Mg_xTi_{(1-x)}$ show a remarkable optical transition from reflecting to absorbing upon hydrogenation, which is reversible upon dehydrogenation. We calculate the optical response of $Mg_xTi_{(1-x)}H_2$, $x = 0.5$-0.875, in the ordered and disordered structures and show that the black absorbing state is an intrinsic property of this material. $Mg_xTi_{(1-x)}H_2$ has a peak at the Fermi level for all compositions x, which is composed of Ti d states. However, the resulting metallic plasma only plays a minor role in the optical response in the visible range for compositions with a high Mg content, as interband transitions interfere to decrease the extinction coefficient κ. Moreover, this effect is enhanced by disorder in the positions of the Ti atoms, which easily destroys the metallic plasma and suppresses the optical reflection even more. The contributions of the H atoms to the bands are spread out over a large energy range as a result of the diverse coordination by Ti and Mg atoms in $Mg_xTi_{(1-x)}H_2$. Interband transitions then result in an almost constant optical absorption over a large energy range, causing the black appearance of these compounds.

Acknowledgments

Bibliography

[1] See the special issue *Toward a Hydrogen Economy*, by R. Coontz and B. Hanson, Science **305**, 957 (2004).

[2] A. Züttel, Mater. Today **6**, 24 (2003).

[3] L. Schlapbach and A. Züttel, Nature **414**, 353 (2001).

[4] A. Züttel, Naturwiss. Unterr. Chem. **91**, 157 (2004).

[5] J. Huot, G. Liang, and R. Schulz, Appl. Phys. A: Mater. Sci. Process. **72**, 187 (2001).

[6] L. Schlapbach, editor, *Hydrogen in Intermetallic Compounds II* (Springer, Berlin, 1992).

[7] F. Manchester and D. Khatamian, Mater. Sci. Forum **31**, 261 (1988).

[8] A. Zaluska, L. Zaluski, and J. O. Ström-Olsen, J. Alloys Compd. **288**, 217 (1999).

[9] A. Zaluska, L. Zaluski, and J. O. Ström-Olsen, Appl. Phys. A: Mater. Sci. Process. **72**, 157 (2001).

[10] R. A. H. Niessen and P. H. L. Notten, Electrochem. Solid-State Lett. **8**, A534 (2005).

[11] R. A. H. Niessen and P. H. L. Notten, J. Alloys Compd. **404**, 457 (2005).

[12] P. Vermeulen, R. A. H. Niessen, and P. H. L. Notten, Electrochem. Commun. **8**, 27 (2006).

[13] G. Liang, J. Huot, S. Boily, A. V. Neste, and R. Schulz, J. Alloys Compd. **292**, 247 (1999).

[14] M. Latroche, W. P. Kalisvaart, and P. H. L. Notten, J. Solid State Chem. **179**, 3024 (2006).

[15] D. Borsa *et al.*, Phys. Rev. B **75**, 205408 (2007).

[16] P. C. M. M. Magusin, W. P. Kalisvaart, P. H. L. Notten, and R. A. van Santen, Chem. Phys. Lett. **456**, 55 (2008).

[17] P. Vermeulen *et al.*, J. Mater. Chem. **18**, 3680 (2008).

[18] P. Vermeulen *et al.*, Electrochem. Solid-State Lett. **9**, A520 (2006).

[19] D. M. Borsa *et al.*, Appl. Phys. Lett. **88**, 241910 (2006).

[20] M. Slaman *et al.*, Sens. Actuators: B **123**, 538 (2007).

[21] A. Baldi *et al.*, Int. J. Hydrogen Energy **33**, 3188 (2008).

[22] D. Kyoi *et al.*, J. Alloys Compd. **372**, 213 (2004).

[23] E. Rönnebro, D. Kyoi, A. Kitano, Y. Kitano, and T. Sakai, J. Alloys Compd. **404**, 68 (2005).

[24] S. Er, D. Tiwari, G. A. de Wijs, and G. Brocks, Phys. Rev. B **79**, 024105 (2009).

[25] B. R. Pauw *et al.*, Acta Mater. **56**, 2948 (2008).

[26] M. J. van Setten, S. Er, G. Brocks, R. A. de Groot, and G. A. de Wijs, Phys. Rev. B **79**, 125117 (2009).

[27] T. J. Richardson *et al.*, Appl. Phys. Lett. **78**, 3047 (2001).

[28] W. Lohstroh *et al.*, Phys. Rev. Lett. **93**, 197404 (2004).

[29] P. E. Blöchl, Phys. Rev. B **50**, 17953 (1994).

[30] G. Kresse and D. Joubert, Phys. Rev. B **59**, 1758 (1999).

[31] G. Kresse and J. Hafner, Phys. Rev. B **47**, 558 (1993).

[32] G. Kresse and J. Furthmüller, Phys. Rev. B **54**, 11169 (1996).

[33] G. Kresse and J. Furthmüller, Comput. Mater. Sci. **6**, 15 (1996).

[34] J. P. Perdew and Y. Wang, Phys. Rev. B **45**, 13244 (1992).

[35] A. D. Becke, J. Chem. Phys. **98**, 5648 (1993).

[36] J. Heyd, G. E. Scuseria, and M. Ernzerhof, J. Chem. Phys. **118**, 8207 (2003).

[37] J. Paier *et al.*, J. Chem. Phys. **124**, 154709 (2006).

[38] J. Paier *et al.*, J. Chem. Phys. **125**, 249901 (2006).

[39] J. Paier, M. Marsman, and G. Kresse, J. Chem. Phys. **127**, 024103 (2007).

[40] S. Froyen, Phys. Rev. B **39**, 3168 (1989).

[41] M. C. Payne, M. P. Teter, D. C. Allan, T. A. Arias, and J. D. Joannopoulos, Rev. Mod. Phys. **64**, 1045 (1992).

[42] M. Methfessel and A. T. Paxton, Phys. Rev. B **40**, 3616 (1989).

[43] P. E. Blöchl, O. Jepsen, and O. K. Andersen, Phys. Rev. B **49**, 16223 (1994).

[44] K. P. Huber and G. Herzberg, *Molecular Spectra and Molecular Structure* (Van Nostrand Reinhold, New York, 1979).

[45] H. Hemmes, A. Driessen, and R. Griessen, J. Phys. C: Solid State Phys. **19**, 3571 (1986).

[46] M. J. van Setten, G. A. de Wijs, M. Fichtner, and G. Brocks, Mater. Chem. **20**, 4952 (2008).

[47] M. J. van Setten, G. A. de Wijs, and G. Brocks, Phys. Rev. B **77**, 165115 (2008).

[48] G. Kresse, J. Furthmüller, and J. Hafner, Europhys. Lett. **32**, 729 (1995).

[49] A. Zunger, S. H. Wei, L. G. Ferreira, and J. E. Bernard, Phys. Rev. Lett. **65**, 353 (1990).

[50] A. V. Ruban, S. I. Simak, S. Shallcross, and H. L. Skriver, Phys. Rev. B **67**, 214302 (2003).

[51] C. Wolverton, V. Ozolins, and A. Zunger, J. Phys.: Condens. Matter **12**, 2740 (1999).

[52] M. Gajdoš, K. Hummer, G. Kresse, J. Furthmüller, and F. Bechstedt, Phys. Rev. B **73**, 045112 (2006).

[53] M. J. van Setten, V. A. Popa, G. A. de Wijs, and G. Brocks, Phys. Rev. B **75**, 35204 (2007).

[54] J. N. Huiberts *et al.*, Nature **380**, 231 (1996).

[55] P. van Gelderen, P. A. Bobbert, P. J. Kelly, and G. Brocks, Phys. Rev. Lett. **85**, 2989 (2000).

[56] P. van Gelderen, P. A. Bobbert, P. J. Kelly, G. Brocks, and R. Tolboom, Phys. Rev. B **66**, 075104 (2002).

[57] M. J. van Setten, G. A. de Wijs, V. A. Popa, and G. Brocks, Phys. Rev. B **72**, 073107 (2005).

[58] M. J. van Setten, G. A. de Wijs, and G. Brocks, Phys. Rev. B **76**, 075125 (2007).

[59] J. Harl, G. Kresse, L. D. Sun, M. Hohage, and P. Zeppenfeld, Phys. Rev. B **76**, 35436 (2007).

[60] K. Momma and F. Izumi, IUCr Newslett. **7**, 106 (2006).

[61] P. Villars, L. D. Calvert, and W. B. Pearson, *Pearson's Handbook of Crystallographic Data for Intermetallic Phases* (ASM International, Materials Park, OH, USA, 1991).

[62] M. Bortz, B. Bertheville, G. Bottger, and K. Yvon, J. Alloys Compd. **287**, L4 (1999).

[63] J. P. Bastide, B. Bonnetot, J. M. Letoffe, and P. Claudy, Mater. Res. Bull. **15**, 1215 (1980).

[64] P. Vajeeston, P. Ravindran, A. Kjekshus, and H. Fjellvåg, Phys. Rev. Lett. **89**, 175506 (2002).

[65] F. D. Manchester, *Phase Diagrams of Binary Hydrogen Alloys* (ASM International, Materials Park, OH, USA, 2000).

[66] B. Bogdanovic *et al.*, J. Alloys Compd. **282**, 84 (1999).

[67] D. R. Lide, *CRC Handbook of Chemistry and Physics. 83r̂d edition* (CRC Press, Boca Raton, 2002).

[68] R. Griessen and T. Riesteter, *Topics in Applied Physics–Hydrogen in Intermetallic Compounds* (Springer, Berlin, 1988).

[69] J. Isidorsson, I. Giebels, H. Arwin, and R. Griessen, Phys. Rev. B **68**, 115112 (2003).

[70] M. R. Hartman, J. J. Rush, T. J. Udovic, R. C. Bowman, and S. J. H. Jr., J. Solid State Chem. **180**, 1298 (2007).

[71] J. Hafner, J. Phys. F: Met. Phys. **15**, L43 (1985).

[72] G. Liang and R. Schulz, J. Mater. Sci. **38**, 1179 (2003).

[73] R. Gremaud *et al.*, Adv. Mater. **19**, 2813 (2007).

Chapter 5

A computational study of hydrogen storage in Mg-Ti-X (X =Al, Si)

5.1 Abstract

Mixing Mg with Ti leads to an alloy with markedly improved hydrogenation kinetics as compared to pure Mg. However, the resulting hydrides are too stable for applications as hydrogen storage materials at moderate temperatures and pressures. Moreover Mg-Ti alloys are unstable with respect to decomposition into the elements. In this paper we examine by means of first-principles density functional theory calculations whether adding Al or Si to Mg-Ti can improve its thermodynamic properties. Indeed we find that Mg-Ti-X (X = Al or Si) alloys are more stable than Mg-Ti alloys, whereas their hydrides are less stable. Controlling the structure of Mg-Ti-X alloys brings the hydrogenation energy in a range that is suitable for their use as hydrogen storage materials.

5.2 Introduction

Future use of hydrogen as an energy carrier depends on finding safe, compact and cost effective methods for storing hydrogen[1]. Solid state storage in the form of metal hydrides is promising since it offers both a safe way of handling hydro-

gen, as well as high volumetric hydrogen densities [2, 3]. Attaining high gravimetric hydrogen densities using solid state storage methods is limited to compounds comprised of lightweight elements. Magnesium, an inexpensive and abundant metal, can store up to 7.65 wt.% hydrogen [4]. The application of MgH_2 as a hydrogen storage material is however obstructed by its high thermodynamic stability and very low (de)hydrogenation rates, both of which lead to excessively high desorption temperatures $T \gtrsim 300°$ [5]. A significant amount of research has been devoted to reduce the stability of MgH_2 or to enhance its (de)hydrogenation kinetics. Experiments on thin films have shown that alloying magnesium with early transition metal (TM) elements can markedly improve the hydrogen kinetics [6–9]. The best results have been obtained with the TMs Sc and Ti and alloy compositions $Mg_{(1-x)}TM_x$ with $x \approx 0.2$.

The improved kinetics have been linked to the existence of a cubic, fluorite-type $Mg_{(1-x)}TM_xH_2$ phase, whereas the tetragonal rutile phase of MgH_2 would hamper the (de)hydrogenation kinetics. From first principles calculations we have shown that a fluorite-type phase of $Mg_{(1-x)}TM_xH_2$ is stable with respect to a rutile-type phase for TM = Sc, Ti, V and Cr, and $x \gtrsim 0.2$ [10]. However, the dehydrogenation enthalpy of these compounds is either larger, or at least not significantly smaller, than that of MgH_2, implicating that the thermodynamic properties are not improved (sufficiently). Moreover, the stability of the $Mg_{(1-x)}TM_x$ alloys decreases along the series Sc, Ti, V, Cr. In fact, only $Mg_{(1-x)}Sc_x$ is thermodynamically stable with respect to decomposition into the elemental metals (Mg and Sc). Scandium is a rare element, however, which prevents its large scale use in a hydrogen storage material. $Mg_{(1-x)}V_x$ and $Mg_{(1-x)}Cr_x$ are thermodynamically quite unstable, which hampers their use in a reversible system, which needs to undergo repeated hydrogen (un)loading cycles.

Ti is an abundant element and thus suitable for large scale applications. The binary phase diagram of Mg and Ti indicates that a stable alloy between these two elements cannot be formed. Studies of kinetically stabilized bulk Mg-Ti samples have been inconclusive [11–13], but Mg-Ti alloys are readily formed in thin films, which are stable under repeated (de)hydrogenation cycles [6, 8, 9, 11, 14–16]. The high stability of Mg-Ti hydride remains a problem, however. The calculated dehydrogenation enthalpy of $Mg_{0.75}Ti_{0.25}H_2$ is 0.76 eV/H_2, which is close to the values reported for MgH_2. Recently, Vermeulen *et al.* [17] have reported that incorporating Al or Si into Mg-Ti thin films decreases the dehydrogenation energy. The hydrogen storage capacity is a maximum 6 wt. % for a composition consisting of 70 at.% Mg, 20 at.% Ti and 10 at.% Al. Similarly, 4.53 wt. % hydrogen is stored in a Mg-Ti-Si alloy of a

similar composition.

In this paper we calculate the stability of Mg-Ti-X (X = Al or Si) alloys and their hydrides for several possible compositions by means of first-principles density functional theory (DFT) calculations. Simultaneous deposition of the metals very likely results in random alloy thin films, whereas by controlled subsequent deposition one might form multilayer structures. We study the energetics of examples of both disordered structures and multilayers.

5.3 Computational methods

DFT calculations are performed at the level of the generalized gradient approximation (GGA) using the PW91 functional [18]. We employ the projector augmented wave (PAW) technique and a plane wave basis set [19, 20], as implemented in the Vienna *Ab initio* Simulation Package (VASP)[21–23]. Standard frozen core PAW potentials are used, where the H $1s$, Mg $3s$, Al $3s3p$, Si $3s3p$ and Ti $3p4s4d$ shells are treated as valence shells. As Ti has a partially filled $3d$ shell, the possibility of spin-polarization is examined. The plane wave kinetic energy cutoff is set at 518 eV. The Brillouin zone is integrated using a regular **k**-point mesh with a spacing of 0.02 Å^{-1} and the Methfessel-Paxton scheme with a smearing parameter of 0.1 eV [24]. The volumes and shapes of the unit cells are optimized, as well as the positions of the atoms. Total energies of the optimized structures are finally calculated using the tetrahedron method [25]. Details on the optimization procedure can be found in Ref. [26].

5.4 Mg-Ti-Al,Si metals

The aim of adding Al or Si is to stabilize the metal Mg-Ti, which otherwise is thermodynamically unstable, as discussed above. Al and Si are chosen because both Mg and Ti form binary alloys with Al and Si. We first look at the energetics of these binary alloys, and then study the possibilities of forming ternary alloys, either as disordered structures, or as multilayers.

5.4.1 Binary alloys

The elements Mg and Ti crystallize in the hcp structure, whereas Al and Si adopt the cubic fcc and diamond structures, respectively. The binary phase diagram of Mg and Al indicates that alloys between these elements can be formed at various

Table 5.1: Optimized lattice parameters (a and c/a) and formation energies with respect to the elemental solids for MX (M = Mg, Ti; X = Al, Si) in the $L1_0$ structure.

Compound	a (Å)	c/a	E_f (eV/atom)
MgAl	4.2802	0.9838	−0.015
MgSi	4.2084	0.9400	0.099
TiAl	3.9918	1.0201	−0.409
TiSi	3.8932	0.9836	−0.495

compositions. With regards to hydrogen storage properties, experimental research shows that the hydrogen plateau pressure maximizes if the Mg content equals the Al content in the samples [27]. Mg and Si form a stable compound Mg_2Si with a cubic fluorite structure, where Si atoms occupy the corners and faces of a fcc cell and Mg atoms are in the tetrahedral interstitial positions [28]. It is well-known, however, that the formation of Mg_2Si inhibits the absorption of hydrogen [29]. The binary phase diagrams of Ti and Al or Si show several stable phases. The most stable alloys are obtained if the amount of Ti is equal to that of Al or Si [17, 30, 31].

With an eye on possible ternary Mg-Ti-X compounds, it should be noted that the solid solubility of Ti in Al or Si is much higher that of Ti in Mg [17]. Therefore, it might be expected that in a stable structure of Mg-Ti-X Ti is surrounded by Al or Si. TiAl crystalizes in a tetragonally distorted fcc structure with space group P4/mmm (123), the so-called $L1_0$ structure [31]. TiSi forms a similar $L1_0$ structure [30]. Both compounds are very stable, as illustrated by their calculated formation energies shown in Table 5.1. The formation energies per atom are calculated as

$$E_f = [E_{\text{MX}} - E_{\text{M}} - E_{\text{X}}]/n \tag{5.1}$$

where E_{MX}, E_{M} and E_{X} are total energies of the MX alloys (M = Mg or Ti, X = Al or Si) in the $L1_0$ structure, and the bulk metals M and X in their ground state structures, respectively; n is the number of atoms in the unit cell. Table 5.1 also shows the results for MgX in the $L1_0$ structure, confirming that TiX is indeed much more stable than the corresponding MgX. Yet MgAl and MgSi are more stable than MgTi, which indicates that adding Al or Si to a Mg-Ti alloy can stabilize it.

If one adds Si to Mg-Ti, the formation of Mg_2Si needs to be prevented, since the latter compound does not absorb hydrogen [29]. We consider the reaction
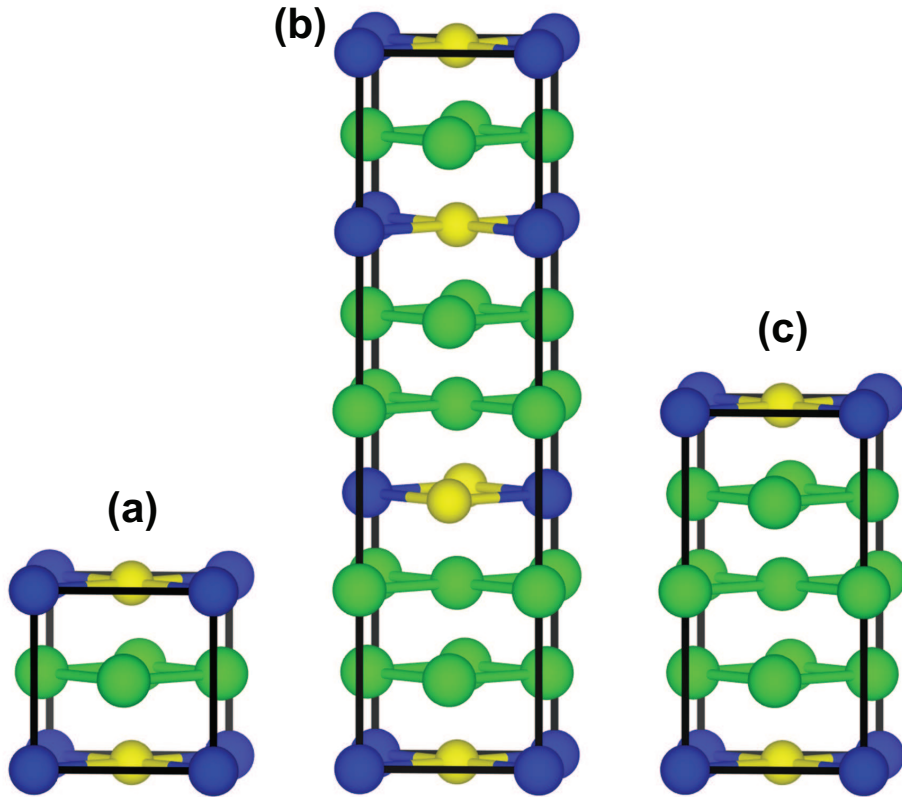
$$\text{Mg}_2\text{Si} + \text{Ti} \longleftrightarrow \text{TiSi} + 2\text{Mg} \tag{5.2}$$

Figure 5.1: (Color online) Layered $Mg_{(1-2y)}Ti_yX_y$ structures for (a) $y = 0.25$, (b) 0.1875 and (c) 0.125 compositions are shown. Mg, Ti and X (= Al or Si) atoms are shown as green, blue and yellow colored spheres, respectively. All structural drawings are produced using the VESTA software [32].

with Mg_2Si in the fluorite structure and TiSi in the $L1_0$ structure. Total energy calculations show that the materials on the right hand side of Eq. (5.2) are more stable by 0.35 eV per TiSi unit. Therefore, one can design the Mg-Ti-Si compound such, that the Ti captures the Si and prevents the formation of Mg_2Si.

5.4.2 Mg-Ti-Al,Si layered structures

In view of the stability of TiAl and TiSi it makes sense to look at ternary Mg-Ti-X alloys whose Ti:X ratio is fixed at 1:1, i.e. $Mg_{(1-2y)}Ti_yX_y$. In particular we study the compositions $y = 0.125$, 0.1875, and 0.25, which cover the experimentally reported

Table 5.2: The calculated formation energies with respect to the elemental solids of $Mg_{(1-2y)}Ti_yX_y$ in the layered structures, see Fig. 5.1.

	E_f (eV/atom)		
Compound	X = Ti	X = Al	X = Si
$Mg_{0.5}Ti_{0.25}X_{0.25}$	0.206	−0.083	−0.132
$Mg_{0.625}Ti_{0.1875}X_{0.1875}$	0.141	−0.015	−0.040
$Mg_{0.75}Ti_{0.125}X_{0.125}$	0.093	0.010	0.006

range of compositions that show interesting hydrogen storage properties [17].

We first look at relatively simple structures, which are based upon alternating atomic layers of TiX and Mg. One could envision such multilayers being formed by atomic beam epitaxy, for instance. Starting from the assumption that the atoms occupy fcc positions, the composition $Mg_{0.5}Ti_{0.25}X_{0.25}$ can be formed by alternating in the (001) direction one layer of TiX and one layer of Mg, as shown in Fig. 5.1. The composition $Mg_{0.75}Ti_{0.125}X_{0.125}$ can then be formed by alternating one layer of TiX with three layers of Mg. Following this strategy, the composition $Mg_{0.625}Ti_{0.1875}X_{0.1875}$ then becomes a more complex alternation of one TiX layer and one or two Mg layers. The resulting unit cells are shown in Fig. 5.1.

The formation energies per atom of these $Mg_{(1-2y)}Ti_yX_y$ structures are given in Table 5.2. They can be compared to the formation energies of layered $Mg_{(1-2y)}Ti_{2y}$ compounds with the same amount of Mg. Mg-Ti is quite unstable over the whole composition range with respect to phase separation into the elements. The formation energy of these layered Mg-Ti structures scales linearly with the Ti content, which one may attribute to the formation of Mg-Ti interfaces. It gives an interface energy of 0.45 eV per interface and atom. Adding Al or Si indeed increases the stability, as can be observed from the formation energies of $Mg_{(1-2y)}Ti_yX_y$.

5.4.3 Mg-Ti-Al,Si disordered structures

In the experiments so far, all three metals are deposited simultaneously [17]. As the structures are not known from experiment and a full computational search for the structure of a ternary alloy is computationally prohibitive, we start from the following assumptions. We position all metal atoms at fcc sites. Starting from MgTi we assume that there is no correlation between the positions of the Mg and the Ti atoms. Such random structures can be modeled in finite supercells by special quasirandom structures (SQSs) [33–35]. We use supercells containing 32 metal atoms
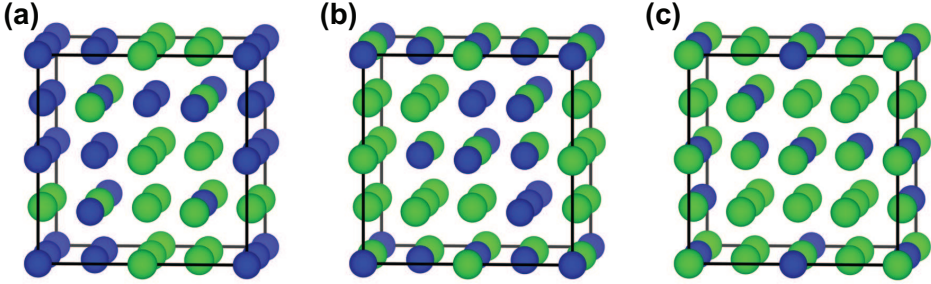
Figure 5.2: (Color online) Prototype Mg-Ti SQSs containing (a) 50, (b) 37.5 and (c) 25 at. % Ti are shown. Mg and Ti atoms are shown as green and blue colored spheres, respectively.

to model SQSs of $Mg_{(1-x)}Ti_x$, $x = 0.25, 0.375, 0.5$, and optimize their structure and cell parameters. Examples of such structures are given in Fig. 5.2.

Adding a third element in the composition $Mg_{(1-2y)}Ti_yX_y$ means that half of the Ti atoms should be replaced by X atoms, where X = Al or Si. From the discussion in the previous sections one might guess that X atoms have a preference to be bonded to Ti, rather than Mg atoms. To examine whether there is such a preference, the coordination numbers N_{Ti} of each Ti by Ti atoms in the nearest neighbor shells, are calculated for the SQSs of $Mg_{(1-x)}Ti_x$. If we replace a Ti atom with a large N_{Ti} by an X atom, the latter will then be surrounded mainly by nearest neighbor Ti atoms, whereas replacing a Ti atom with a small N_{Ti} results in the X atom being surrounded mainly by Mg atoms.

We order the Ti atoms in the SQSs of $Mg_{(1-x)}Ti_x$ according to their N_{Ti} values and consider three scenarios for replacing half of them by X atoms. In the first scenario Ti atoms with the largest N_{Ti} are replaced, which leads a maximum coordination of X atoms by Ti or X atoms. We call this the high coordination (H) structure in the following. In contrast, in the second scenario only Ti atoms with small N_{Ti} are replaced, giving X atoms that are mostly surrounded by Mg atoms, which we call low (L) coordination. The third scenario is a case of mixed (M) coordination, where half of the replaced Ti atoms have a large N_{Ti} and half of them have a small N_{Ti}. This M structure mainly serves as a check on the results obtained for the L and M cases. It should be noted that in the L (H) structure the Ti atoms that remain in $Mg_{(1-2y)}Ti_yX_y$ all have a large (small) N_{Ti}.

The formation energies with respect to the elements of the $Mg_{(1-2y)}Ti_yX_y$ structures constructed via these three scenarios are presented in Table 5.3. They can be

Table 5.3: Calculated formation energies, E_f (eV/atom), with respect to the elemental solids of $Mg_{(1-2y)}Ti_yX_y$ in the disordered structures. The construction of the L, H, and M structures is discussed in the text.

Compound	X = Ti	X = Al			X = Si		
		L	H	M	L	H	M
$Mg_{0.5}Ti_{0.25}X_{0.25}$	0.156	−0.008	0.052	0	−0.066	0.006	−0.035
$Mg_{0.625}Ti_{0.1875}X_{0.1875}$	0.153	0.025	0.091	0.046	−0.020	0.064	0.020
$Mg_{0.75}Ti_{0.125}X_{0.125}$	0.110	0.035	0.058	0.063	0.038	0.058	0.064

compared to the formation energies of the corresponding $Mg_{(1-2y)}Ti_{2y}$ structures. Apparently, Al and Si both have a stabilizing effect on the Mg-Ti compounds, irrespective of where these atoms are positioned, with Si having a larger effect than Al. Moreover, the stability of $Mg_{(1-2y)}Ti_yX_y$ increases with increasing y. However, on an absolute scale only the structures with $y = 0.25$ for Al and $y = 0.25, 0.1875$ for Si are thermodynamically stable with respect to decomposition into the elements.

Comparing the L, H, and M structure in Table 5.3 one observes that the relative ordering of the metal atoms can have a sizable effect on the formation energies. Perhaps somewhat contra-intuitively the L case yields the lowest energy, whereas the H case gives the highest energy. In the L structures the Al or Si atoms have a small N_{Ti}, meaning that they are mainly surrounded by Mg atoms, which in view of Table 5.1 does not seem to give much stabilization. However, the Ti atoms that remain in the L structure all have a large N_{Ti}, which means that they are mainly surrounded by Ti atoms. This minimizes the number of direct Mg-Ti contacts that decrease the stability. Thus the maximum beneficial effect on the formation energy of adding X (= Al, Si) in these structures is not so much in forming close Ti-X contacts, but in preventing direct Mg-Ti contacts. Since the Ti atoms in the H structure all have a small N_{Ti}, the number of Mg-Ti contacts is large, and the energy of this structure is higher that of the L structure. The energies of the M structures are between that of the L and H structures, which is in line with this analysis. An exception to this rule is the composition $Mg_{0.75}Ti_{0.125}X_{0.125}$. Here however the Mg content is so large that the spread in N_{Ti} is not large, which makes the distinction between sites with large and small N_{Ti} a bit arbitrary.

Comparing the formation energies of the layered structures, Table 5.2, to those of the disordered structures, Table 5.3, one observes that the layered structures are more stable. This may provide new ideas for structures with interesting properties, formed by immiscible elements.

Table 5.4: Calculated hydrogenation energies E_h (eV/H$_2$) of $Mg_{(1-2y)}Ti_yX_yH_2$ in the layered and the disordered L structures. The second and the fifth column represent the formation energies of the corresponding $Mg_{(1-2y)}Ti_{2y}H_2$ structures.

	layered			disordered L		
Compound	X = Ti	X = Al	X = Si	X = Ti	X = Al	X = Si
$Mg_{0.5}Ti_{0.25}X_{0.25}H_2$	-1.118	-0.178	0.335	-1.120	-0.358	-0.156
$Mg_{0.625}Ti_{0.1875}X_{0.1875}H_2$	-0.906	-0.278	0.093	-0.981	-0.468	-0.240
$Mg_{0.75}Ti_{0.125}X_{0.125}H_2$	-0.711	-0.317	-0.086	-0.807	-0.501	-0.434

5.5 Mg-Ti-Al,Si Hydrides

In this section we discuss the energetics of Mg-Ti-Al,Si hydrides. In previous studies we have shown that a fluorite-type cubic structure of $Mg_{(1-x)}Ti_xH_2$ is more stable than the MgH$_2$ rutile-type structure for $x \gtrsim 0.1$-0.2 [10, 26]. In the following we assume that replacing half of the Ti atoms by Al or Si maintains the fluorite structure. Experimentally the (de)hydrogenation kinetics of Mg-Ti-X (= Al, Si) is comparably fast as that of Mg-Ti, which is attributed to the existence of a fluorite structure [17]. We use the structural models of the Mg-Ti-X alloys discussed in the previous sections and position hydrogen atoms in the tetrahedral interstitial sites to obtain fluorite-type $Mg_{(1-2y)}Ti_yX_yH_2$ structures. For the disordered systems we use the L structures, since these give the lowest energies for the alloys. Subsequently all cell parameters and geometries of these hydrides are optimized.

We calculate the hydrogenation energies according to

$$E_h = E_{Mg_{(1-2y)}Ti_yX_yH_2} - E_{Mg_{(1-2y)}Ti_yX_y} - E_{H_2}, \tag{5.3}$$

where $E_{Mg_{(1-2y)}Ti_yX_yH_2}$, $E_{Mg_{(1-2y)}Ti_yX_y}$, and E_{H_2} are the total energies of the hydride, the corresponding alloy, and the hydrogen molecule, respectively. The calculated hydrogenation energies are given in Table 5.4.

The results clearly show that the hydrides $Mg_{(1-2y)}Ti_yX_yH_2$ are much less stable than their corresponding $Mg_{(1-2y)}Ti_{2y}H_2$, whether in the simple, layered structures, or in the disordered structures. Since the alloys $Mg_{(1-2y)}Ti_yX_y$ are more stable than their corresponding $Mg_{(1-2y)}Ti_{2y}$, see Tables 5.2 and 5.3, this is an example of van Mal's rule [36]. The latter states that stabilization of an alloy phase is accompanied by a destabilization of its hydride. Van Mal's rule also holds if one compares the layered structures to the disordered structures. The layered structures of the $Mg_{(1-2y)}Ti_yX_y$

alloys are more stable then their corresponding disordered structures, compare Tables 5.2 and 5.3. One then expects the hydrides $Mg_{(1-2y)}Ti_yX_yH_2$ to be less stable in the layered structures than in the disordered structures, as indeed can be observed in Table 5.4. Moreover, since Mg-Ti-Si alloys are more stable than Mg-Ti-Al alloys, one may expect that Mg-Ti-Si hydrides are less stable than Mg-Ti-Al hydrides. The results in Table 5.4 confirm this.

We now consider the hydrogenation energies in a more quantitative way. A hydrogenation energy of ~ -0.4 eV/H_2 gives an equilibrium hydrogen pressure of ~ 1 bar at room temperature [2, 3]. Even with this hydrogenation energy the amount of heat released in a very short time when a bulk material is loaded with hydrogen, can be a problem in some applications. Therefore, depending on the application a hydrogenation energy between ~ -0.15 and ~ -0.4 eV/H_2 is required. Starting with the pure Mg-Ti alloys one observes that their hydrogenation energies are far outside this range. They are in fact larger or comparable to the hydrogenation energy of pure Mg [10, 26].

The addition of Al or Si markedly destabilizes the hydrides and brings the hydrogenation energies into the range required for possible applications, where Si has a larger effect than Al. The effects are particularly large in the layered structures. In fact, $Mg_{(1-2y)}Ti_ySi_yH_2$ in a layered structure is unstable, or marginally stable for the compositions we studied. In contrast, the hydrogenation energy of $Mg_{(1-2y)}Ti_yAl_y$ is ~ -0.3 eV/H_2. Moreover, the alloy $Mg_{(1-2y)}Ti_yAl_y$ is stable with respect to decomposition into the elements for $y = 0.1875, 0.25$, and only marginally unstable for $y = 0.125$, see Table 5.2. These properties indicate that $Mg_{(1-2y)}Ti_yAl_y$ in layered form is potentially a promising material for hydrogen storage.

The layered structures of $Mg_{(1-2y)}Ti_yX_yH_2$ are relatively simple. Hydrogen atoms occupy positions at, or close to the tetrahedral interstitial sites, as one would expect of a fluorite structure, see Fig. 5.3. Such an atomic arrangement could be advantageous for fast hydrogen kinetics.

Also in the disordered structures does the addition of Al or Si destabilize the hydrides, although the effects are not as large as in the layered structures. Again Si has a larger effect than Al, but the hydrogenation energies of all compositions studied are markedly better than those of pure Mg, or Mg-Ti, in accordance with the experimental findings [17]. If one demands that the $Mg_{(1-2y)}Ti_yX_y$ alloys are stable with respect to decomposition into the elements,then for X = Al, Si, one needs $y = 0.25$ and $y = 0.1875, 0.25$, respectively, see Table 5.3, which gives hydrogenation energies ranging from -0.22 to -0.37 eV/H_2.

The optimized structures of the disordered L structures are shown in Fig. 5.4. The
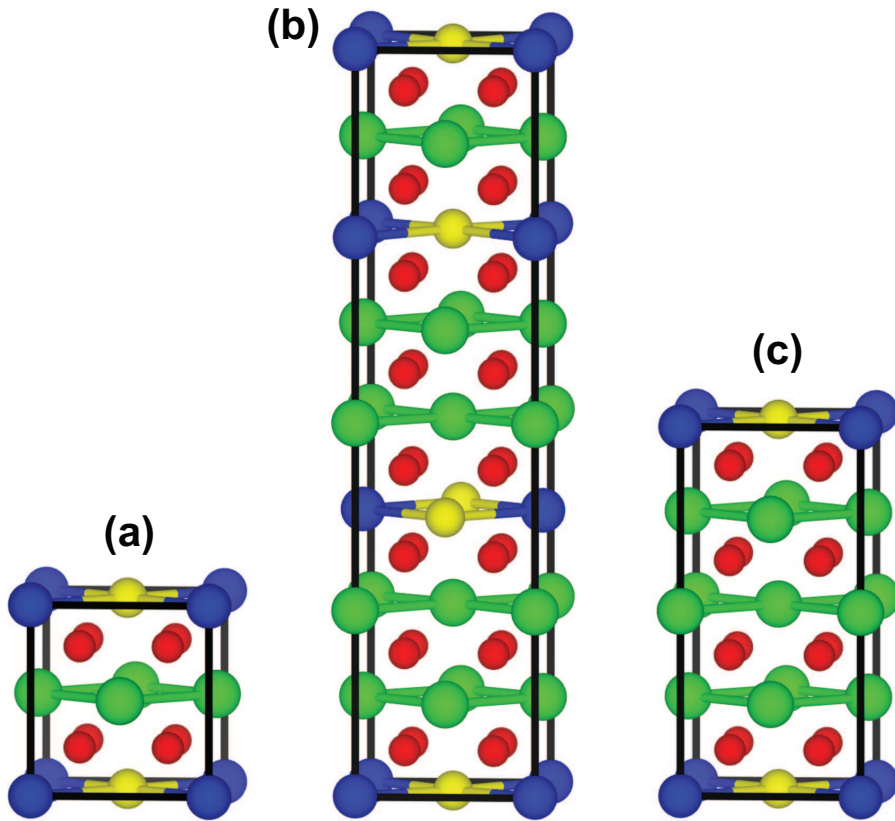
Figure 5.3: (Color online) Optimized structures of $Mg_{(1-2y)}Ti_yAl_yH_2$ in layered form. Hydrogen atoms are shown as red colored spheres. The compositions with (a) $y = 0.25$, (b) 0.1875, and (c) 0.125 are shown from left to right.

top row shows Mg-Ti-X compounds with decreasing Ti content from left to right. The hydrogen atoms stay close to the tetrahedral interstitial sites in almost every case, which makes these structures fluorite-like. The largest deviations are observed for the composition with the lowest Ti content (or highest Mg content). The hydrogens close to the Mg atoms then start to assume positions that are typical for the cubic β-phase of MgH_2, as is explained in detail in Ref. [26]. In a fluorite MH_2 structure each metal atom M is cubically coordinated by eight hydrogen atoms. This is perfect if M = Ti (TiH_2 has the fluorite structure), but Mg prefers a octahedral coordination (which occurs both in rutile α-MgH_2, and cubic β-MgH_2).

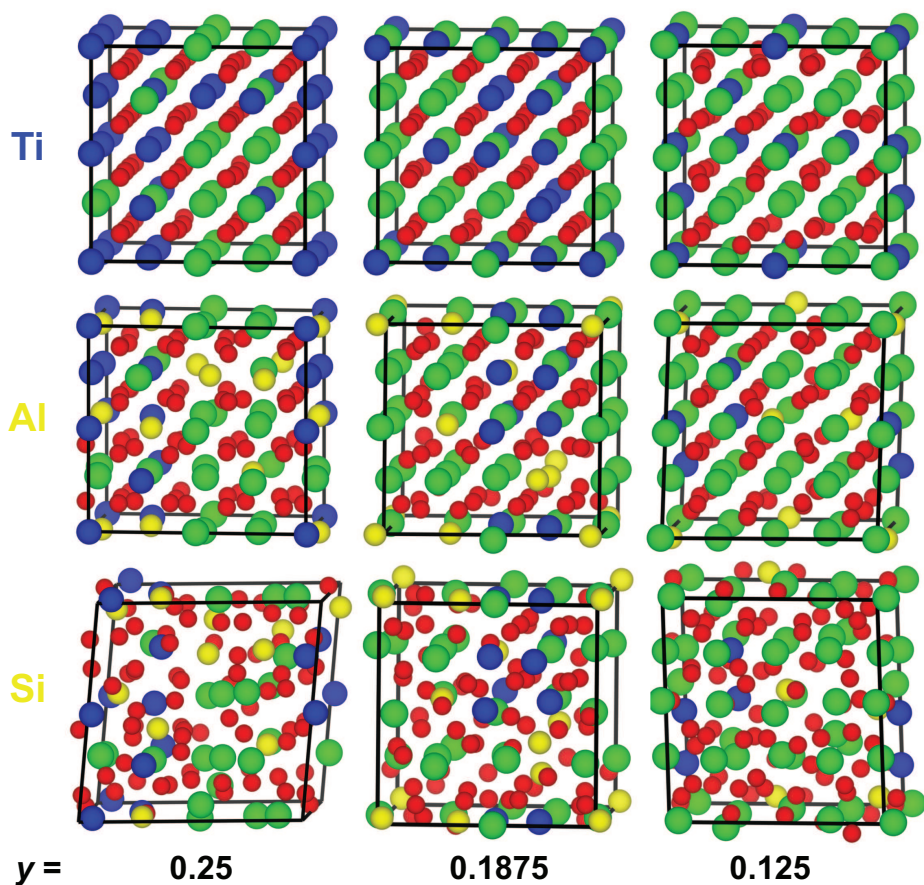**Figure 5.4:** (Color online) Optimized structures of $Mg_{(1-2y)}Ti_yX_yH_2$ in the disordered L structure. The columns from left to right are for the compositions $y = 0.25, 0.1875$, and 0.125, respectively. The rows from top to bottom are for X = Ti, Al, and Si, respectively.

The middle and bottom rows of Fig. 5.4 show the fully optimized structures of $Mg_{(1-2y)}Ti_yAl_yH_2$ and $Mg_{(1-2y)}Ti_ySi_yH_2$, respectively, for the different compositions. It is clear that the positions of the hydrogen atoms are noticeably shifted from the tetrahedral interstitial sites. Both Mg and Al prefer an octahedral coordination by hydrogen atoms, which is different from the cubic coordination found in a fluorite structure. Si prefers a tetrahedral coordination, which explains why the structure of $Mg_{(1-2y)}Ti_ySi_yH_2$ deviates substantially from a fluorite-type structure.

Acknowledgments

Bibliography

[1] See the special issue *Toward a Hydrogen Economy*, by R. Coontz and B. Hanson, Science **305**, 957 (2004).

[2] L. Schlapbach and A. Züttel, Nature **414**, 353 (2001).

[3] A. Züttel, Naturwiss. Unterr. Chem. **91**, 157 (2004).

[4] J. F. Stampfer Jr., C. Holley Jr., and J. F. Suttle, J. Am. Chem. Soc. **82**, 3504 (1960).

[5] K. H. J. Buschow, P. C. P. Bouten, and A. R. Miedema, Rep. Prog. Phys. **45**, 937 (1982).

[6] R. A. H. Niessen and P. H. L. Notten, Electrochem. Solid-State Lett. **8**, A534 (2005).

[7] R. A. H. Niessen and P. H. L. Notten, J. Alloys Compd. **404**, 457 (2005).

[8] P. Vermeulen, R. A. H. Niessen, and P. H. L. Notten, Electrochem. Commun. **8**, 27 (2006).

[9] D. Borsa *et al.*, Phys. Rev. B **75**, 205408 (2007).

[10] S. Er, D. Tiwari, G. A. de Wijs, and G. Brocks, Phys. Rev. B **79**, 024105 (2009).

[11] T. Mitchell, S. Diplas, P. Tsakiropoulos, and J. F. Watts, Philos. Mag. A **82**, 841 (2002).

[12] G. Liang and R. Schulz, J. Mater. Sci. **38**, 1179 (2003).

[13] S. Rousselot, M. P. Bichat, D. Guay, and L. Roue, J. Power Sources **175**, 621 (2008).

[14] D. M. Borsa *et al.*, Appl. Phys. Lett. **88**, 241910 (2006).

[15] P. Vermeulen *et al.*, Electrochem. Solid-State Lett. **9**, A520 (2006).

[16] M. Slaman *et al.*, Sens. Actuators: B **123**, 538 (2007).

[17] P. Vermeulen, E. F. M. J. van Thiel, and P. H. L. Notten, Chem. Eur. J. **13**, 9892 (2007).

[18] J. P. Perdew and Y. Wang, Phys. Rev. B **45**, 13244 (1992).

[19] P. E. Blöchl, Phys. Rev. B **50**, 17953 (1994).

[20] G. Kresse and D. Joubert, Phys. Rev. B **59**, 1758 (1999).

[21] G. Kresse and J. Hafner, Phys. Rev. B **47**, 558 (1993).

[22] G. Kresse and J. Furthmüller, Phys. Rev. B **54**, 11169 (1996).

[23] G. Kresse and J. Furthmüller, Comput. Mater. Sci. **6**, 15 (1996).

[24] M. Methfessel and A. T. Paxton, Phys. Rev. B **40**, 3616 (1989).

[25] P. E. Blöchl, O. Jepsen, and O. K. Andersen, Phys. Rev. B **49**, 16223 (1994).

[26] S. Er, M. J. van Setten, G. A. de Wijs, and G. Brocks, submitted (2009).

[27] A. Zaluska, L. Zaluski, and J. O. Ström-Olsen, Appl. Phys. A: Mater. Sci. Process. **72**, 157 (2001).

[28] A. A. Nayeb-Hashemi and J. B. Clark, J. Phase Equilib. Diffus. **5**, 584 (1984).

[29] J. J. Vajo, F. Mertens, C. C. Ahn, R. C. B. Jr, and B. Fultz, J. Phys. Chem. B **108**, 13977 (2004).

[30] M. Ekman and V. Ozoliņš, Phys. Rev. B **57**, 4419 (1998).

[31] I. Ohnuma *et al.*, Acta Mater. **48**, 3113 (2000).

[32] K. Momma and F. Izumi, IUCr Newslett. **7**, 106 (2006).

[33] A. Zunger, S. H. Wei, L. G. Ferreira, and J. E. Bernard, Phys. Rev. Lett. **65**, 353 (1990).

[34] C. Wolverton, V. Ozolins, and A. Zunger, J. Phys.: Condens. Matter **12**, 2740 (1999).

[35] A. V. Ruban, S. I. Simak, S. Shallcross, and H. L. Skriver, Phys. Rev. B **67**, 214302 (2003).

[36] H. H. van Mal, K. H. C. Buschow, and A. R. Miedema, J. Less-Common Met. **35**, 65 (1974).

Part – B
Molecular Hydrogen Storage

Chapter 6

Hydrogen storage by polylithiated molecules and nanostructures

6.1   Abstract

We study polylithiated molecules as building blocks for hydrogen storage materials, using first-principles calculations. CLi_4 and OLi_2 bind 12 and 10 hydrogen molecules, respectively, with an average binding energy of 0.10 and 0.13 eV, leading to gravimetric densities of 37.8 and 40.3 weight % H_2. Bonding between Li and C or O is strongly polar and H_2 molecules attach to the partially charged Li atoms without dissociating, which is favorable for (de)hydrogenation kinetics. CLi_n and OLi_m molecules can be chemically bonded to graphene sheets to hinder the aggregation of such molecules. In particular B or Be doped graphene strongly bind the molecules without seriously affecting the hydrogen binding energy. It still leads to a hydrogen storage capacity in the range 5-8.5 wt.% H_2.

6.2   Introduction

In recent years we observe a widespread effort aimed at finding alternatives to fossil fuels. The goal is to apply renewable resources that meet the increasing global demand for energy, while at the same time cut down CO_2 emissions [1]. Hydrogen is

a potential energy carrier, since it can be produced sustainably and is one of the most abundant elements [2]. Burning hydrogen does not affect the environment as only water is produced. On board utilization of hydrogen on a large scale is hampered, however, by the lack of efficient hydrogen storage systems. Some of the methods suggested so far are high pressure gas tanks, low temperature liquid hydrogen tanks, chemical solid state storage such as metal-hydrides, and physisorption of hydrogen by materials with a high surface area [3]. Physisorption offers the possibility of storing hydrogen in molecular form. From kinetic considerations this is advantageous over chemical storage in atomic form, which requires dissociation of the hydrogen bond and the formation of a hydride.

Materials that are mainly based upon carbon are cheap, lightweight, and can have large internal surfaces. The bottleneck of physisorption by such materials lies in the weak interaction of hydrogen molecules with the host materials [4]. From thermodynamic principles it can be shown that, for storage of hydrogen in physisorbed form at 30 bar under ambient temperature, and delivery at 1.5 bar, the optimum adsorption enthalpy of the hydrogen molecules is 0.15 eV/H_2 [5]. As the adsorption enthalpy of hydrogen on activated carbon is only ~ 0.05 eV/H_2 [6], very low temperatures or high pressures are necessary to attain meaningful storage capacities in carbon materials. One can imagine encapsulating hydrogen in carbon nanocages, but the applicability of such systems is unknown at present [7]. At the moment none of the above methods have achieved all requirements of a hydrogen storage system.

Previous studies have shown that isolated metal atoms or ions can bind hydrogen molecules, where the type of bonding depends on the metallic species. Transition metal atoms bind hydrogen molecules through weak multicenter chemical bonds called Kubas bonds [8–10]. Alkali and alkaline earth ions bind hydrogen molecules through electrostatic (charge-multipole) and polarization (charge-induced multipole) interactions [11]. Of particular interest is the lightweight Li^+ ion, which can bind up to six hydrogen molecules with an average binding energy of 0.19 eV/H_2 [12]. This is close to the optimal binding energy of 0.15 eV/H_2 [5]. For this type of bonding it is essential that Li is ionized. Moreover, Li atoms need to be prevented from clustering, as, for instance, steric hindrance would result in a significant reduction of the amount of hydrogen molecules that can be bonded. Recent research therefore focuses on the hydrogen storage properties of Li-doped carbon nanostructures [12–27]. A limited amount of Li can be introduced by doping without the Li atoms clustering, consequently restricting the wt.% of adsorbed hydrogen significantly.

Polylithiated molecules are species that contain a large density of Li atoms. Such molecules have been studied experimentally and theoretically for a number of years,

but never with an eye on their potential for hydrogen storage. The main focus has been on the interaction of single atoms such as C or O, with multiple Li atoms. The first polylithiated molecule, OLi_3, has been identified by mass spectroscopy by Wu *et al.* [28] and its bonding characterized quantum chemically by Schleyer *et al.* [29]. The latter group has also predicted the existence of the carbon based polylithiated molecules CLi_5 and CLi_6 [30], which has later been confirmed experimentally by Kudo [31]. These studies have stimulated extensive research into the properties of CLi_n and OLi_m molecules [32–38]. C−Li and O−Li bonds are strongly polar, resulting in a significant positive charge on the Li atoms. This should facilitate electrostatic bonding to hydrogen molecules, as discussed above.

In this paper we study hydrogen storage properties of the polylithiated molecules CLi_n, $n = 3$-5 and OLi_m, $m = 1$-4. We find that each Li atom can bind multiple hydrogen molecules and that the binding energy increases with the partial charge on the Li atom. In particular, a CLi_4 molecule binds up to 12 and an OLi_2 molecule up to 10 hydrogen molecules, with binding energies in the range of 0.10-0.14 and 0.13-0.21 eV/H_2, respectively. The corresponding gravimetric storage densities are 37.8 wt.% H_2 for CLi_4H_{24} and 40.3 wt.% H_2 for OLi_2H_{20}. Such extremely high densities make polylithiated molecules fascinating building blocks for hydrogen storage materials. Aggregation of CLi_n or OLi_m molecules would be detrimental for the reversibility of hydrogenation. Therefore we explore the possibilities of attaching polylithiated molecules to carbon nanostructures, in particular graphene, in order to immobilize them. Using dopants such as B or Be, one can increase the binding of the molecules to the substrate, without weakening the binding of hydrogen to the molecules. This scenario leads to several interesting structures with gravimetric densities > 5 wt.% H_2.

6.3   Computational Details

The calculations are performed at the level of density functional theory (DFT), using the PW91 generalized gradient approximation (GGA) [39], and the projector augmented wave (PAW) method [40, 41], as implemented in the Vienna *ab initio* simulation package (VASP) [42, 43]. The PAW potentials treat the H $1s$, Li and Be $1s$, $2s$, B, C and O $2s$, $2p$ as valence electrons. With a plane wave kinetic energy cutoff of 518 eV the total energies are converged on a scale of 10^{-3} eV/atom. Geometries are optimized without any symmetry constraints, using the conjugate gradient (CG) algorithm. Convergence criteria of 10^{-4} eV and 0.02 eV/Å are applied for the energy difference between consecutive electronic steps and the total remaining forces on the

atoms, respectively.

Single molecules are treated within a cubic box with a cell parameter of 20 Å, using periodic boundary conditions and Γ-point sampling. In the graphene systems to be discussed below we use a 4×4 in-plane graphene supercell and a 3×3 regular **k**-point mesh to sample the Brillouin Zone (BZ). The final total energies and charge densities of the optimized structures are obtained using the corrected linear tetrahedron method[44]. The optimized geometries of a number of structures discussed in this paper are given in the supporting information. The structures are visualized using the VESTA program. The same program is used to generate the files in the supporting information [45].

The PW91 functional in combination with PAW potentials have been used previously to study the hydrogen binding properties of Li coated C_{60}, $B_{12}C_{48}$ and B_{80} fullerenes [20, 26, 27]. To have an indication of the error bar on the total energies of the structures studied in this paper, obtained with the PW91 GGA functional, we repeat the calculations using the PBE GGA functional [46, 47]. Generally, the results we obtain with these two functionals are very similar. The binding energies of H_2 molecules to polylithiated molecules and nanostructures obtained with the PBE functional are ~ 20 meV/H_2 lower than those obtained with the PW91 functional, whereas dimerization energies of polylithiated molecules obtained with PBE are 20-60 meV/monomer lower. As these differences are small and uniform, we only give the PW91 results in the following.

6.4   Results and Discussion

6.4.1   Polylithiated Molecules

First we analyze the interaction of molecular hydrogen with CLi_n and OLi_m molecules. As the electron affinities of C and O are much larger than that of Li, the C−Li and O−Li bonds are very polar. If C and O become hypercoordinated by Li atoms, i.e. CLi_n with $n \geq 5$, or OLi_m with $m \geq 3$, the Li coordination shells become increasingly metallic and the average charge on the Li atoms decreases. The binding of hydrogen to these atoms is dominated by electrostatic and polarization interactions. Therefore, to maximize hydrogen binding energies, the charge on the Li atoms should be maximal and one needs to avoid hypercoordination of the C or O atoms. In CLi_4 or OLi_2 all valence electrons are involved in C−Li and O−Li bonds, respectively, maximizing the charge on the Li atoms. The most stable geometries of CLi_4 and OLi_2 have a high symmetry, i.e. T_d and $D_{\infty h}$, respectively. All Li atoms
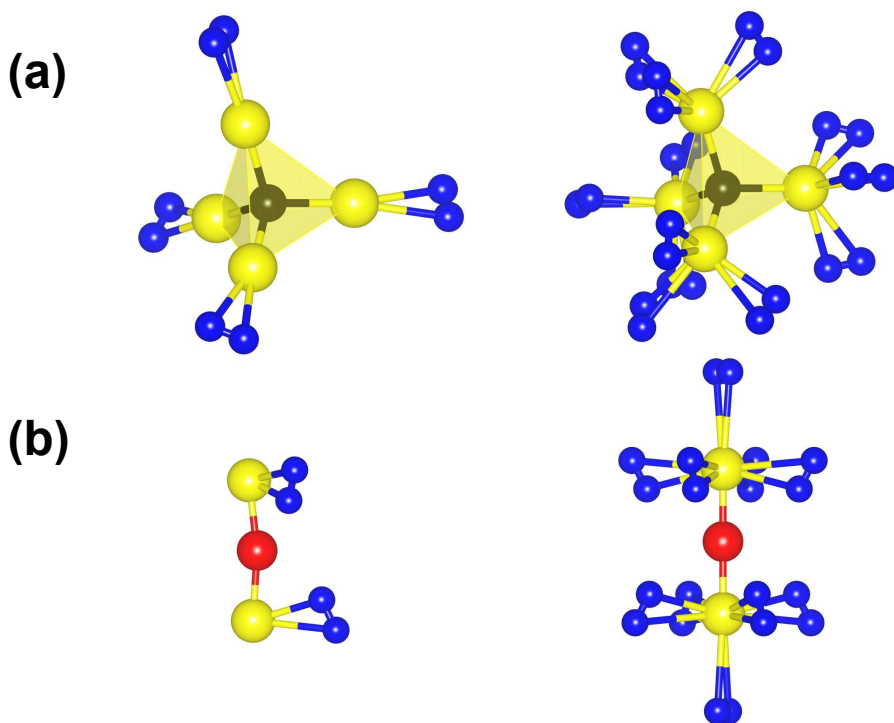
Figure 6.1: Optimized geometries of (a) CLi_4H_8, CLi_4H_{24}, and (b) OLi_2H_4, OLi_4H_{20} complexes. Carbon, oxygen, lithium and hydrogen atoms are shown as black, red, yellow and blue spheres, respectively.

in a molecule are then equivalent.

A Bader charge analysis of the calculated self-consistent charge densities gives a charge of +0.82e on each of the Li atoms in CLi_4, and a charge of +0.88e on the Li atoms in OLi_2 [48]. These high charges facilitate the electrostatic bonding of hydrogen molecules to the Li atoms in these molecules, similar to that in isolated Li^+ ions [12]. Hydrogen molecules then cluster around the Li sites of the CLi_4 and OLi_2 molecules. Examples of the structures of hydrogenated molecules are shown in 6.1 and bond lengths before and after hydrogenation are given in 6.1.

Also given in 6.1 are the hydrogen binding energies, which are calculated by subtracting the total energy of the hydrogenated polylithiated molecules from the sum of the total energies of the isolated polylithiated molecules and the hydrogen molecules, divided by the number of hydrogen molecules. Each Li atom in a CLi_4 molecule can bind three H_2 molecules as shown in 6.1, which leads to 37.8 wt.% H_2. The average

Table 6.1: Calculated bond lengths (Å), Bader charges (e), hydrogen binding energies $E_b^{H_2}$ (eV/H$_2$) and gravimetric hydrogen densities of CLi$_4$ and OLi$_2$ molecules. For Li$-$H$_2$ the bonding distance is measured between Li atom and the center of H$-$H bonds. The average numbers are given and the numbers in parentheses indicate the spreads.

Molecule	bond lengths (Å)			charge on Li	$E_b^{H_2}$	wt. % H$_2$
	C,O$-$Li	Li$-$H$_2$	H$-$H			
CLi$_4$	1.898(3)	$-$	$-$	+0.819(2)	$-$	$-$
CLi$_4$H$_8$	1.888(5)	2.036(12)	0.756(0)	+0.827(2)	0.14	16.86
CLi$_4$H$_{24}$	1.908(3)	2.158(7)	0.763(2)	+0.851(3)	0.10	37.82
OLi$_2$	1.643(0)	$-$	$-$	+0.876(0)	$-$	$-$
OLi$_2$H$_4$	1.671(1)	1.862(5)	0.793(0)	+0.869(0)	0.21	11.89
OLi$_2$H$_{20}$	1.711(1)	2.140(144)	0.764(13)	+0.881(1)	0.13	40.29

binding energy decreases from 0.14 eV for the first H$_2$ molecule (per Li atom), to 0.10 eV for the fully hydrogenated state. The decrease reflects a net repulsive interaction between the H$_2$ molecules surrounding a Li atom. Steric hindrance prevents binding a fourth H$_2$ (at least with a binding energy > 0.04 eV). The H$_2$ binding energies are consistent with those found for isolated Li$^+$ ions, bearing in mind that the Li atoms in CLi$_4$ have a somewhat reduced charge [11].

OLi$_2$ molecules bind hydrogen more strongly than CLi$_4$ molecules. As the net charge on a Li atom in OLi$_2$ is larger than in CLi$_4$ this can be expected if the binding is electrostatic. Because the Li atoms in OLi$_2$ are less crowded than in CLi$_4$, each Li atom can accommodate up to five H$_2$ molecules, before steric hindrance prevents binding of additional hydrogen. The average binding energy decreases from 0.21 eV for the first H$_2$ molecule (per Li atom) to 0.13 eV in the fully hydrogenated state. It leads to 40.3 wt.% H$_2$ for the OLi$_2$H$_{20}$ complex.

The fully hydrogenated CLi$_4$H$_{24}$ and OLi$_2$H$_{20}$ complexes keep a high symmetry, i.e. T_d and D_{2d}, respectively. In intermediate hydrogenation stages the symmetry can be broken, see 6.1. After hydrogenation the C$-$Li and O$-$Li bonds are stretched by 1% respectively 4%. This is accompanied by a slight increase of the partial charge on Li by 4% respectively 0.6%. The optimized calculated bond length of an isolated H$_2$ molecule is 0.748 Å. 6.1 shows that in the complexes the H$-$H bond lengths increase by 1-6%. The limited size of these changes agrees with the notion of a weak interaction with the H$_2$ molecules. The absolute size of these changes generally correlates with the binding energy.
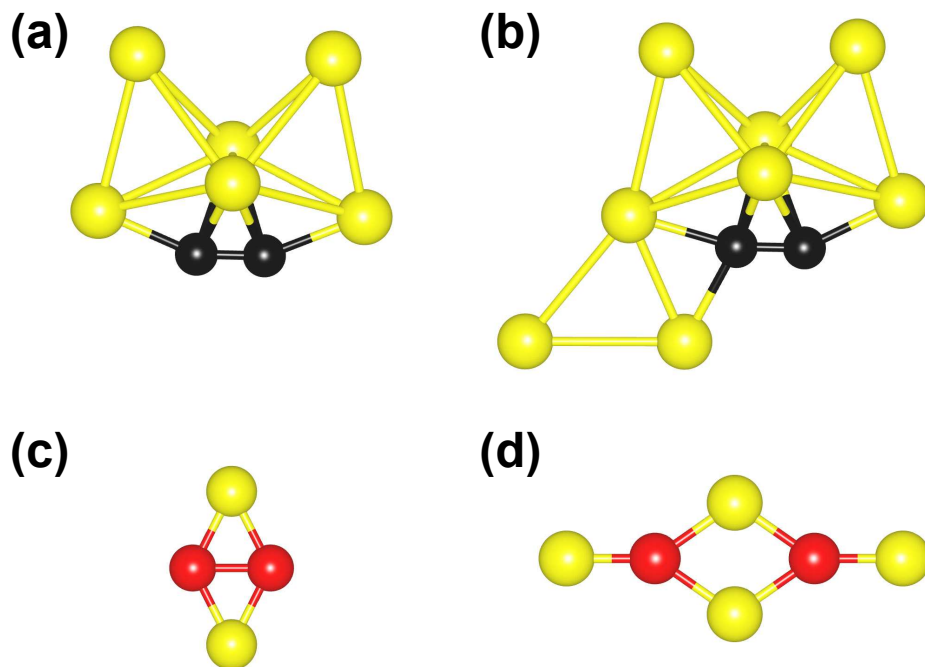
Figure 6.2: Optimized geometries of (a) $(CLi_3)_2$, (b) $(CLi_4)_2$, (c) $(OLi)_2$ and (d) $(OLi_2)_2$.

6.4.2 Adsorption on Graphene

It is clear that individual CLi_4 and OLi_2 molecules can bind a substantial number of H_2 molecules. In order to maintain reversibility during repeated hydrogen loading and unloading cycles, one should however prevent the formation of clusters or aggregates of CLi_4 or OLi_2 molecules. From a thermodynamic point of view such clusters could form. For instance, the equilibrium geometry of C_2Li_8 is shown in 6.2(b) [49]. The energy of this structure is 2.54 eV/CLi_4 lower in energy than that of two separate CLi_4 molecules. Similarly, two OLi_2 molecules can form a cluster with a binding energy of 1.37 eV/OLi_2, see 6.2(d). Presumably also structures of larger clusters exist that have a favorable binding energy. One could rely on kinetic barriers preventing clustering of polylithiated molecules. Here we consider alternative possibilities, which consist of immobilizing the molecules by binding them to a holder template. Microporous carbon and carbon nanostructures would be obvious substrates for these molecules.
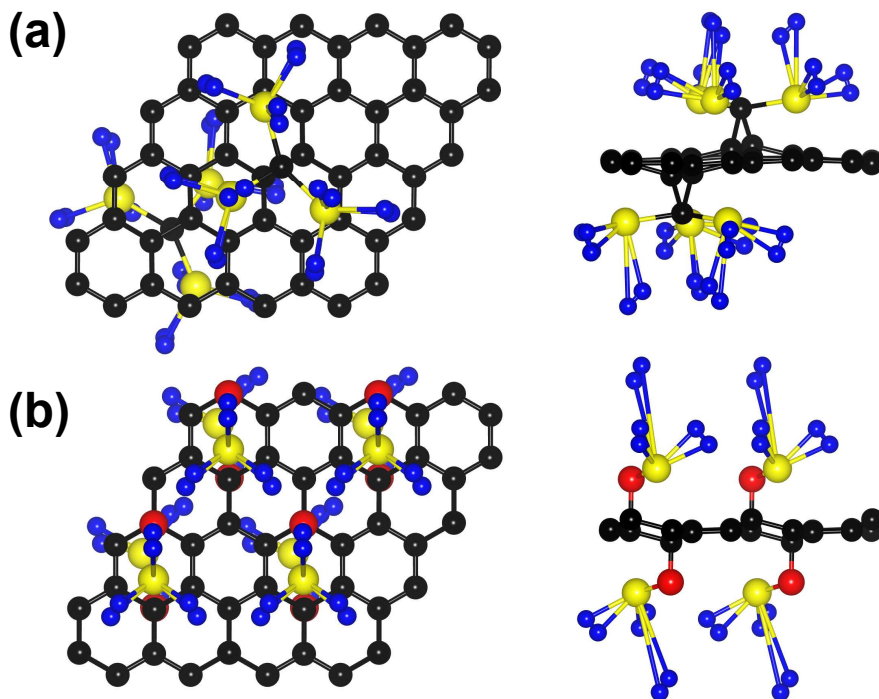
Figure 6.3: Top and side views of the optimized geometries of graphene binding (a) two CLi_3 molecules, or (b) four OLi molecules per supercell, in their fully hydrogenated forms.

As a prototype system we consider binding to a single sheet of graphite, i.e. to graphene. We use a 4×4 graphene supercell, which contains 32 atoms and has an optimized cell parameter of 9.866 Å. This cell is sufficiently large to prevent a direct interaction between molecules bonded to graphene in neighboring cells. The calculated binding energies of single CLi_4 and OLi_2 molecules bonded to graphene are 0.73 and 0.55 eV, respectively. Both of these energies are considerably smaller than the corresponding molecular dimerization energies, indicating that the interaction with the substrate is not sufficiently strong. One has to consider increasing this interaction.

For this we pursue two different strategies consisting of modifying the molecules or the substrate, respectively. Removing one Li atom from CLi_4 or OLi_2 strengthens the bonding to graphene. The calculated binding energy between CLi_3 and graphene is 2.00 eV. CLi_3 molecules on graphene are preferably positioned over the center of
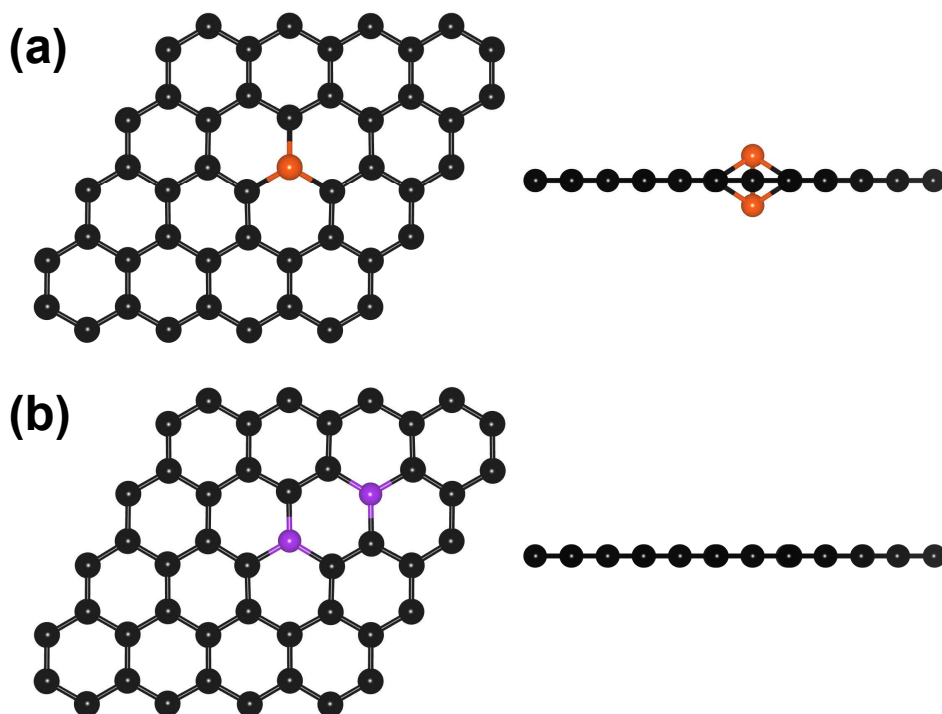
Figure 6.4: Top and side views of the optimized geometries of the (a) Be doped and (b) B doped graphene structures.

C−C bonds. Both faces of graphene can be functionalized, which leads to a geometry as shown in 6.3(a). This structure is stable, but it is not the absolute minimum energy structure. C_2Li_6 in its equilibrium structure, cf. 6.2(a) [50], has a binding energy of 3.86 eV/CLi_3 with respect to two separate CLi_3 molecules. It means that, although the CLi_3−graphene structure is kinetically stable, there is still a thermodynamic driving force towards aggregation of CLi_3 molecules.

OLi molecules also bind strongly to a graphene substrate. Since an OLi molecule is smaller than a CLi_3 molecule, it is possible to quadruple the packing density of these molecules, as is shown in 6.3(b). OLi molecules preferentially bind to the substrate through the formation of an O−C bond. The calculated binding energy is 2.22 eV, which is comparable to the 2.26 eV/OLi aggregation energy of two OLi molecules into O_2Li_2. The O_2Li_2 molecule has a planar structure as shown in 6.2(c). This means that the OLi-graphene structure is close to being thermodynamically stable.
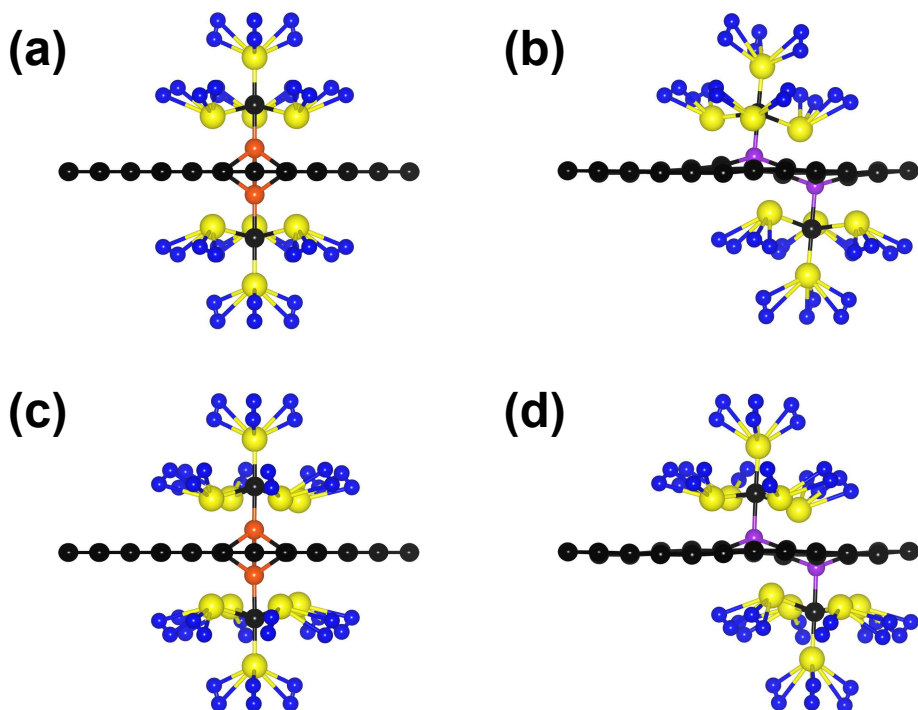
Figure 6.5: Side views of the fully hydrogenated structures of CLi_4 on (a) Be doped and (b) B doped graphene and of CLi_5 on (c) Be doped and (d) B doped graphene.

6.4.3   Adsorption on Doped Graphene

Another possible way of increasing the binding between polylithiated molecules and the substrate is by chemical modification of the graphene layer [51]. Introducing an impurity in graphene might for instance not only strengthen the interaction with CLi_n and OLi_m molecules, but could also maintain the positive charge on the Li atoms, and therefore the binding to H_2 molecules. Here we consider modification of graphene by atomic substitution of C by B or Be atoms. Previous studies have shown that B doping of graphene does not cause any major deformation of the graphene structure [52]. B doping concentrations of as high as 17 at. % can be achieved in thin films [53]. From experiment it has been suggested that the preferential geometry upon high B doping has two B atoms in para positions of an hexagonal ring in the graphene plane, as shown in 6.4(b). Indeed, the stability of this geometry has recently been confirmed by a theoretical study [54]. Here we consider such a double B substitution

Table 6.2: Binding energies (eV) between CLi_n and OLi_m molecules and (doped) graphene, and dimerization energies $(CLi_n)_2$, $(OLi_m)_2$.

	CLi_3	CLi_4	CLi_5	OLi	OLi_2	OLi_3	OLi_4
undoped	2.00	0.73		2.22	0.55		
Be doped	4.12	3.81	3.96	4.14	3.76	3.55	3.00
B doped	4.05	2.91	3.23	3.45	2.49	3.13	3.69
dimer	3.86	2.54	1.57	2.26	1.37	1.17	0.34

in our 4×4 graphene supercell, which gives a doping concentration of 6.25 at. %.

As an alternative to B doping we also consider substituting C with Be atoms. Replacing one C with a Be atom does not alter the planar structure of graphene. A single Be atom binds to a vacancy in the graphene lattice with a binding energy of 2.67 eV (with respect to the bulk Be metal). It is energetically advantageous however to replace a single C atom by a pair of Be atoms. The second Be atom then binds with a binding energy of 0.69 eV (again, with respect to bulk Be). The two Be atoms are then displaced above and below the graphene plane by 0.855 Å, as shown in 6.4(a), whereas the rest of graphene maintains its original structure. The Be atoms can act as pedestals that increase the distance between the graphene plane and the molecules we are going to attach, which could limit steric hindrance. All of the Be or B doped graphene structures have nonmagnetic ground states.

Modifying graphene by Be or B doping increases its interaction with polylithiated molecules. The molecules preferentially bind to the dopant atoms and form C,O−B,Be bonds. From the point of view of binding strength, there is no need to modify the molecules by extracting a Li atom before attaching them to the substrate. CLi_4 binds to a B or a Be site with binding energies of 2.91, 3.81 eV, respectively. The binding geometries are shown in 6.5. The binding between OLi_2 and B or Be doped graphene has an energy of 2.49, 3.76 eV , respectively. Since all these binding energies are well above the molecular dimerization energies one expects that aggregation of these molecules is now suppressed. Remarkably, doped graphene also forms strong bonds to other CLi_n and OLi_m molecules, including hypercoordinated ones such as CLi_5, OLi_3 and OLi_4, leading to similar binding geometries. The binding energies are given in 6.2 and examples of binding geometries are shown in 6.5.

With the polylithiated molecules strongly bonded to (doped) graphene we now study the hydrogenation properties of these systems. For CLi_3 and OLi bonded to undoped graphene we find that each of the Li atoms in the molecules above and

Table 6.3: Average hydrogen binding energies $E_b^{H_2}$ (eV/H_2), number of hydrogen molecules #H_2 bonded per CLi_n or OLi_m species, and gravimetric hydrogen densities of polylithiated molecules bonded to (doped) graphene.

	undoped			Be doped			B doped		
	$E_b^{H_2}$	#H_2	wt.% H_2	$E_b^{H_2}$	#H_2	wt.% H_2	$E_b^{H_2}$	#H_2	wt.% H_2
CLi_3	0.10	9	7.46	0.15	7	5.83	0.11	8	6.72
CLi_4				0.09	9	7.17	0.09	9	7.29
CLi_5				0.08	11	8.40	0.07	11	8.53
OLi	0.12	3	7.85	0.23	3	2.70	0.10	3	2.75
OLi_2				0.10	6	5.10	0.09	6	5.19
OLi_3				0.12	6	4.96	0.10	6	5.04
OLi_4				0.08	9	7.06	0.06	9	7.18

below the graphene plane can bind three H_2 molecules, see 6.3. The average hydrogen binding energy is 0.10 and 0.12 eV, respectively, which is comparable to that in free CLi_4 and OLi_2 molecules, compare 6.1. The resulting geometries are given in 6.3. The gravimetric densities in the CLi_3- and OLi-graphene systems are 7.46 and 7.85 wt.% H_2, respectively.

As discussed above, doping of graphene with Be or B increases the binding of polylithiated molecules to the substrate. The effect of doping on the binding energy between hydrogen and these molecules is small in most cases, as can be observed in 6.3. Only for H_2 on CLi_3 and OLi bonded to Be doped graphene the binding energy is significantly increased. The distance between the hydrogen molecules and the graphene plane is larger in these systems, as compared to the other cases. The gravimetric hydrogen density in the doped graphene systems is determined by the concentration of dopant atoms, since the polylithiated molecules are bonded to these atoms, as well as by the number of hydrogen molecules bonded to a single polylithiated molecule.

The latter is foremost determined by steric hindrance. A Li atom that is close to the graphene plane or to other Li atoms can in general capture only one or two H_2 molecules, whereas the ones that are further away from the plane and other Li atoms can bind three H_2 molecules. This is illustrated in 6.5. We have fixed the doping concentration of graphene. In particular for the OLi_m systems one can still increase the doping concentration without introducing too much steric hindrance, which would increase the gravimetric density substantially.

Hydrogen binding energies decrease slightly for hypercoordinated polylithiated molecules, i.e. CLi_n, $n > 3$ and OLi_m, $m > 1$. 6.5 shows that this leads to a trade-off between hydrogen binding energy and gravimetric density. Nevertheless it is clear that there are several possible systems and structures that attain a gravimetric density higher than 5% H_2 with H_2 binding energies in excess of 0.1 eV.

6.5   Conclusions

In conclusion, we have shown by means of first-principles DFT calculations that polylithiated molecules can be used as versatile building blocks for hydrogen storage materials. $Li-C$ and $Li-O$ bonds are strongly polar and the partially charged Li atoms can attract up to three to five H_2 molecules with an average binding energy in the range 0.10-0.15 eV. CLi_4 and OLi_2 molecules can then bind 12 and 10 hydrogen molecules, respectively, giving very high gravimetric densities of 37.8 and 40.3 weight % H_2. Binding polylithiated molecules to carbon nanostructures such as graphene can be used to immobilize them. In particular doping graphene with B or Be increases the binding energy. Although there is a trade-off between the size of the H_2 adsorption energy and its gravimetric density in these systems, densities in the range 5-8.5 wt.% H_2 can be reached without seriously decreasing the adsorption energy.

Acknowledgments

Supplementary Info

Optimized structures of free-standing (hydrogenated) polylithiated molecules and of (hydrogenated) polylithiated molecules adsorbed on doped graphene are supplied in CIF (Crystallographic Information File) format. This information is available free of charge via the Internet at http://pubs.acs.org.

Bibliography

[1] S. Pacala and R. Socolow, Science **305**, 968 (2004).

[2] See the special issue *Toward a Hydrogen Economy*, by R. Coontz and B. Hanson, Science **305**, 957 (2004).

[3] L. Schlapbach and A. Züttel, Nature **414**, 353 (2001).

[4] S. Patchkovskii *et al.*, Proc. Natl. Acad. Sci. U.S.A. **102**, 10439 (2005).

[5] S. K. Bhatia and A. L. Myers, Langmuir **22**, 1688 (2006).

[6] B. Panella, M. Hirscher, and S. Roth, Carbon **43**, 2209 (2005).

[7] O. V. Pupysheva, A. A. Farajian, and B. I. Yakobson, Nano Lett. **8**, 767 (2008).

[8] J. Niu, B. K. Rao, and P. Jena, Phys. Rev. Lett. **68**, 2277 (1992).

[9] L. Gagliardi and P. Pyykkö, J. Am. Chem. Soc. **126**, 15014 (2004).

[10] E. Durgun, S. Ciraci, W. Zhou, and T. Yildirim, Phys. Rev. Lett. **97**, 226102 (2006).

[11] R. C. Lochan and M. Head-Gordon, Phys. Chem. Chem. Phys. **8**, 1357 (2006).

[12] K. R. S. Chandrakumar and S. K. Ghosh, Nano Lett. **8**, 13 (2008).

[13] P. Chen, X. Wu, J. Lin, and K. L. Tan, Science **285**, 91 (1999).

[14] Z. Zhou, X. Gao, J. Yan, D. Song, and M. Morinaga, Carbon **42**, 2677 (2004).

[15] W. Q. Deng, X. Xu, and W. A. Goddard, Phys. Rev. Lett. **92**, 166103 (2004).

[16] O. Maresca, R. J. M. Pellenq, F. Marinelli, and J. Conard, J. Chem. Phys. **121**, 12548 (2004).

[17] Z. H. Zhu, G. Q. Lu, and S. C. Smith, Carbon **42**, 2509 (2004).

[18] I. Cabria, M. J. López, and J. A. Alonso, J. Chem. Phys. **123**, 204721 (2005).

[19] Y. Zhang, L. G. Scanlon, M. A. Rottmayer, and P. B. Balbuena, J. Phys. Chem. B **110**, 22532 (2006).

[20] Q. Sun, P. Jena, Q. Wang, and M. Marquez, J. Am. Chem. Soc. **128**, 9741 (2006).

[21] B. Fang, H. Zhou, and I. Honma, Appl. Phys. Lett. **89**, 023102 (2006).

[22] J. H. Cho and C. R. Park, Catal. Today **120**, 407 (2007).

[23] S. Han and W. Goddard III, J. Am. Chem. Soc. **129**, 8422 (2007).

[24] A. Blomqvist, C. M. Araujo, P. Srepusharawoot, and R. Ahuja, Proc. Natl. Acad. Sci. U.S.A. **104**, 20173 (2007).

[25] L. Chen, Y. Zhang, N. Koratkar, P. Jena, and S. K. Nayak, Phys. Rev. B **77**, 33405 (2008).

[26] Y. Li and R. T. Yang, J. Phys. Chem. C **112**, 19268 (2008).

[27] Q. Sun, Q. Wang, and P. Jena, Appl. Phys. Lett. **94**, 013111 (2009).

[28] C. H. Wu, H. Kudo, and H. R. Ihle, J. Chem. Phys. **70**, 1815 (1979).

[29] P. v. R. Schleyer, E. U. Wuerthwein, and J. A. Pople, J. Am. Chem. Soc. **104**, 5839 (1982).

[30] P. v. R. Schleyer, E. U. Wuerthwein, E. Kaufmann, T. Clark, and J. A. Pople, J. Am. Chem. Soc. **105**, 5930 (1983).

[31] H. Kudo, Nature **355**, 432 (1992).

[32] P. v. R. Schleyer and J. Kapp, Chem. Phys. Lett. **255**, 363 (1996).

[33] P. Lievens *et al.*, Eur. Phys. J. D **9**, 289 (1999).

[34] E. D. Jemmis *et al.*, J. Am. Chem. Soc. **104**, 4275 (1982).

[35] J. Ivanic and C. J. Marsden, J. Am. Chem. Soc. **115**, 7503 (1993).

[36] H. Kudo and C. H. Wu, J. Nucl. Mater. **201**, 261 (1993).

[37] R. Ponec *et al.*, J. Phys. Chem. A **106**, 1019 (2002).

[38] W. Zhizhong, Z. Xiange, and T. Auchin, J. Mol. Struct. **453**, 225 (1998).

[39] J. P. Perdew *et al.*, Phys. Rev. B **46**, 6671 (1992).

[40] P. E. Blöchl, Phys. Rev. B **50**, 17953 (1994).

[41] G. Kresse and D. Joubert, Phys. Rev. B **59**, 1758 (1999).

[42] G. Kresse and J. Hafner, Phys. Rev. B **47**, 558 (1993).

[43] G. Kresse and J. Furthmüller, Phys. Rev. B **54**, 11169 (1996).

[44] P. E. Blöchl, O. Jepsen, and O. K. Andersen, Phys. Rev. B **49**, 16223 (1994).

[45] K. Momma and F. Izumi, J. Appl. Crystallogr. **41**, 653 (2008).

[46] J. P. Perdew, K. Burke, and M. Ernzerhof, Phys. Rev. Lett. **77**, 3865 (1996).

[47] J. P. Perdew, K. Burke, and M. Ernzerhof, Phys. Rev. Lett. **78**, 1396 (1997).

[48] G. Henkelman, A. Arnaldsson, and H. Jónsson, Comput. Mater. Sci. **36**, 354 (2006).

[49] J. Ivanic and C. J. Marsden, Organometallics **13**, 5141 (1994).

[50] A. M. Sapse and P. v. R. Schleyer, *Lithium Chemistry: A Theoretical and Experimental Overview* (Wiley-IEEE, 1995).

[51] D. W. Boukhvalov and M. I. Katsnelson, Nano Lett. **8**, 4373 (2008).

[52] M. Endo, T. Hayashi, S. Hong, T. Enoki, and M. S. Dresselhaus, J. Appl. Phys. **90**, 5670 (2001).

[53] C. T. Hach, L. E. Jones, C. Crossland, and P. A. Thrower, Carbon **37**, 221 (1999).

[54] R. H. Miwa, T. B. Martins, and A. Fazzio, Nanotechnology **19**, 155708 (2008).

Chapter 7

DFT study of planar boron sheets: A new template for hydrogen storage

7.1 Abstract

We study the hydrogen storage properties of planar boron sheets and compare them to those of graphene. The binding of molecular hydrogen to the boron sheet (0.05 eV) is stronger than that to graphene. We find that dispersion of alkali metal (AM = Li, Na, and K) atoms onto the boron sheet markedly increases hydrogen binding energies and storage capacities. The unique structure of the boron sheet presents a template for creating a stable lattice of strongly bonded metal atoms with a large nearest neighbor distance. In contrast, AM atoms dispersed on graphene tend to cluster to form a bulk metal. In particular the boron-Li system is found to be a good candidate for hydrogen storage purposes. In the fully loaded case this compound can contain up to 10.7 wt % molecular hydrogen with an average binding energy of 0.15 eV/H_2.

7.2 Introduction

Hydrogen is an abundant, clean, and renewable energy carrier [1]. An important barrier preventing the large scale use of hydrogen is storing it densely and safely un-

der moderate conditions [2]. Also, fast loading and unloading of the storage system is still a challenge. Storage of hydrogen in molecular form may be more beneficial than storage of atomic hydrogen in chemical hydrides. Complex metal hydrides, for instance, are often either too stable or too unstable [3, 4] and require substantial doping to tune their stability [5, 6]. Moreover, the formation and decomposition of chemical hydrides typically involve complicated solid-state chemical reactions, which hamper the kinetics of hydrogen loading and unloading. In contrast, materials that physisorb molecular hydrogen, such as graphene, carbon nanotubes and fullerenes, clathrates, zeolites, and metal organic frameworks (MOFs), are capable of achieving fast hydrogen kinetics. The binding energy of hydrogen to these host materials is however small, which leads to unfavorable operating conditions of very low temperatures or high hydrogen pressures [7].

Recent studies show that metal doping enhances the strength of binding between hydrogen molecules and physisorption materials [8, 9]. An ideal metal dopant should strongly bind to the host material, and it should bind hydrogen molecules effectively. For instance, for storage of molecular hydrogen at 30 bar under ambient temperature, and delivery at 1.5 bar, the optimum adsorption enthalpy needs to be 0.15 eV/H_2 [7]. Upon deposition, the geometrical positioning of metal atoms over the substrate is also important, since the number of H_2 molecules per dopant site should be maximized. To prevent steric hindrance, this usually means that the dopant atoms need to be far apart. Therefore, the material should resist the clustering of metal atoms. At least the binding energy of a metal atom to the substrate should then be larger than the cohesive energy of the bulk metal. This is extremely difficult to attain with transition metal dopants, since the cohesive energies of bulk transition metals are high. Alkali metals have much lower cohesive energies and are therefore more suitable as dopants.

Recent studies addressed the alkali metal doping of physisorption materials such as graphene [10–12], fullerene [13–15], carbon nanotubes [16–19], and MOFs [20–23]. Hydrogen molecules are trapped around the dispersed doping metal atoms through electrostatic and polarization interactions [24]. In addition to increasing the binding strengths to hydrogen, alkali metal doping also increases the effective surface area available for absorption in some cases. Hydrogen adsorption then goes beyond a single monolayer, increasing the volumetric and gravimetric hydrogen densities accordingly.

In order to obtain a sufficiently high gravimetric density, not only the alkali metals need to be lightweight, but also the substrates need to be lightweight materials. In the past decade, carbon nanostructures of various dimensions have been studied extensively both theoretically and experimentally for various applications, including as substrates for hydrogen storage. The recent realization of the structurally most
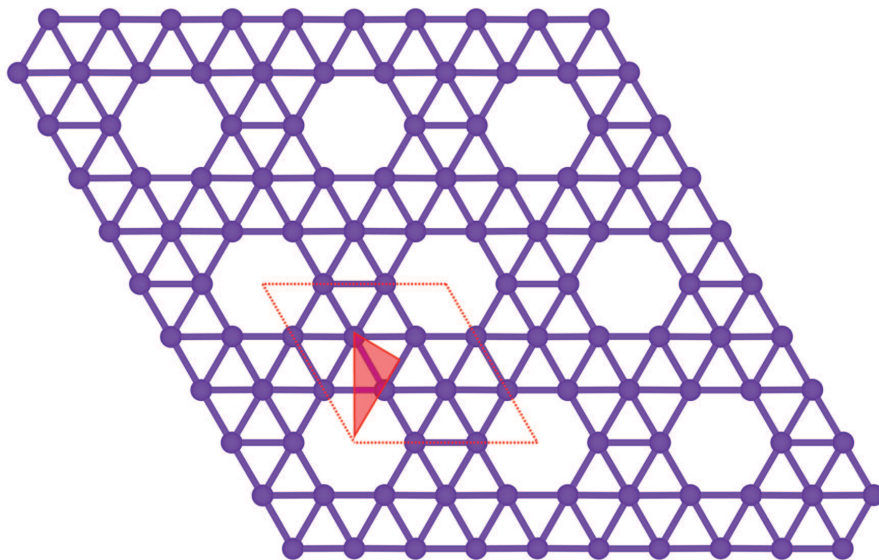
Figure 7.1: The most stable form of the boron sheet. The primitive cell is indicated by dotted red lines. It contains eight boron atoms, shown as purple spheres. The irreducible part of the Wigner−Seitz cell (WSC) is indicated by a triangle.

simple carbon network, graphene, has attracted a great deal of interest [25, 26]. The lightest element that can form extensive covalently bonded structures is in fact boron. Boron, having one electron less than carbon, forms icosahedral clusters,[27, 28] and has long been thought not to form two-dimensional (2-D) structures similar to graphene.

However, it has very recently been shown that the stability of planar 2-D hexagonal boron sheets is enhanced markedly by inserting additional boron atoms in the centers of hexagons of the honeycomb structure; see 7.1 [29–32]. These additional boron atoms modify the electronic structure of the boron lattice. 2-D hexagonal boron is an electron deficient system with part of the sp^2 bonding states unoccupied. The electrons provided by the additional boron atoms occupy these states, increasing the stability [29]. These new 2-D boron structures also provide insight into the unusual stability of other boron-only structures with different dimensions, such as fullerenes [33–35], nanotubes [32, 36, 37], and nanoribbons [38].

Here, we investigate the hydrogen storage properties of the boron sheet structure that is identified as the most stable form, the so-called α-structure.[29] We first

study the interaction of H_2 molecules with this boron sheet. Next, the dispersion of alkali metal (AM = Li, Na, and K) atoms onto the boron sheet is considered. We study the binding and the mobility of these AM atoms on the boron sheet and the hydrogenation energies of these systems. All of the three AMs are found to bind strongly to the boron sheet. Moreover, the unique structure of the boron sheet allows for a stable lattice of AM atoms with a large nearest neighbor AM−AM distance, which consequently creates space for hydrogenation. The AM atoms accumulate a net positive charge, which not only stabilizes this structure but also strengthens the binding to hydrogen molecules. All three AMs lead to a higher hydrogen binding energy, but Li is by far the best doping element.

7.3   Computational Details

We perform first-principles calculations based on density functional theory (DFT), using the Vienna *ab initio* simulation package (VASP) [39, 40]. The generalized gradient approximation (GGA) in the form of the PW91 functional is used to approximate exchange and correlation [41]. Although dispersion (van der Waals) interactions are not captured by this functional, it should give a good description of chemical bonding and of electrostatic interactions, which are the most prominent interactions in alkali doped systems; see also ref [12]. Binding energies of H_2 molecules to similar systems obtained with the PW91 functional are within ~ 20 meV/H_2 of those obtained with the PBE functional [12]. Therefore, we only give the PW91 results in the following.

The basis set is constructed according to the projector augmented wave (PAW) method [42, 43]. The following electrons are treated as valence: H 1s, B 2s2p, Li 1s2s, Na 3s2p, and K 4s3p. A cutoff energy of 400 eV is used for the plane-wave basis. Brillouin zones (BZs) of all structures are integrated with k-point spacings of ~ 0.01 Å^{-1} [44]. For instance, the BZ corresponding to the unit cell shown in Figure 7.1 is then integrated using a 12×12 regular grid. Gaussian smearing is used with a smearing width of 0.01 eV. Periodic images of the sheet along the surface normal are well separated by a distance of ~ 20 Å, so that the interactions between these images are negligible. Atomic and geometric relaxations are carried out by employing the conjugated-gradient (CG) algorithm. All atomic positions and cell parameters are relaxed. The relaxations are assumed to be complete when the total force remaining on each atom and the stress tensor components acting on the cells are less than 0.02 eV/Å and 2.5 kbar, respectively. Total energies then are converged to within 1 meV/unit cell at least. The tetrahedron method is then used to calculate the total energies of the relaxed structures [45].
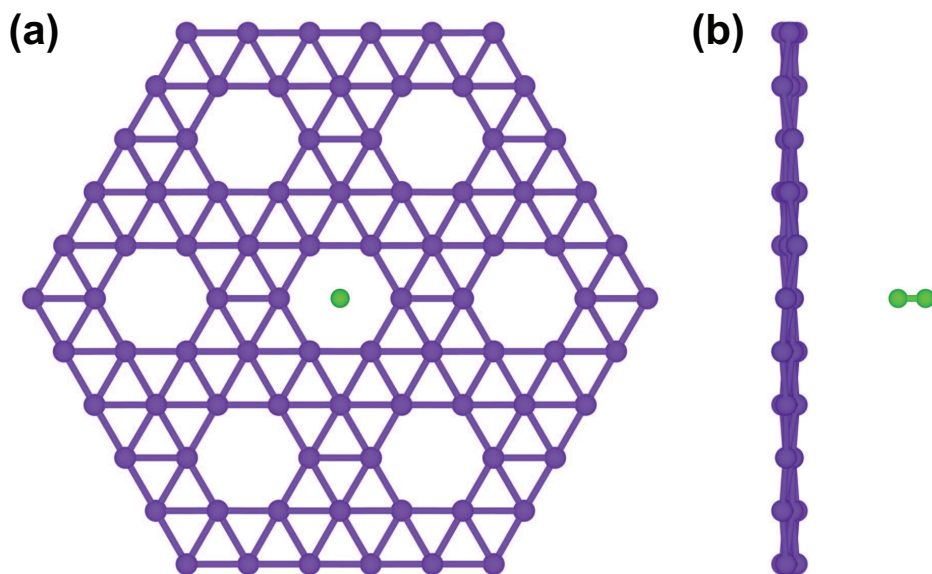
Figure 7.2: The most stable geometry of H_2 adsorbed on a boron sheet shown in (a) top, and (b) side views. The molecule is positioned over the center of an empty boron hexagon with its axis orthogonal to the boron plane.

7.4 Results and Discussion

7.4.1 Hydrogen Adsorption on Boron Sheets

The most stable structure of a boron sheet is shown in 7.1. It is a graphene-like structure, where two-thirds of the hexagon centers are occupied by additional boron atoms. The primitive cell of the sheet then contains eight boron atoms. It leads to a unique planar structure with a lattice of empty hexagons spaced at a distance of 5.06 Å of one another.

To model the interaction of hydrogen molecules with the boron sheet, we use a 2×2 supercell. The distance between hydrogen molecules in neighboring cells is then 10.12 Å, which is sufficiently large to neglect the interaction between these molecules. We consider a number of possible positions of the H_2 molecule on the boron sheet. Since the latter contains a lot of symmetry, it is only necessary to consider the irreducible part of the Wigner−Seitz cell (WSC), which is indicated in 7.1. We scan the edges of the irreducible WSC by placing a H_2 molecule at several positions, which are separated by 0.8 Å, as measured from the H−H bond centers.

At each of these points, we consider three different molecular orientations. In two of these orientations, the H_2 molecular axis is parallel to the boron plane. The two orientations differ by an in-plane angle of $30°$. In the third configuration, the H_2 molecular axis is perpendicular to the boron plane. The H−H bond centers are placed at a distance of at least 2 Å from the boron sheet.

In total, we have constructed a set of 36 distinct initial geometries. All of the structures in this set are then subjected to relaxation without any symmetry constraints. These calculations reveal that H_2 molecules tend to occupy positions over the open boron hexagons. The minimum energy configuration is the one in which the molecule is over the center of an open hexagon with its axis perpendicular to the boron plane (7.2). The distance between the boron plane and the center of the molecule is 3.27 Å, and the calculated value of the binding energy is 47 meV. The energy differences between different orientations of the H_2 molecule are generally small. A H_2 molecule at this site with its axis parallel to the boron plane is only ~ 5 meV higher in energy. The potential energy surface obtained by varying the position of the H_2 molecule over the plane has a corrugation of 61 meV.

Interestingly, the interaction of H_2 with the boron sheet shows similarities to its interaction with graphene. We consider a graphene supercell similar to that of boron, which has of course the typical graphene structure without atoms in the centers of the hexagons. The calculated binding energy of H_2 to graphene is then 25 meV. Likewise, the geometry of the adsorbed H_2 molecule is very similar to that on the boron sheet, and the distance to the graphene plane is 3.24 Å. Our results on the graphene−H_2 system are in accordance with earlier studies [46–48]. We note that, although the binding of H_2 to the boron sheet is slightly stronger than that to graphene, it is still too weak for a practical hydrogen storage application.

7.4.2   Doping Boron Sheets with Alkali Metals

Next, we consider deposition of AM atoms onto the boron sheet, with AM = Li, Na, or K. To have a stable material at a reasonable temperature, it is essential that the metals strongly bind to the boron template. In addition, meaningful hydrogen gravimetric densities can be reached only if the AM atoms are separated far enough from each other so that each atom has sufficient space to bind hydrogen molecules. Placing a single AM atom in the unit cell shown in 7.1 leads to a lattice of AM atoms with a cell parameter of 5.06 Å. We vary the position of the AM atom on the boron sheet and relax all structures, as discussed in the previous section. The optimal position of all three lightweight AMs turns out to be over the center of the empty boron hexagon, as in 7.3. Upon relaxing, the unit cell parameters of the doped
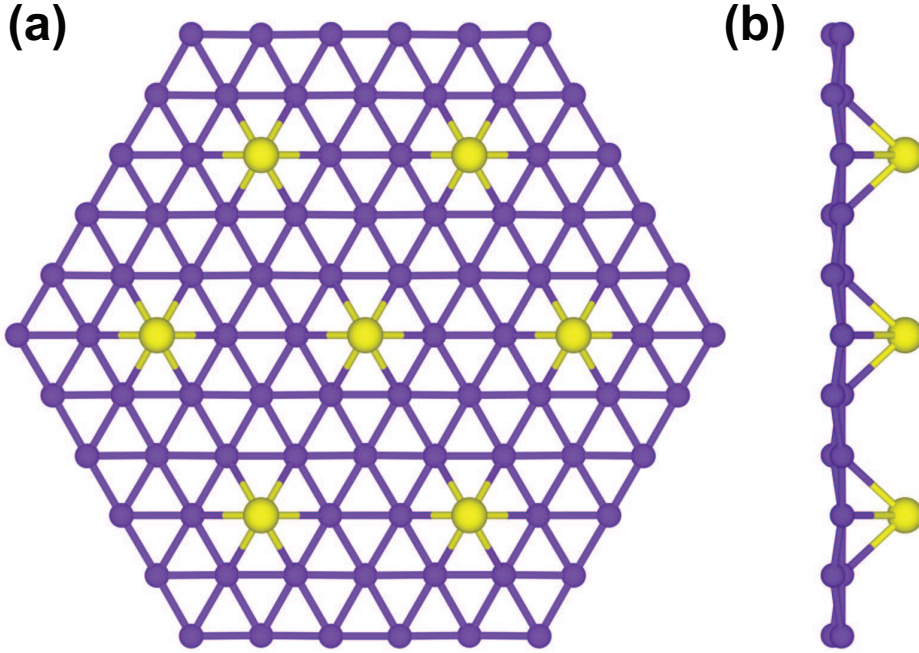
Figure 7.3: Optimized structure of a boron sheet doped with Li atoms (yellow spheres), shown from (a) the top and (b) the side. Boron sheets doped with other lightweight AMs have a similar geometry.

systems do not change noticeably. The optimized cell parameters are 5.08, 5.07, and 5.07 Å for the Li, Na, and K doped boron sheet, respectively.

The binding energies of the AM atoms to the boron sheet are calculated according to

$$E_{\mathrm{b}} = E_{\mathrm{AMbulk}} + E_{\mathrm{boron}} - E_{\mathrm{boronAM}}, \qquad (7.1)$$

where E_{AMbulk} is the total energy per atom of the AM bulk metal, E_{boronAM} is the total energy per AM atom of the AM doped boron sheet, and E_{boron} is the corresponding total energy of the boron sheet. The results are shown in 7.1. For comparison, the binding energies E_{at}, calculated from eq 7.1 by replacing E_{AMbulk} with the energy of an isolated AM atom, are also given in this table. The numbers show that all three systems are thermodynamically stable with respect to separation into bulk metal and a boron sheet.

The equilibrium distance between the AM atoms and the boron plane, listed in 7.1, shows an increase going from Li to K, as might be expected. Electrostatic interactions

Table 7.1: Calculated Binding Energies of Alkali Metals on a Boron Sheet (7.3) with Respect to Bulk Metal (E_b), Isolated Atoms (E_{at}), Equilibrium Distances to the Boron Plane (d), and Bader Charges on the Alkali Atoms (Q)

AM	E_b(eV)	E_{at}(eV)	d(Å)	Q (e)
Li	0.27	1.89	1.54	+0.85
Na	0.02	1.11	2.26	+0.60
K	0.34	1.21	2.75	+0.47

are dominant in binding hydrogen molecules to the AM atoms [12]. Therefore, it is useful to make a Bader charge analysis to determine the effective charges on the AMs [49]. The Bader charges decrease going from Li to K, which at first sight may seem surprising as the electronegativity of the AMs decreases along this series. However, comparing the nearest neighbor distances between the metal atoms on the boron surface with those in the bulk metals, one observes that the former are larger by 70, 40, and 10 % for Li, Na, and K, respectively. This means that the Li atoms on the boron sheet are relatively isolated, but the K atoms are still in relatively close contact. In this configuration, a Li atom is bonded to the boron sheet and the binding has a large ionic contribution, whereas a K atom is bonded to the boron sheet and to other K atoms with a mix of ionic and metallic bonding. Clearly, the binding of a Na atom is intermediate between these two situations.

In principle, one might increase the distance between the K atoms by decreasing their concentration on the boron sheet. However, K is already the heaviest element of the AM series considered here, and a reduction of their concentration increases the number of boron atoms per metal atom. This would seriously decrease the gravimetric hydrogen density, since the amount of hydrogen adsorbed depends on the metal atoms only. In conclusion, since Li is the lightest element, binds strongly to the boron sheet, and discharges almost completely upon deposition, it is the best candidate as a dopant for hydrogen storage purposes.

Since the Li atoms on the boron carry an effective positive charge, one may expect a net repulsion between these atoms. We consider the binding energy E_b, eq 7.1, and Bader charge Q as a function of the Li concentration. The results are given in 7.2. In the concentration we have considered so far, the Li−Li nearest neighbor distance is 5.08 Å. Doubling the boron surface unit cell in each direction and occupying only one empty hexagon by a Li atom decreases the concentration by a factor of 4 and decreases the Li−Li nearest neighbor distance by a factor of 2. Occupying not only

Table 7.2: Calculated Binding Energies with Respect to Bulk Metal (E_b) and Bader Charges (Q) of Li on a Boron Sheet at Various Concentrations, Represented by the Nearest Neighbor Metal−Metal Distance d_{nn}.

d_{nn}(Å)	E_b(eV)	Q (e)
10.16	0.45	+0.88
5.08	0.27	+0.85
2.93	0.16	+0.75

all empty, but also all filled boron hexagons increases the Li concentration by a factor of 3. The Li−Li nearest neighbor distance is then multiplied $1/\sqrt{(3)}$. The binding energy indeed decreases with increasing concentration, confirming the net repulsion between the Li atoms. There is a corresponding slight decrease of the Bader charge on the Li atoms. Note however that, at all concentrations studied, the system is stable against phase separation into a sheet carrying a lower concentration of Li and bulk Li. The Li concentration can therefore be controlled by the amount of Li dispersed on the boron sheet.

It is interesting to compare the Li doping of the boron sheet to that of a similar system, namely, Li doping of graphene, which has been proposed as a suitable hydrogen storage system [10, 11]. We use a similar unit cell as for the boron sheet, containing six carbon atoms and three hexagons, one of which contains a Li atom. After relaxation, the lattice parameter of the graphene−Li cell is 4.28 Å, whereas the boron-Li cell parameter is slightly larger (5.08 Å). We find that the binding of Li atoms to graphene is considerably weaker than the binding to the boron sheet. On graphene, the binding energy $E_b = -0.61$ eV. Obviously, a negative value of the binding energy indicates that this system is thermodynamically unstable with respect to bulk Li and graphene, in contrast to the boron-Li system, cf. 7.1.

Moreover, a Bader analysis carried out on the graphene-Li system reveals that only 0.64e is removed from Li atoms after deposition, which is significantly smaller than the case of the boron−Li system. These results suggest that the boron sheet is a more promising candidate for lightweight AM doping than pure graphene.

7.4.3 Mobility of Alkali Metal Atoms

The stability of a material such as a doped boron or graphene sheet also depends on the mobility of the AM atoms on the sheet. Within the transition state theory model, the most important parameter determining the mobility is the energy barrier
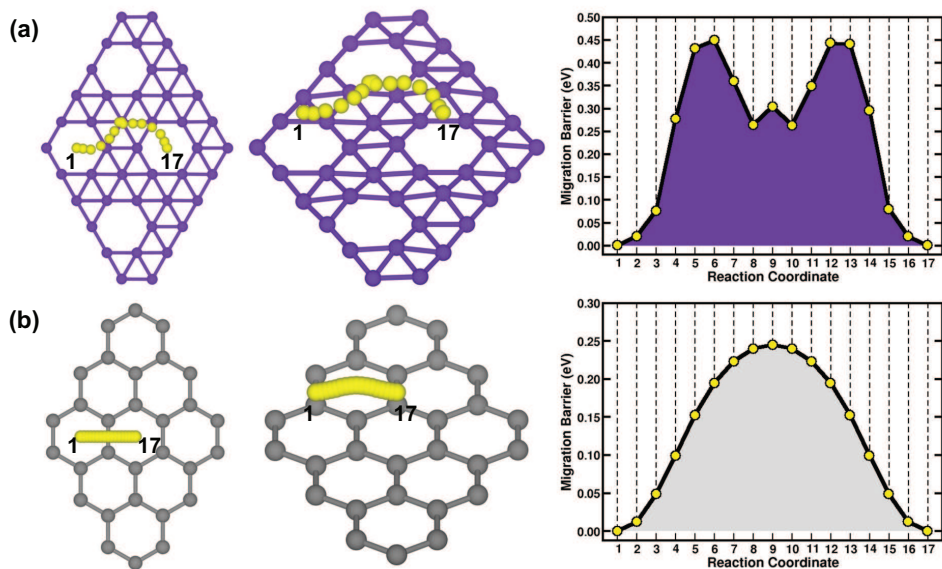
Figure 7.4: Diffusion of a Li atom over a (a) boron sheet and (b) graphene. The lowest energy diffusion paths are shown in top and perspective views. Calculated energy profiles along the paths are plotted on the right-hand side. The yellow dots in the plot correspond to the positions shown on the left-hand side. The diffusion barriers are 0.45 and 0.25 eV on the boron and graphene, respectively.

for diffusion. We determine the diffusion path of a single Li atom on the boron sheet using the nudged elastic band method [50–52]. The calculations are carried out using a 2×2 supercell with 32 boron atoms, where one empty hexagon is occupied by a Li atom. A string of 17 images is chosen to model the diffusion path between two empty hexagons, as shown in 7.4a. Positions over the centers of the empty hexagons represent absolute energy minima, and positions over the boron atoms at the centers of the other hexagons represent secondary adsorption minima. An optimal path runs over B atoms, and along B−B bonds, as shown in 7.4a, with maxima over B−B bond centers. The calculated diffusion barrier is 0.45 eV. The lowest energy path for diffusion between two energy minima corresponding to empty hexagons proceeds via a secondary minimum over a filled hexagon, giving rise to a curved path. The simpler direct path between two empty hexagons involves an energy barrier of 0.55 eV and is therefore less likely.

We can compare this to diffusion of a Li atom over graphene. Positions over the

Table 7.3: Calculated Binding Energies of Alkali Metals on a Boron Sheet Where Both Sides of the Sheet are Functionalized (7.3), with Respect to Bulk Metal (E_b) and Isolated Atoms (E_{at}), Equilibrium Distances to the Boron Plane (d), Bader Charges on the Alkali Atoms (Q), Hydrogen Binding Energies (E_{H_2}), and Gravimetric Hydrogen densities of the B_8AM_2 Systems.

AM	E_b(eV)	E_{at}(eV)	d(Å)	$Q(e)$	E_{H_2}(eV)	H_2 (wt %)
Li	0.18	1.80	1.62	+0.82	$0.35 - 0.15$	10.75
Na	0.02	1.11	2.28	+0.60	$0.13 - 0.07$	8.36
K	0.35	1.22	2.75	+0.47	0.06	2.39

centers of the carbon hexagons represent the absolute energy minima. A Li atom diffuses over a C−C bond following a simple path, with a maximum over a C−C bond center, as shown in 7.4b. The calculated diffusion barrier is $E_d = 0.25$ eV. Consequently, Li atoms on graphene are quite mobile. Using an Arrhenius expression for the jump rate $\nu = \nu_0 \exp[E_d/kT]$ with a typical attempt frequency of $\nu_0 \approx 10^{12}$ Hz, one obtains $\nu \approx 10^8$ Hz at room temperature and $\nu \approx 1$ Hz at $T = 105$ K. Because of their negative binding energy with respect to bulk Li, as discussed in the previous section, there is a thermodynamic driving force for Li atoms to cluster, which would seriously hamper the use of doped graphene as a hydrogen storage material [10, 11]. It is, however, possible to use graphene as a template for polylithiated molecules to create a stable storage material [12].

The diffusion barrier, $E_d = 0.45$ eV, for Li atoms on the boron sheet is substantially larger than that on graphene. Using the same Arrhenius expression as above, a jump rate of $\nu \approx 1$ Hz is obtained at $T = 190$ K. At room temperature, individual Li atoms are still mobile ($\nu \approx 10^4$ Hz), but the formation bulk Li metal is thermodynamically unfavorable because of the high binding energy of the Li atoms on the boron sheet. The energy difference between the minimum energy sites of a Li atom (over the centers of empty boron hexagons) and the secondary minima is 0.3 eV. It means that at room temperature only the minimum energy sites are occupied. Since the Li atoms carry a substantial effective charge, there is in addition no driving force for clustering of metal atoms on the sheet. The minimum energy sites on the boron sheet form a regular lattice with a spacing of 5.08 Å between the lattice points, which forms the ideal template for creating a stable lattice of Li atoms.
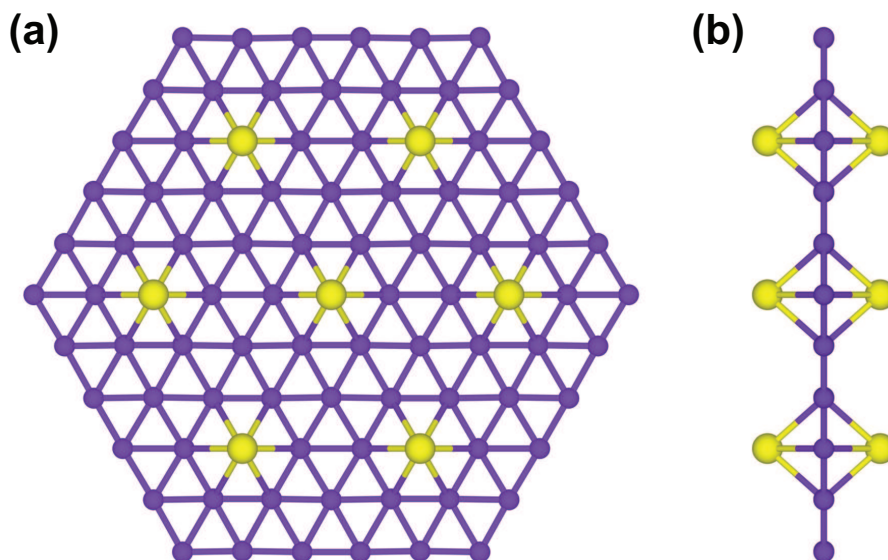
Figure 7.5: Optimized structure of a boron sheet doped with Li atoms on both sides, shown from (a) the top and (b) the side. Boron sheets doped with other lightweight AMs have a similar geometry.

7.4.4   Hydrogen Adsorption on Alkali Doped Boron Sheets

Starting from the AM lattice on the boron sheet, as discussed in the previous sections, we find in fact that both faces of the boron lattice can be functionalized with AMs, as depicted in 7.5. The chemical formula of the AM doped boron unit cells is then B_8AM_2 and the optimized lattice constants are 5.10, 5.08, and 5.08 Å for the AM = Li, Na, and K, respectively. The optimized structures have mirror symmetry with respect to the boron plane. The binding energies of the AM atoms, their distances to the boron plane, and their Bader charges are given in 7.3. A comparison to the data of 7.1 demonstrates that there is very little interaction between the AM atoms located above and below the boron sheet. Our general observations for AM doping remain valid; i.e., also for the doubly functionalized boron sheet, we have a stable lattice of effectively charged AM atoms.

Electrostatic and polarization interactions contribute most to the binding between the AM atoms and hydrogen molecules [12]. One may therefore expect that the effective charges on the metal atoms after deposition onto the boron sheet determines the strength of the interaction between the host material and the hydrogen molecules.
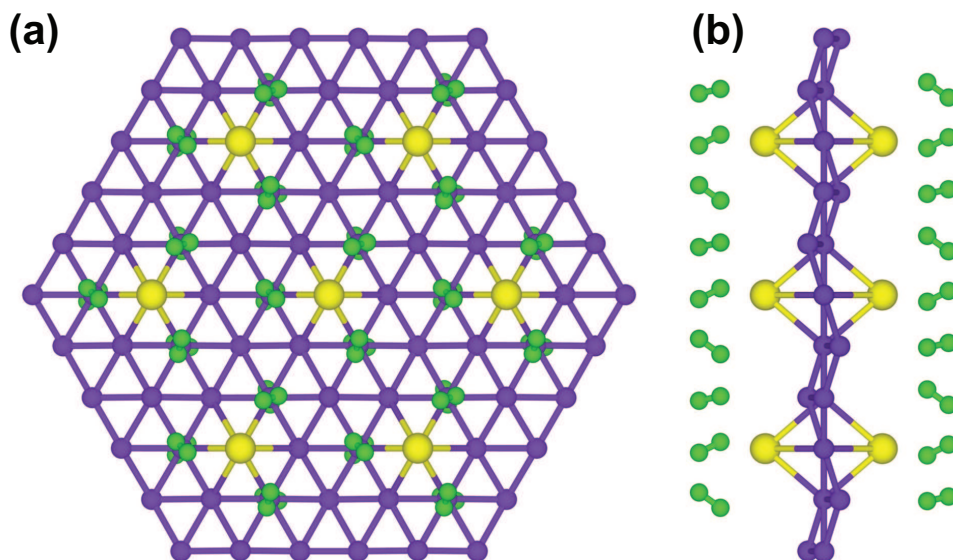
(a)

(b)

Figure 7.6: The optimized geometry of the Li doped boron sheet after full hydrogenation, shown from (a) the top and (b) the side. Three H_2 molecules surround each Li atom.

These charges decrease along the series Li, Na, and K, as shown by 7.3. The binding energies of hydrogen molecules to the AM doped boron sheet follow this trend. The first two H_2 molecules bind to B_8Li_2 with a binding energy of 0.35 eV/H_2 (one H_2 binds to the top Li, and one to the bottom Li). The corresponding numbers for Na and K are significantly smaller, i.e., 0.13 and 0.06 eV/H_2, respectively.

Each Li atom in this structure can capture up to three H_2 molecules, but the average binding energy then drops to 0.15 eV/H_2. In the fully loaded case, the B_8Li_2 compound then contains 10.7 wt % hydrogen, and the chemical formula of the unit cell is $B_8Li_2(H_2)_6$. The optimized geometry is shown in 7.6. The centers of all the H_2 molecules surrounding the Li atoms are located at an equivalent distance of 2.35 Å from the metal atoms. These results are in line with the interactions of H_2 molecules with isolated AM cations [14, 24]. The maximum number of H_2 molecules that can be gathered around a metal center is determined by the Coulomb interactions that develop between Li$-H_2$ and H_2-H_2, and by steric effects.

The B_8Na_2 system can also capture three H_2 molecules per metal. The average binding energy for the H_2 molecules then drops to 0.07 eV/H_2, which is still larger than the binding between a H_2 molecule and a bare boron sheet. In contrast, the
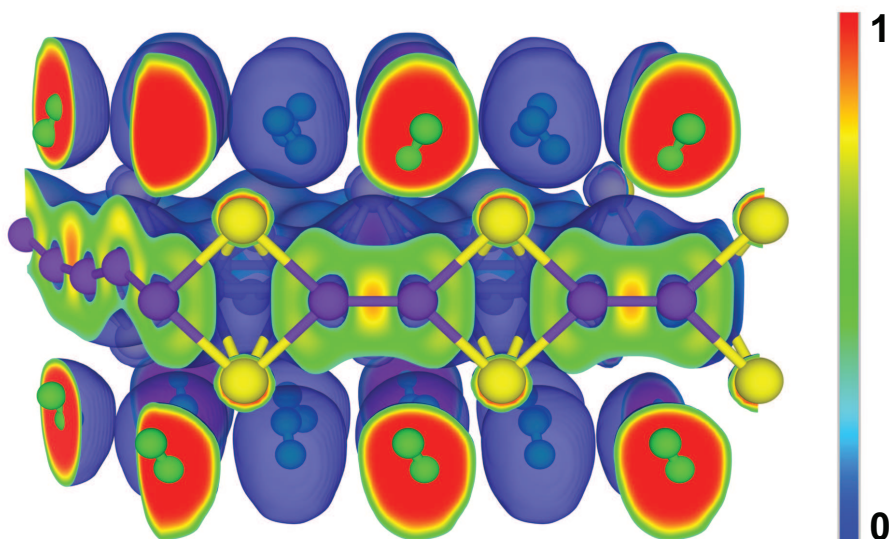
Figure 7.7: Electron localization function of the boron−Li system at its fully hydrogenated state. The electrons are localized at the H_2 molecules and around the boron sheet, where the bonding is covalent. The positively charged Li ions are depleted from electrons.

B_8K_2 system is capable of capturing only a single H_2 molecule per K atom with a low binding energy of 0.06 eV/H_2. It is clear that, if compared to the Li doped system, the higher electron densities on the Na and K atoms result in weaker interactions with H_2 molecules. The Li doped boron sheet is the best option for hydrogen storage.

It is interesting to note that the amount of charge on the Li atoms, as a consequence of their interaction with the boron lattice, stays almost constant during the consecutive addition of H_2 molecules. The H−H bonds of the adsorbed H_2 molecules are only elongated by ~ 1.5 % as compared to an isolated H_2 molecule, which illustrates that the interaction between H_2 molecules and the Li atoms is mostly electrostatic and not chemical bonding.

The calculated electron localization function for the $B_8Li_2(H_2)_6$ system is shown in 7.7. The Li atoms are depleted, consistent with our Bader analysis. Hydrogens stay in molecular form and are surrounded by their localized electron clouds. There is no direct indication of an orbital interaction between the Li atoms and the hydrogens. Moreover, the pattern of the covalent bonding within the boron lattice is not significantly altered by the Li atoms or the H_2 molecules.

7.5 Conclusions

We study the planar boron α-sheet as a physisorption template for hydrogen storage. Direct physisorption of H_2 on a boron sheet gives a binding energy of 0.05 eV. Alkali metal (AM) atoms can be dispersed on the boron sheet to increase the hydrogen binding energies. The boron sheet interacts strongly with AM atoms, and the doped systems are thermodynamically stable with respect to clustering of metal atoms. Moreover, the unique geometry of the boron plane provides a natural lattice for the metal atoms whose nearest neighbor distance can be tuned by varying their concentration. In particular, Li is found to be a promising doping element for hydrogen storage. The strong interaction between the boron sheet and the Li atoms results in an almost complete transfer of the Li valence electrons to the boron sheet. Electrostatic interactions between the well-exposed Li atoms and the H_2 molecules then lead to an average binding energy of 0.15 eV/H_2. The system physisorbs up to a maximum of 10.7 wt % hydrogen. In contrast, AM atoms dispersed on graphene are generally unstable with respect to the bulk metal, which suggests that AM doped nanostructures based upon boron are a much better starting point for hydrogen storage than their carbon based counterparts.

Acknowledgments

Bibliography

[1] See the special issue *Toward a Hydrogen Economy*, by R. Coontz and B. Hanson, Science **305**, 957 (2004).

[2] L. Schlapbach and A. Züttel, Nature **414**, 353 (2001).

[3] M. J. van Setten, G. A. de Wijs, V. A. Popa, and G. Brocks, Phys. Rev. B **72**, 073107 (2005).

[4] S. Er, D. Tiwari, G. A. de Wijs, and G. Brocks, Phys. Rev. B **79**, 024105 (2009).

[5] M. J. van Setten, G. A. de Wijs, and G. Brocks, Phys. Rev. B **76**, 075125 (2007).

[6] R. Gremaud *et al.*, Adv. Mater. **19**, 2813 (2007).

[7] S. K. Bhatia and A. L. Myers, Langmuir **22**, 1688 (2006).

[8] T. Yildirim and S. Ciraci, Phys. Rev. Lett. **94**, 175501 (2005).

[9] E. Durgun, S. Ciraci, and T. Yildirim, Phys. Rev. B **77**, 85405 (2008).

[10] W. Q. Deng, X. Xu, and W. A. Goddard, Phys. Rev. Lett. **92**, 166103 (2004).

[11] C. Ataca, E. Aktürk, S. Ciraci, and H. Ustunel, Appl. Phys. Lett. **93**, 043123 (2008).

[12] S. Er, G. A. de Wijs, and G. Brocks, J. Phys. Chem. C **113**, 8997 (2009).

[13] Q. Sun, P. Jena, Q. Wang, and M. Marquez, J. Am. Chem. Soc. **128**, 9741 (2006).

[14] K. R. S. Chandrakumar and S. K. Ghosh, Nano Lett. **8**, 13 (2008).

[15] Q. Sun, Q. Wang, and P. Jena, Appl. Phys. Lett. **94**, 013111 (2009).

[16] P. Chen, X. Wu, J. Lin, and K. L. Tan, Science **285**, 91 (1999).

[17] C. Liu *et al.*, Science **286**, 1127 (1999).

[18] R. Yang, Carbon **38**, 623 (2000).

[19] E. Lee, Y. Kim, Y. Jin, and K. Chang, Phys. Rev. B **66**, 73415 (2002).

[20] A. Blomqvist, C. M. Araujo, P. Srepusharawoot, and R. Ahuja, Proc. Natl. Acad. Sci. U.S.A. **104**, 20173 (2007).

[21] S. S. Han, W. Q. Deng, and W. A. Goddard, Angew. Chem., Int. Ed. **46**, 6289 (2007).

[22] A. Mavrandonakis, E. Tylianakis, A. K. Stubos, and G. E. Froudakis, J. Phys. Chem. C **112**, 7290 (2008).

[23] E. Klontzas, A. Mavrandonakis, E. Tylianakis, and G. Froudakis, Nano Lett. **8**, 1572 (2008).

[24] R. C. Lochan and M. Head-Gordon, Phys. Chem. Chem. Phys. **8**, 1357 (2006).

[25] K. S. Novoselov *et al.*, Science **306**, 666 (2004).

[26] A. Geim and A. MacDonald, Phys. Today **60**, 35 (2007).

[27] E. L. Muetterties, *The chemistry of boron and its compounds* (New York: John Wiley & Sons, Inc., 1967).

[28] H. Werheit, *Landolt-Börnstein: Numerical Data and Functional Relationships in Science and Technology - New Series* (Berlin: Springer, 2000).

[29] H. Tang and S. Ismail-Beigi, Phys. Rev. Lett. **99**, 115501 (2007).

[30] K. C. Lau and R. Pandey, J. Phys. Chem. C **111**, 2906 (2007).

[31] K. C. Lau and R. Pandey, J. Phys. Chem. B **112**, 10217 (2008).

[32] X. Yang, Y. Ding, and J. Ni, Phys. Rev. B **77**, 041402 (2008).

[33] D. L. Prasad and E. D. Jemmis, Phys. Rev. Lett. **100**, 165504 (2008).

[34] Q. B. Yan, X. L. Sheng, Q. R. Zheng, L. Z. Zhang, and G. Su, Phys. Rev. B **78**, 20 (2008).

[35] T. Baruah, M. R. Pederson, and R. R. Zope, Phys. Rev. B **78**, 045408 (2008).

[36] A. K. Singh, A. Sadrzadeh, and B. I. Yakobson, Nano Lett. **8**, 1314 (2008).

[37] K. C. Lau, R. Orlando, and R. Pandey, J. Phys.: Condens. Matter **20**, 125202 (2008).

[38] Y. Ding, X. Yang, and J. Ni, Appl. Phys. Lett. **93**, 043107 (2008).

[39] G. Kresse and J. Hafner, Phys. Rev. B **47**, 558 (1993).

[40] G. Kresse and J. Furthmüller, Phys. Rev. B **54**, 11169 (1996).

[41] J. P. Perdew *et al.*, Phys. Rev. B **46**, 6671 (1992).

[42] P. E. Blöchl, Phys. Rev. B **50**, 17953 (1994).

[43] G. Kresse and D. Joubert, Phys. Rev. B **59**, 1758 (1999).

[44] H. J. Monkhorst and J. D. Pack, Phys. Rev. B **13**, 5188 (1976).

[45] P. E. Blöchl, O. Jepsen, and O. K. Andersen, Phys. Rev. B **49**, 16223 (1994).

[46] T. Heine, L. Zhechkov, and G. Seifert, Phys. Chem. Chem. Phys. **6**, 980 (2004).

[47] D. Henwood and J. D. Carey, Phys. Rev. B **75**, 245413 (2007).

[48] N. Park, S. Hong, G. Kim, and S. H. Jhi, J. Am. Chem. Soc. **129**, 8999 (2007).

[49] G. Henkelman, A. Arnaldsson, and H. Jónsson, Comput. Mater. Sci. **36**, 354 (2006).

[50] H. Jónsson, G. Mills, and K. W. Jacobsen, *Nudged Elastic Band Method for Finding Minimum Energy Paths of Transitions, in Classical and Quantum Dynamics in Condensed Phase Simulations* (Singapore: World Scientific, 1998).

[51] G. Henkelman and H. Jónsson, J. Chem. Phys. **113**, 9978 (2000).

[52] D. Sheppard, R. Terrell, and G. Henkelman, J. Chem. Phys. **128**, 134106 (2008).

Chapter 8

Lightweight metal doping of metal-organic frameworks: Implications for hydrogen storage

8.1 Introduction

Metal organic frameworks (MOFs) are low density crystalline materials with exceptionally high porosity [1]. Recent advancements in MOF synthesis are promising their widespread usage as gas storage systems, particularly hydrogen [2–15]. Available MOF systems, however, are known to bind hydrogen molecules very weakly, therefore requiring massive operating pressures and cryogenic conditions. Recent theoretical studies on Li doped MOF systems report significant improvements on molecular hydrogen uptake capacities near ambient conditions [16–18]. In these studies, however, Li atoms are modeled to bind to the aromatic linker units. Here, we report that lightweight alkali metals (AM=Li, Na, and K) and alkaline earth metals (AEM=Be, Mg, and Ca) favorably bind to the oxide connector units in MOF-5. At higher metal doping concentrations the connector structure is reconstructed so that Zn ions are partially replaced by the doping metal ions, eventually ceasing the network porosity. Altering the aromatic linker to generate more favorable sites for

the doping metals has found no use. A similar scenario is predicted for remaining members of MOF family built with oxides of other transition metal ions.

8.2   Computational Methods

Optimization of the geometry and calculation of total energy and forces are performed with first principles calculations at the level of density functional theory (DFT), using the VASP code[19–21]. Generalized gradient approximation (GGA) of DFT in the form of PW91 functional [22] is used for the exchange and correlation potentials. Projector augmented wave (PAW) formalism is adopted and the cutoff kinetic energy for the plane wave basis is set to 400 eV [23, 24]. The Brillouin zone (BZ) is sampled at the Γ-point only due to a large unit cell. Shape and volume of the cells are conserved while the atomic coordinates were subject to change without any symmetry constraints. Convergence criterions for calculation of self consistent total energy and the structural optimizations were 10^{-4} eV difference between two consecutive electronic steps and 0.02 eV/Å residual force on each atom, respectively.

8.3   Results

We first determine the strength of interaction between a single metal atom and the MOF-5 structure ($\sim$1 at % dopant). The lowest energy structures with AMs are the ones where the dopants are positioned at connector sites, between oxygen atoms of neighboring BDC^{2-} (=1,4-benzenedicarboxylate) linkers. These geometries are lower in energy than the metals occupying the center of linker carbon rings by $0.31, 0.31$ and 0.19 eV/cell for Li, Na, and K dopants, respectively. In the case of AEM doping, we find that both Be and Ca are located at the connector sites, whereas a single neutral Mg atom interacts very weakly with MOF-5 on both sites. The optimized geometries for Be and Ca, however, are different. Be atom, prefers a similar position to that of AM atoms. Ca, on the other hand, favors a geometry where it stays intact with seven oxygen atoms, six from three BDC^{2-} linkers and one from the tetrahedral $[Zn_4O]^{6+}$. The presence of a single Ca atom inside the MOF-5 unit cell has greater influence on the modification of the zinc oxide connector site than the rest of the doping materials considered here.

We further investigate the effects of AM(AEM) doping on the MOF-5 system by considering a situation with increased doping concentration. In principle, when both faces of the BDC^{2-} linkers are functionalized twelve metal ions would be accommodated within the unit cell ($\sim$10 at % dopant). Here, we compare the relative stability
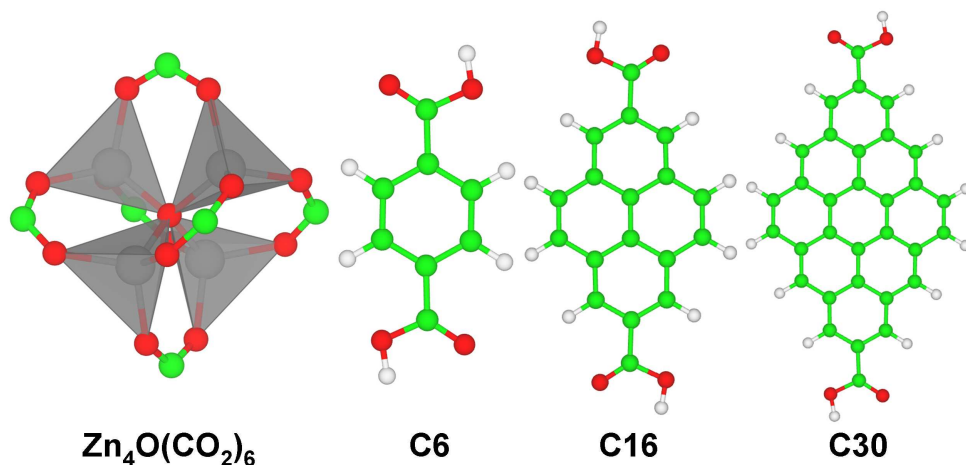
Figure 8.1: Connector geometry in MOF-5 (left figure), and linkers used in this study. Zinc, carbon, oxygen, and hydrogen atoms are shown as grey, green, red and white spheres, respectively.

of the two cases. In the first case, prior to relaxation all the twelve metal atoms are placed at a bonding distance above and below the hexagonal centers of six BDC^{2-} units. In the second case, all the metal atoms are placed around one of the two oxide connector sites inside the unit cell. Same initial geometries are used to simulate the effects of doping with AM(AEM) ions.

For each individual dopant, total energy differences between the optimized geometries of the first and the second cases are given in Table 8.1. It is clear that the entire set of lightweight AMs or AEMs thermodynamically favor the second case, in which they interact closely with the oxygen atoms of the MOF-5 system. This is in contrast to the earlier studies on the same system where only organic linker sites were considered for atomic Li adsorption [16–18]. Our results obtained from heavy doping are in connection with the single atom doped systems. Moreover, (except for Na and K) increasing doping concentration enlarges the total energy gap between the two cases, in favor of metal clustering around oxide connector sites. Particularly for Li doping, the energy difference is 7.66 eV/cell (or 0.64 eV/Li) (Table 8.1). The increment in total energy difference compared to the single atom doped system is due to a structural change around the connector site. In the relaxed structure, one of the Zn ions is found to be removed form the tetrahedral $[Zn_4O]^{6+}$ unit and moved to the cell cavity, consequently central oxygen is now bonded to a Li atom (Fig 2). The rest of the AM atoms also are stabilized in the vicinity of oxygen atoms. For

Table 8.1: Calculated binding energy values, Eb (eV/dopant), of metal dopants to the MOF-5 structure. Data corresponds to $\sim$1 at % and$\sim$10 at % dopant concentration.

Doping element	$\sim$1 at %		$\sim$10 at %	
	@linker	@connector	@linker	@connector
Li	-1.328	-1.640	-1.172	-1.811
Na	-0.699	-1.013	-0.636	-0.941
K	-1.096	-1.283	-0.931	-1.106
Be	-0.167	-1.107	-1.027	-3.366
Mg	-0.037	-0.051	-0.643	-1.356
Ca	-1.323	-1.520	-1.226	-2.891

Na(K), total energy differences between the relaxed structures of linker and connector sites is 3.66(2.09) eV/cell in favor of connector sites, but noticeably smaller than the Li doping scenario (Table 8.1). These values are in connection with the single atom doped system. Conservation of the $[Zn_4O]^{6+}$ geometry upon Na(K) doping together with the binding energy values implies that there is an energy barrier for structural modification. Earlier second group elements (Be, Mg, and Ca) also tend to cluster around the oxide connector positions. Interestingly, Zn ions are exchanged by all the AEMs, and accordingly, the cell geometry is modified. The results show that, increasing AEM doping concentrations, as in the case of Li doping, lead to a catastrophic restructuring of the geometry. It is therefore expected that the porosity of the 3-D system would be affected on the macro scale.

It is also important to know whether our conclusions on the MOF-5 will also hold for other MOF systems build with different organic linkers or metal oxide connectors. Isoreticular series of MOFs with $Zn_4O(CO_2)_6$ connectors are already been successfully synthesized [7, 25]. Here, as an example, we consider the interaction of a single neutral AM(AEM) atoms with three different molecules of various sizes, namely C6, C16 and C30 (Fig 1) (naming is according to the total number of ring carbons ,as in Ref.[16]). AMs are found to bind the C30 molecule the strongest, but with no remarkable improvement in binding energies compared to C6 molecule. For instance, in the case of Li, the calculated binding energy to the C30 molecule is $\sim$50 meV higher than to the C6 molecule. The binding energy value for the C6-Li system matches closely to that of one Li atom MOF-5 linker unit interaction. AEMs, on the other hand,
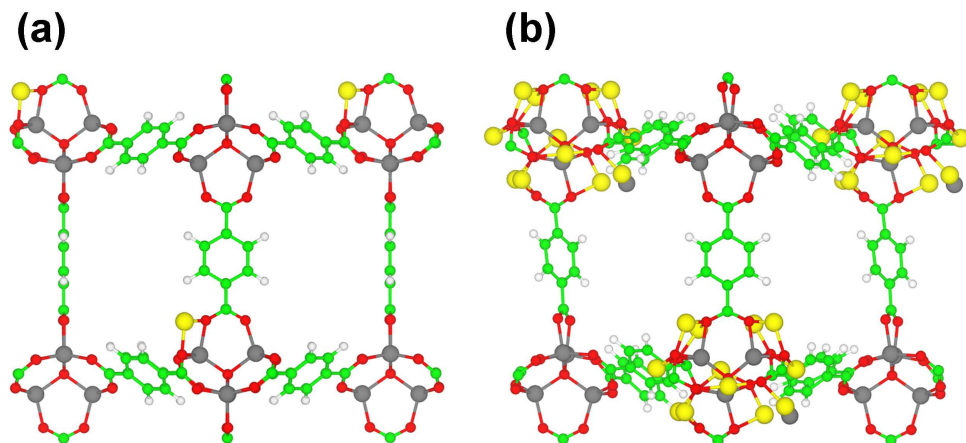
(a) **(b)**

Figure 8.2: Optimized geometries of MOF-5 system upon ∼1 at % (a), and ∼10 at % (b) Li (yellow spheres) doping at connector sites.

interact with the C6 molecule stronger than the other two molecules. Apart from weakly interacting Be and non-reacting Mg, Ca seems to be the ideal dopant within the AEM group. To sum up, we confirm that altering the linker does not provide a viable solution. For all of the doping metal atoms, none of the organic linkers studied here were able to successfully generate an energetically favorable site compared to the $Zn_4O(CO_2)_6$ connectors. Future synthesis of MOFs with high electron affinity linkers might open a new path for lightweight metal doping.

MOFs build with metal ions other than Zn have also drawn recent interest [7, 26–29]. Such systems are not necessarily isostructural with MOF-5. It is therefore not straightforward for us to study all of the available MOF structures in here. However, we can still generalize our conclusions on the prototype MOF-5 structure to the other MOF systems build with different transition metal oxide connectors. The key point whether a MOF system would resist structural alterations upon AM(AEM) doping lies on the relative stability of the metal oxide units. In the bulk phase, oxides of lightweight AM(AEM) atoms are mostly more stable than the oxides of transition metal ions [30–32]. Therefore, upon doing, most of the MOF systems with transition metal connector sites would be vulnerable to metal substitution reactions as observed in MOF-5.

Acknowledgments

Bibliography

[1] O. Yaghi *et al.*, Nature **423**, 705 (2003).

[2] N. L. Rosi *et al.*, Science **300**, 1127 (2003).

[3] X. Zhao *et al.*, Science **306**, 1012 (2004).

[4] J. Rowsell, J. Eckert, and O. Yaghi, J. Am. Chem. Soc. **127**, 14904 (2005).

[5] J. Rowsell, A. Millward, K. Park, and O. Yaghi, J. Am. Chem. Soc. **126**, 5666 (2004).

[6] J. Rowsell, E. Spencer, J. Eckert, J. Howard, and O. Yaghi, Science **309**, 1350 (2005).

[7] J. Rowsell and O. Yaghi, J. Am. Chem. Soc. **128**, 1304 (2006).

[8] J. Rowsell and O. Yaghi, Angew. Chem., Int. Ed. **44**, 4670 (2005).

[9] A. Wong-Foy, A. Matzger, and O. Yaghi, J. Am. Chem. Soc **128**, 3494 (2006).

[10] S. S. Kaye, A. Dailly, O. M. Yaghi, and J. R. Long, J. Am. Chem. Soc **129**, 14176 (2007).

[11] J. G. Vitillo *et al.*, J. Am. Chem. Soc. **130**, 8386 (2008).

[12] W. Zhou, H. Wu, and T. Yildirim, J. Am. Chem. Soc. **130**, 15268 (2008).

[13] M. Dinca and J. R. Long, Angew. Chem., Int. Ed. **47**, 6766 (2008).

[14] A. Dailly, J. Vajo, and C. Ahn, J. Phys. Chem. B **110**, 1099 (2006).

[15] J. Liu *et al.*, J. Phys. Chem. C **100**, 2911 (2008).

[16] S. Han and W. Goddard III, J. Am. Chem. Soc. **129**, 8422 (2007).

[17] A. Blomqvist, C. M. Araujo, P. Srepusharawoot, and R. Ahuja, Proc. Natl. Acad. Sci. U.S.A. **104**, 20173 (2007).

[18] A. Mavrandonakis, E. Tylianakis, A. K. Stubos, and G. E. Froudakis, J. Phys. Chem. C **112**, 7290 (2008).

[19] G. Kresse and J. Hafner, Phys. Rev. B **47**, 558 (1993).

[20] G. Kresse and J. Furthmüller, Phys. Rev. B **54**, 11169 (1996).

[21] G. Kresse and J. Furthmüller, Comput. Mater. Sci. **6**, 15 (1996).

[22] J. P. Perdew and Y. Wang, Phys. Rev. B **45**, 13244 (1992).

[23] P. E. Blöchl, Phys. Rev. B **50**, 17953 (1994).

[24] G. Kresse and D. Joubert, Phys. Rev. B **59**, 1758 (1999).

[25] M. Eddaoudi *et al.*, Science **295**, 469 (2002).

[26] N. Rosi *et al.*, J. Am. Chem. Soc. **127**, 1504 (2005).

[27] H. Furukawa, J. Kim, N. Ockwig, M. OKeeffe, and O. Yaghi, J. Am. Chem. Soc. **130**, 11650 (2008).

[28] P. Dietzel, Y. Morita, R. Blom, and H. Fjellvag, Angew. Chem., Int. Ed. **44**, 6354 (2005).

[29] P. Dietzel, B. Panella, M. Hirscher, R. Blom, and H. Fjellvåg, Chem. Commun. **2006**, 959 (2006).

[30] O. Kubaschewski, C. B. Alcock, and P. J. Spencer, *Mater Thermochemistry* (Oxford: Pergamon Press, 1993).

[31] M. W. Chase, *NIST-JANAF Thermochemical Tables* (New York: American Chemical Society, 1998).

[32] L. Wang, T. Maxisch, and G. Ceder, Phys. Rev. B **73**, 195107 (2006).

Chapter 9

Summary

At the present time, a sustainable provision of energy is one of the greatest challenges for mankind. It requires ground-breaking scientific ideas, bold monetary investments and innovative public actions to initiate technological, economical and social transitions. Energy generated from sustainable sources has to be transported and stored in an efficient and ecologically friendly way. At this point, hydrogen is a vital ingredient in the sustainable energy scenarios. It is crucial to find safe, compact and cost effective methods for storing hydrogen to enhance the future realization of the sustainable energy economy. Due to the complexity of developing hydrogen storage systems, scientific research at a fundamental level is required. The present thesis is devoted to the first-principles study of the hydrogen storage properties of a set of promising bulk, nano and molecular systems.

The thesis starts with a brief introduction (**Chapter 1**) of the background of hydrogen as a fuel. The introduction chapter lists several conventional and novel hydrogen storage methods. Viable hydrogen storage technologies should be able to encompass all the storage objectives. Besides being safe and economically affordable, the storage material needs to be compact and lightweight. Accordingly, a promising storage material has to achieve meaningful gravimetric and volumetric hydrogen densities. It is, therefore, a necessity that the storage system is built to a great extend from lightweight chemical elements. The operability of storage materials depends hugely on their thermal and kinetic properties. Accordingly, the materials should allow for an efficient thermal management and fast hydrogen (un)loading rates. Moreover, the storage systems need to be durable over many hydrogen (un)loading cycles.

Chapter 2 summarizes the computational methodology by discussing the theoretical and the practical background of the present study. Density functional theory

is described, which is the working horse of practical calculations. In an effort to simplify the solution of the complex physical problems a set of approximations are necessarily introduced. Pseudopotentials and plane-waves with a finite energy cutoff are the most notable of these approximations. The details of the calculations on the physical and the chemical properties of the materials are discussed at the end of the methodology chapter.

The computational results are presented in two parts. In **Part − A**, storage materials that are suited for storage of hydrogen in atomic form are considered. The main interest of Part A is devoted to the bulk systems of magnesium-dihydride (MgH_2) and its alloys with transition metals and aluminium or silicon. MgH_2 is an inexpensive, and compact material that offers storing of hydrogen in suitable gravimetric and volumetric densities. However, it suffers from slow (de)hydrogenation kinetics and a high thermodynamic stability. Alloying MgH_2 with lightweight transition metals (TMs) aims at enhancing the kinetic and the thermodynamic properties. As shown in **Chapter 3**, TM-alloying (∼20 at. %) initiates a phase transition from the original MgH_2 phase to a fluorite phase, resulting in significant improvements in the (de)hydrogenation kinetics. The thermodynamic properties of the new materials with high magnesium contents, however, are not improved sufficiently. In **Chapter 4**, possible disorders in the positions of metal atoms are modeled using special quasi-random structures (SQS) for a set of different compositions. SQSs of Mg-Ti-H, similar to the ordered structures, give evidence for a phase transition around 20 at. % Ti. In addition, in chapter 4 calculations regarding the optical response of ordered and disordered Mg-Ti-H structures are presented. The effects of adding Al or Si to Mg-Ti and their hydrides are examined in **Chapter 5**. The results show that the added elements greatly improve the thermodynamic properties of the Mg-Ti and their hydrides and make them more suitable for practical hydrogen storage applications.

In **Part − B**, several hydrogen storage materials are considered that are suited for storage of hydrogen in molecular form. A significant advantage of molecular hydrogen storage over chemical storage in atomic form, which requires dissociation of the hydrogen bond and the formation of a hydride, is the improved kinetics.

The first chapter of Part B, **Chapter 6**, focuses on polylithiated carbon and oxygen molecules as building blocks for hydrogen storage materials. In the gas phase polylithiated molecules favorably bind several hydrogen molecules, reaching extremely high gravimetric densities. Practical use of polylithiated molecules is made possible by condensing them on graphene sheets. In particular B or Be doped graphene strongly bind the molecules without seriously affecting the hydrogen bind-

ing energies.

In **Chapter 7**, boron planar sheets are considered as hydrogen storage templates. The computational results indicate that the alkali metal (AM) decorated boron sheets are a much better starting point for hydrogen storage than their carbon based counterparts. In particular, the boron-Li system is a promising candidate for hydrogen storage purposes.

Chapter 8 focuses on the potential applicability of metal organic frameworks (MOFs) as hydrogen storage materials. Stand-alone MOFs interact with hydrogen molecules via physisorption. Accordingly, massive operating pressures and cryogenic conditions are required to store reasonable amounts of hydrogen. Previous studies show that incorporating lightweight AMs or alkaline earth metals (AEMs) to the MOF structures enables a hydrogen storage under moderate thermodynamic conditions. The findings presented in this chapter, however, contradict the earlier studies on the interactions of AMs (AEMs) with the MOF systems. The results indicate that AMs (AEMs) bind very strongly to the oxide building blocks of MOF systems and have a detrimental effect on the structure of the entire system. As implied in chapter 8, lightweight AM or AEM doping of MOF structures is not an ideal strategy.

List of publications

[1] *Tunable hydrogen storage in magnesium-transition metal compounds: First-principles calculations*
Süleyman Er, Dhirendra Tiwari, Gilles A. de Wijs, and Geert Brocks
Phys. Rev. B **79**, 024105 (2009)

[2] *First-principles study of the optical properties of $Mg_x Ti_{(1-x)} H_2$*
Michiel J. van Setten, **Süleyman Er**, Geert Brocks, Robert A. de Groot, and Gilles A. de Wijs
Phys. Rev. B **79**, 125117 (2009)

[3] *First-principles modelling of magnesium titanium hydrides*
Süleyman Er, Michiel J van Setten, Gilles A. de Wijs, and Geert Brocks
J. Phys.: Condens. Matt.; Accepted (2009)

[4] *A computational study of hydrogen storage in Mg-Ti-X (X = Al, Si)*
Süleyman Er, Gilles A. de Wijs, and Geert Brocks
(in preparation)

[5] *Hydrogen storage by polylithiated molecules and nanostructures*
Süleyman Er, Gilles A. de Wijs, and Geert Brocks
J. Phys. Chem. C **113**, 8997 (2009)

[6] *DFT study of planar boron sheets: A new template for hydrogen storage*
Süleyman Er, Gilles A. de Wijs, and Geert Brocks
J. Phys. Chem. C; Accepted (2009)

[**7**] *Impacts of lightweight metal doping on metal-organic frameworks*
     Süleyman Er, Deniz Cakir, Gilles A. de Wijs, and Geert Brocks
     (in preparation)

[**8**] *Role of 3d transition metals in NaBH$_4$ thermodynamics: Ab initio study*
     Deniz Cakir, **Süleyman Er**, Gilles A. de Wijs, and Geert Brocks
     (in preparation)

[**9**] *Effects of Ca coating on boron fullerenes*
     Süleyman Er, Gilles A. de Wijs, and Geert Brocks
     (in preparation)

[**10**] *Hydrogen storage abilities of lightweight metal decorated boron doped hetero-
     fullerenes*
     Süleyman Er, Gilles A. de Wijs, and Geert Brocks
     (in preparation)

[**11**] *Ca deposited tetrazine based covalent-organic frameworks for hydrogen storage*
     Süleyman Er, Gilles A. de Wijs, and Geert Brocks
     (in preparation)

Short curriculum vitæ

Name: Süleyman Er
Date of birth: May 31st, 1980
Place of birth: Civril, Turkey

2009:   **Junior Researcher (Ph.D.)** in Physics.
           University of Twente, The Netherlands.
           Project: *Computational modeling of novel materials for hydrogen storage.*
           Supervisors: Dr. Geert Brocks and Prof. Dr. Paul J. Kelly.

2005:   **Bachelor of Science (B.Sc.)** in Chemistry.
           Bilkent University, Turkey.
           Project: *Computational study of single-site mutation and secondary
           structure stability: An isodesmic reaction approach.*
           Supervisor: Prof. Dr. Andrzej S. Cieplak.

2004:   **Visiting Research Scholar**.
           University of Illinois at Urbana-Champaign, USA.
           Project: *Atomic scale simulations for anti-cancer drug discovery.*
           Supervisor: Prof. Dr. Eric Oldfield.

2003:   **Trainee Research Scholar**.
           Max Planck Institute for Polymer Research, Mainz, Germany.
           European Snychrotron Radiation Facility, Grenoble, France.
           Project: *Controlled design of macro ion based nanostructured materials.*
           Supervisor: Dr. Franziska Gröhn.